Investigation of efficient electrochemical reduction of CO_2 to CO over Zn- and Cd-based catalysts

by

Jing Xiao

A thesis submitted in partial fulfillment of the requirements for the degree of

Doctor of Philosophy

in

Materials Engineering

Department of Chemical and Materials Engineering
University of Alberta

Abstract

Electrochemical CO_2 reduction reaction (CO_2RR), powered by renewable electricity sources, is an attractive approach to mitigating CO_2 emissions and to storing intermittent renewable energy in the form of high-value carbon-neutral fuels. Among the various CO_2RR products, CO, as an important feedstock for Fischer-Tropsch process, is the most kinetically accessible product. However, the sluggish kinetics for initial CO_2 activation and the inevitable competitive hydrogen evolution reaction (HER) in aqueous electrolytes lead to the insufficient selectivity and energy efficiency of CO production. Although noble metals, such as Au, Ag and Pt, have been recognized as the most efficient catalysts for CO production, their low abundances and the associated high costs hinder their large-scale applications. Therefore, it is highly imperative to develop inexpensive electrocatalysts capable of efficiently promoting CO_2RR to CO with high selectivity.

Among the possible candidate non-noble metals, Zn holds the promise as a potential alternative to noble metals due to its earth-abundance and intrinsic selectivity for CO production. Hence, hexagonal Zn nanoplates (H-Zn-NPs) enclosed by Zn(100) and Zn(002) facets were synthesized and studied for their feasibility to catalyze CO_2RR. Compared with the similarly sized Zn nanoparticles (S-Zn-NPs), the H-Zn-NPs exhibited remarkably enhanced current density, together with an improved CO Faradaic efficiency (FE) of over 85% in a wide potential window. Theoretical calculations revealed that the exposed Zn(100) facets and edge sites on H-Zn-NPs were energetically favorable for CO_2RR to CO, which directly results in the enhanced CO_2RR performance.

Recently, $CdCO_3$ was found to possess high CO selectivity because of the strong binding affinity with CO_2. However, the reported current density (< 1 mA cm^{-2}) is far from being satisfactory. Therefore, $CdCO_3$ nanoparticles decorated carbon nanofibers ($CdCO_3$-CNFs) were synthesized to boost CO_2RR by a strong catalyst-support interaction. As expected, the obtained $CdCO_3$-CNFs displayed a high FE of 93.4% and a good partial current density (~10 mA cm^{-2}) at a potential of –0.83 V. Moreover, the local pH effect on CO_2RR was investigated based on the in-situ synthesis of $CdCO_3$ from porous CdO nanosheets, which would release OH^- at the electrode/electrolyte interface. Compared with the pre-synthesized $CdCO_3$ having similar morphology, the in-situ grown $CdCO_3$ exhibited considerably increased FEs of CO in a wide potential range and achieved the maximum value of 99.2% at a potential of −0.86 V. The enhancement in CO selectivity was demonstrated to benefit from the higher local pH at the catalyst surface which significantly promoted CO_2RR while inhibiting HER. This work provides new insights into the design strategy for cost-effective and efficient electrocatalysts for CO_2RR to CO.

Preface

This thesis is an original work by Jing Xiao (J. Xiao) under the supervision of Dr. Jing-Li Luo (J.-L. Luo).

Chapter 1 is the introduction that contains the background knowledge and principles of electrochemical CO_2 reduction, as well as the literature survey of catalysts for electrochemical reduction of CO_2 to CO.

Chapter 2 presents the employed methodologies and characterizations.

Chapter 3 has been published as J. Xiao, M.-R. Gao, S. Liu, J.-L. Luo, Hexagonal Zn nanoplates enclosed by Zn (100) and Zn (002) facets for highly selective CO_2 electroreduction to CO, ACS Appl. Mater. Interfaces, 12 (2020) 31431-31438.

Chapter 4 has been published as J. Xiao, M.-R. Gao, J.-L. Luo, Rational design of $CdCO_3$ nanoparticles decorated carbon nanofibers for boosting electrochemical CO_2 reduction, J. Power Sources, 510 (2021) 230433.

Chapter 5 has been submitted to Chem. Eng. J. for publication as J. Xiao, S. Liu, P.-F. Sui, C. Xu, J.-L. Luo, In-situ generated hydroxides realize near-unity CO selectivity for electrochemical CO_2 reduction.

Chapter 6 includes the summary and future prospects.

I was responsible for designing and conducting all the experiments, data collection and analysis, as well as writing the manuscripts. For Chapter 3 and 4, M. -R. Gao worked on the DFT calculation part. For Chapter 3 and 5, Dr. S. Liu provided valuable suggestions in the modification of scientific figures for publication. For Chapter 5, P.-F. Sui and Dr. C. Xu assisted with part of the SEM characterizations. For all the work above, Dr. J.-L. Luo provided valuable comments and suggestions and made revisions for the manuscripts.

Acknowledgements

First and foremost, I would like to express my sincere gratitude to my supervisor, Dr. Jing-Li Luo, for all the academic and financial support during the past four years. She taught me how to think of and investigate the scientific questions in the right way, which must benefit the rest of my life. Without her patient instruction, insightful criticism and expert guidance, the completion of this thesis would not have been possible.

Secondly, my deep appreciation goes to my supervisor committing members, Dr. Anastasia Elias and Dr. Hongbo Zeng for their thoughtful suggestions and assistance during my research progress. I offer my sincere appreciation to Dr. Subiao Liu for his valuable suggestions in the experimental design of my first paper.

Thirdly, I would like to thank all my colleagues, Dr. Chong Sun, Dr. Nanqi Duan, Dr. Zhou Chen, Dr. Chenyu Xu, Miss. Yuanyuan Hong, Mr. Minrui Gao, Mr. Pengfei Sui, Mr. Shaoqing Liu, Miss. Mengnan Zhu, and Mr. Bowen Zhang, for their great help and collaboration during my research in the lab. Besides, I would like to thank Dr. Shihong Xu, Dr. Nancy Zhang and Dr. Peng Li in Nanofab, University of Alberta, for their assistance and suggestions in materials characterizations.

Fourthly, I would also like to acknowledge the funding agencies: Natural Science and Engineering Research Council of Canada (NSERC, GRPIN-2016-05494) and China Scholarship Council (CSC).

Last but not least, my special thanks are given to my family. Thanks for always being there for me, and for encouraging me in the academic path I chose.

Table of Contents

List of Tables

List of Figures

List of Symbols

E^0	Standard potential
F	Faraday's constant
I	Total current
j	Current density
j_{CO}	Partial current density of CO
η	Overpotential
E^{eq}	Equilibrium potential
C_{dl}	Double-layer capacitance
R_{s}	Ohmic resistance
R_{ct}	Charge-transfer resistance
ΔG	Gibbs free energy
E_{F}	Fermi energy
α	The ratio of diagonal length to thickness
R_f	Roughness factors
ΔE_{COOH}	Binding energy of *COOH
ΔE_{CO}	Binding energy of *CO
ΔE_{H}	Binding energy of *H

List of Abbreviations

CCS	Capture and storage of CO_2
CO_2RR	CO_2 reduction reaction
HER	Hydrogen evolution reaction
SHE	Standard hydrogen electrode
FE	Faradaic efficiency
NP	Nanoparticles
RHE	Reversible hydrogen electrode
DFT	Density functional theory
GB	Grain boundary
rGO	Reduced graphene oxide
CNT	Carbon nanotube
C_3N_4	Graphitic carbon nitride
EELS	Electron energy loss spectroscopy
IRAS	Infrared reflection absorption spectroscopy
EMIM-BF_4	1-ethyl-3-methylimidazolium tetrafluoroborate
H-Zn-NPs	Hexagonal Zn nanoplates
S-Zn-NPs	Similarly sized Zn nanoparticles
SCE	Saturated calomel electrode
$CdCO_3$-CNFs	$CdCO_3$ NPs decorated carbon nanofibers
$CdCO_3$-CB	$CdCO_3$ NPs decorated carbon black
PNS	Porous nanosheet

i-$CdCO_3$	In-situ grown $CdCO_3$
s-$CdCO_3$	Similarly sized $CdCO_3$
p-$CdCO_3$	Pristine commercial $CdCO_3$
XRD	X-ray diffraction
SEM	Scanning electron microscopy
EDS	Energy-dispersive spectroscopy
TEM	Transmission electron microscopy
XPS	X-ray photoelectron spectroscopy
UPS	Ultraviolet photoelectron spectroscopy
TGA	Thermalgravimetric analysis
LSV	Linear sweep voltammetry
CV	Cyclic voltammetry
GC	Gas chromatography
IC	Ion chromatography
ECSA	Electrochemically active surface area
EE	Energy efficiency
EIS	Electrochemical impedance spectroscopy
PDOS	Partial densities of states
CHE	Computational hydrogen electrode
SAED	Selected-area electron-diffraction
PR	Production rate
CPE	Constant phase element

Chapter 1. Introduction

1.1 CO_2 utilization

The extensive consumption of fossil fuels has caused an increasing accumulation of atmospheric carbon dioxide (CO_2), which in turn results in serious problems associated with resources, environment, and climate, known as the "global warming effect" [1-3]. To date, anthropogenic activities have caused about 1.0 °C of global warming above the pre-industrial level, and this is likely to reach 1.5 °C between 2030 and 2052 if the current emission rates persist [2]. In order to mitigate the global warming trend, the capture and storage of CO_2 (CCS) and the conversion and utilization of CO_2 have gained widespread attentions [4, 5]. However, CCS is limited by its high operating costs and high safety risks [6]. The conversion of CO_2 into value-added carbon-neutral fuels is a promising strategy for human society, to close the anthropogenic carbon cycle.

Typical approaches for CO_2 utilization include (bio)chemical, thermochemical, photochemical and electrochemical catalysis [5-7]. Among them, electrochemical CO_2 reduction reaction (CO_2RR) is considered as an appealing technology since it can be conducted under mild conditions (near room temperature and ambient pressure) in aqueous solutions, in which water instead of molecular hydrogen (H_2) gas is employed as a hydrogen source [6]. Moreover, when coupled with renewable electricity sources (e.g., hydroelectric, wind and solar energies), electrochemical CO_2RR makes it possible to achieve a net zero carbon emissions footprint, as illustrated in Figure 1.1 [3, 8]. These features imply that electrochemical CO_2RR possesses a great potential for simultaneously achieving carbon recycle utilization and renewable electricity storage.

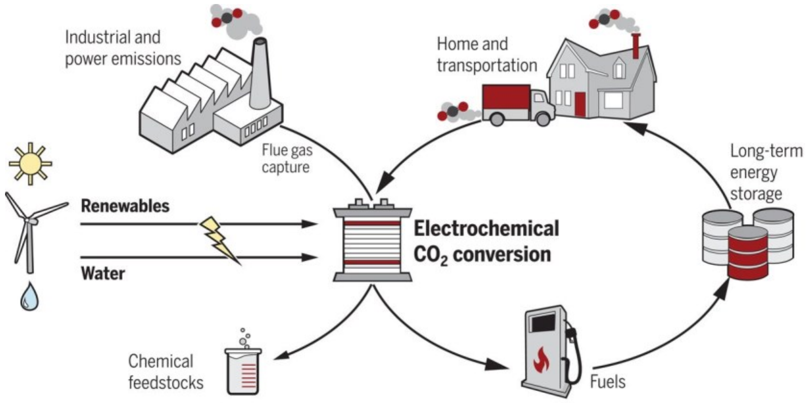

Figure 1.1 Illustration of a net carbon-neutral cycle through the pathway of electrochemical CO_2 conversion powered by renewable electricity sources. Reprinted with permission from Reference [3]. Copyright (2019) American Association for the Advancement of Science.

1.2 Fundamentals of electrochemical CO_2 reduction reaction (CO_2RR)

1.2.1 Thermodynamics of electrochemical CO_2RR

CO_2RR is cathodic by nature with a general form below [9]:

$$x\mathrm{CO_2} + n\mathrm{H}^+ + n\mathrm{e}^- \rightarrow \text{product} + y\mathrm{H_2O} \tag{1.1}$$

This reaction is usually complemented by oxygen evolution reaction (OER) in the anode [10]:

$$2\mathrm{H_2O} \rightarrow \mathrm{O_2} + 4\mathrm{H}^+ + 4\mathrm{e}^- \quad E^0 = 1.23\ \text{V vs. standard hydrogen electrode (SHE)} \tag{1.2}$$

Utilizing appropriate catalysts permits the formation of various products from the electrochemical CO_2RR, such as carbon monoxide (CO) [11, 12], formic acid (HCOOH) [13, 14], formaldehyde (CH_2O) [15], methanol (CH_3OH) [8, 16], methane (CH_4) [17], ethylene (C_2H_4) [18, 19] and ethanol [20]. Table 1.1 lists the standard potentials for CO_2RR to these commonly reported products [21]. The close thermodynamic standard potentials of different CO_2RR pathways make it difficult to control the selectivity. Moreover, the concurrent hydrogen evolution reaction (HER, the last equation in Table 1.1) often competes with

CO_2RR in aqueous media, further leading to the insufficient selectivity of target products. Therefore, it remains challenging to selectively target one specific product at a high yield.

Table 1.1 Selected standard potentials (E^0 vs. SHE) of CO_2RR and HER at 1.0 atm and 25 °C in aqueous solutions [21]. Reprinted with permission from Royal Society of Chemistry.

Products	Cathodic half-reactions	E^0 vs. SHE (V)
$CO(g)$	$CO_2(g) + 2H^+ + 2e^- \rightarrow CO(g) + H_2O(l)$	−0.11
$HCOOH(l)$	$CO_2(g) + 2H^+ + 2e^- \rightarrow HCOOH(l)$	−0.25
$CH_2O(l)$	$CO_2(g) + 4H^+ + 4e^- \rightarrow CH_2O(l) + H_2O(l)$	−0.07
$CH_3OH(l)$	$CO_2(g) + 6H^+ + 6e^- \rightarrow CH_3OH(l) + H_2O(l)$	0.02
$CH_4(g)$	$CO_2(g) + 8H^+ + 8e^- \rightarrow CH_4(g) + 2H_2O(l)$	0.17
$C_2H_4(g)$	$2CO_2(g) + 12H^+ + 12e^- \rightarrow C_2H_4(g) + 4H_2O(l)$	0.06
$C_2H_5OH(l)$	$2CO_2(g) + 12H^+ + 12e^- \rightarrow C_2H_5OH(l) + 3H_2O(l)$	0.08
$H_2(g)$	$2H^+ + 2e^- \rightarrow H_2(g)$	0.00

Encouragingly, high yield and selectivity have been achieved for CO_2RR to CO and HCOOH, especially the high selectivity of gaseous CO can save the cost of separation from aqueous electrolytes during the production process. More importantly, CO has a wide range of application prospects, including chemical, metallurgical and pharmaceutical applications [22, 23]. Particularly, as a component of syngas, CO can be downstream processed through Fischer-Tropsch chemistry for the synthesis of a series of basic organic chemical products and intermediates [24]. Hence, CO has been regarded as the most promising product to realize profitable electrochemical CO_2RR.

1.2.2 Mechanism of electrochemical CO_2RR to CO

The reaction pathway of electrochemical CO_2RR to CO is generally recognized to involve three elementary steps in aqueous media [12, 25],

$$CO_2 + * + H^+ + e^- \rightarrow *COOH \qquad (1.3)$$

$$*COOH + H^+ + e^- \rightarrow *CO + H_2O \tag{1.4}$$

$$*CO \rightarrow CO + * \tag{1.5}$$

where * refers to an adsorption site on catalysts. Briefly, a CO_2 molecule is initially adsorbed onto the surface of catalysts and forms a *COOH intermediate through a proton-coupled electron transfer process (Equation 1.3). Subsequently, the adsorbed *COOH experiences another proton-coupled electron transfer to form a *CO intermediate and a H_2O molecule (Equation 1.4). Finally, the *CO intermediate desorbs from the catalysts to produce CO (Equation 1.5). Such a reaction pathway has been widely applied to most theoretical calculations, which are based on a computational hydrogen electrode (CHE) model [26, 27]. However, in some experimental work, it is believed that one electron is firstly transferred to an adsorbed CO_2 to form a $*CO_2^-$ (sometimes denoted as $CO_2^{\bullet -}$) intermediate, and then a *COOH intermediate is generated after receiving one proton [28-30] as follows,

$$CO_2 + * + e^- \rightarrow *CO_2^- \tag{1.3a}$$

$$*CO_2^- + H^+ \rightarrow *COOH \tag{1.3b}$$

The proton donors are HCO_3^- ions and/or H_2O (or H_3O^+) molecules, depending on the nature of catalysts and experimental conditions [26, 31, 32]. The scheme of the reaction pathway for CO_2RR to CO is displayed in Figure 1.2 [33].

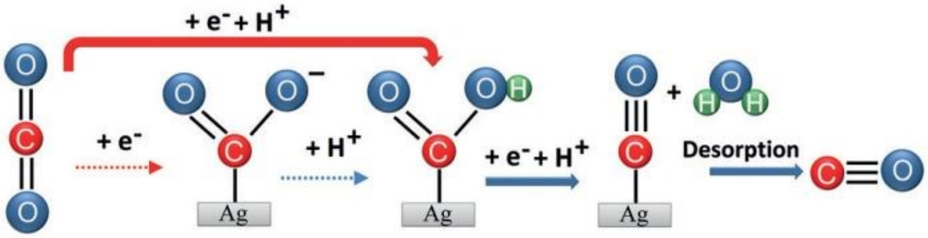

Figure 1.2 Schematic diagram of the reaction pathway for CO_2RR to CO. Reprinted with permission from Reference [33]. Copyright (2016) Wiley-VCH.

The formation of $*CO_2^-$ (Equation 1.3a) is the rate-determining step for the process of CO production over the majority of catalysts, since a very negative reduction potential (–1.9 V vs. SHE at pH = 7) is required to change the geometry of linear CO_2 molecules to the bent $*CO_2^-$ intermediates [34, 35]. The rate-determining step is switched to the subsequent proton-transfer step (Equation 1.3b) over some well-designed nanostructured catalysts, such as oxide-derived Au [29] and nanoporous Ag [36], which are able to effectively stabilize the $*CO_2^-$ intermediates. Tafel analysis is widely used to identify the rate-determining step for CO_2RR, and a Tafel slope of 118 mV dec^{-1} commonly corresponds to the initial electron-transfer step while 59 mV dec^{-1} corresponds to the first proton-transfer step [26].

The above results imply that the binding energies of the key intermediates, i.e., *COOH (or $*CO_2^-$) and *CO, are closely related to the CO selectivity on CO_2RR catalysts. A highly selective catalyst for CO production should possess catalytically active sites that can strongly bind *COOH to promote the second reduction step (Equation 1.4) but weakly adsorb the obtained *CO for product liberation (Equation 1.5). Meanwhile, the catalyst is also required to exhibit a low binding affinity for *H to inhibit the competitive HER. Therefore, tuning the binding energies of these intermediates is a crucial strategy for designing selective and efficient catalysts for CO_2RR to CO.

1.2.3 Merits for electrochemical CO_2RR to CO

A superior CO_2RR system should be highly active, selective, stable and cost-effective. Several parameters are normally used to characterize the performance of a CO_2RR system, including Faradaic efficiency, current density, overpotential, along with stability and cost.

1. *Faradaic efficiency*

Faradaic efficiency (FE) describes the ratio of the current density involving the electrochemical reaction for an aimed product to the applied current density [37]. It is popularly used to evaluate the selectivity of aimed products. The FE of CO can be determined by the following equation [37, 38]:

$$\mathrm{FE} = \frac{nm\mathrm{F}}{I} \times 100\% = \frac{nvpf_{\mathrm{v}}F}{RTI} \times 100\% \tag{1.6}$$

where n is the number of electrons participating the reaction for CO production; F is Faraday's constant (96485 C mol^{-1}); m (mol s^{-1}) is the number of moles of the harvested CO per second; I (C s^{-1}) is the total current; v (vol%) is the volume fraction of CO in the exhaust gases, which is equal to the mole fraction when the gases are considered to be ideal; f_{v} (m^3 s^{-1}) represents the volume flow rate of exhaust gases, which is measured by a flow meter at the exit of the cell at room temperature (T) and under ambient pressure (p).

2. *Current density*

Current density (j) is defined as the current flow per unit area of electrode surface, reflecting the reaction rate of CO_2RR. It is dependent on the utilization of catalysts, applied potential, and the diffusion rates of relevant species [10]. To directly evaluate the generation rate for CO, the partial current density of CO (j_{CO}) is introduced. It can be derived by multiplying j and the FE of CO. A high j_{CO} at specific applied potential is desirable for an efficient CO_2RR system.

3. *Overpotential*

Overpotential (η) is the potential difference between the potential where the reduction reaction occurs (E) and the thermodynamically determined equilibrium potential of CO_2RR (E^{eq}). Owing to the sluggish kinetics of CO_2RR and the insufficient activity of catalysts, it generally requires a high η to obtain a considerable j and an appreciable FE of CO, which is energetically wasteful [21]. For the high-efficiency CO_2 reduction, the high overpotential is the leading kinetic barrier.

4. Energy efficiency

Energy Efficiency (EE) describes the ratio of the energy stored in an aimed product to the applied electrical energy. The EE value of a product can be calculated via the equation below:

$$EE = \frac{E^{eq} \times FE}{E^{eq} + \eta} \times 100\% \tag{1.7}$$

where E^{eq} is the equilibrium cell potential for the product B and η is the overpotential. $E^{eq} + \eta$ is equal to the total cell voltage.

5. *Stability and cost*

Good long-term stability and low process costs are the two crucial requirements for technological commercialization. However, most of the reported stability tests for CO_2RR systems are not longer than 24 h. The process costs of CO_2RR mainly contain capital expenses and electricity costs. To reduce the process cost, it is desirable to develop a cost-effective catalyst with robust stability.

1.3 Literature review of catalysts for electrochemical CO_2RR to CO

As mentioned in Section 1.2.2, the catalysts for electrochemical CO_2RR to CO should process appropriate binding strength of the key intermediates, i.e., *COOH, *CO and *H, to effectively promote CO production while suppressing HER. However, the binding energies of these intermediates are typically proportionally correlated via the so-called linear scaling relationships [39, 40], making them hard to be controlled individually. To date, transition metals, along with their compounds, and some carbon-based materials have been demonstrated to exhibit proper binding affinities with the key intermediates for CO_2RR to CO. In addition, nanostructured noble metals, including Au [12, 41, 42], Ag [30, 36, 43] and Pd [44, 45], are among the most selective and efficient catalysts for CO production. However, their scarcity and the associated high costs inevitably hinder their large-scale applications. In recent years, tremendous efforts have been devoted to seeking earth-abundant alternatives, especially non-noble metal-based materials, with the catalytic activity and CO selectivity comparable to the noble metals. This chapter systematically summarizes the CO_2RR catalysts by categorizing them into three types: noble metal-based catalysts, non-noble metal-based catalysts and carbon-based catalysts.

1.3.1 Noble metal-based catalysts

Many fundamental studies have been done on noble metals because of their high intrinsic activity for CO production as well as the stable chemical and electrochemical properties. Several structural features, including particle size, exposed crystal facets, grain boundaries and metal-support interface, have been experimentally and computationally demonstrated to significantly influence the performance of CO_2RR to CO over noble metal-based catalysts.

Generally, the particle size of catalysts directly affects the proportion of the atoms at corner, edge, and surface sites, which possess different coordination numbers, surface energies and thus, the adsorption energies with key intermediates. The size-dependent CO_2RR performance was first studied by Zhu et al., who synthesized monodisperse Au nanoparticles (NPs) with a size range of 4−10 nm [12]. Experimentally, 8 nm Au NPs with a crystallite diameter of 4 nm exhibit the highest CO selectivity (FE of 90% at a potential of −0.67 V vs. reversible hydrogen electrode, RHE). Computationally, density functional theory (DFT) study suggests that edge sites facilitate CO_2RR while corner sites favor HER. As shown in

Figures 1.3a and b, on Au(211) facet (edge sites), the required free energy to form *COOH is rather low while the energy barrier of *H formation is sufficiently high. On the contrary, *H formation is quite facile on a 13-atom Au cluster (consisting of corner atoms). Moreover, the computational results suggest that the optimum size of Au NPs is around 1.5 nm, corresponding to the highest density of edge sites (Figure 1.3c). The size dependence of CO_2RR was also observed on Ag [46] and Pd NPs [44], further confirming that a decrease in particle size leads to an increasing population of edge sites, thereby significantly enhancing the selectivity and catalytic activity of CO production.

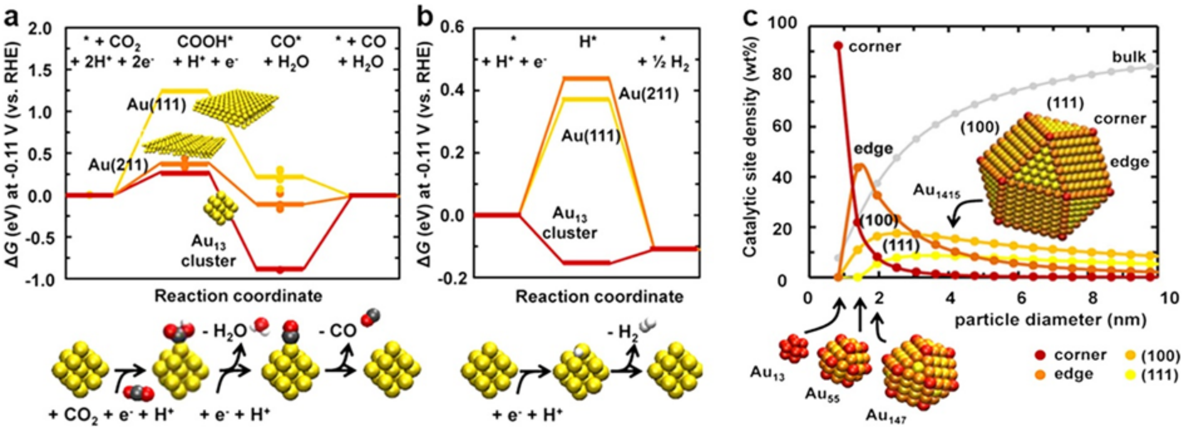

Figure 1.3 Free energy diagrams for (a) CO_2RR to CO and (b) HER on Au(111), Au(211) and a 13-atom Au cluster at -0.11 V vs. RHE. (c) Density of adsorption sites on closed-shell cuboctahedral Au clusters versus the cluster diameter. Reprinted with permission from Reference [12]. Copyright (2013) American Chemical Society.

Besides tuning particle size, the control of exposed crystal facets represents an alternative strategy for adjusting the binding energies of the key intermediates, so as to enhance the performance of CO_2RR to CO over noble metal-based catalysts. Hori is the pioneer in investigating the influence of different crystal facets on the catalytic activity of single-crystalline Ag [47]. He found that the j_{CO} of the prepared Ag catalysts decreased gradually with the sequence of Ag(110) > Ag(111) > Ag(100). This experimental evidence is in good agreement with the results of a recently reported computational study which suggests that the free energy barriers for the formation of *COOH on Ag(221) and Ag(110) facets are lower than the values on Ag(100) and Ag(111) facets [26]. Similarly, the CO_2RR catalytic activity on Pd metals is in the sequence of Pd(110) > Pd(111) > Pd(100) [48, 49]. In addition to Ag and Pd, Au-based catalysts also exhibit the facet-dependent performance for CO production. For instance, concave rhombic dodecahedron Au NPs exhibit superior CO selectivity as compared to low-index NPs, due to the presence of multiple high-index facets [50]. The high-index facets are open surface structures with high densities of coordinatively unsaturated atoms at the surface steps, which are active sites for various reactions [51, 52]. Tuning the shape of catalysts has been demonstrated to be an effective method to maximize the percentage of energetically favorable facets and hence, a high catalytic activity of CO production can be achieved on well-designed nanostructured architectures, such as ultrathin Au nanowires [41] and triangular Ag nanoplates [38].

Grain boundaries (GBs), one of the bulk defects with a strong strain effect, have proven to play a significant role in stabilizing the *COOH intermediate for CO_2RR. Kanan's group took an important step to reveal a quantitative linear correlation between the density of GBs and the CO_2RR catalytic activity based on Au metals. They initially observed an ultrahigh FE (> 96%) at a low overpotential of 0.24 V on oxide-derived Au metals and proposed that GBs may contribute to the enhanced CO_2RR performance since the oxide-derived Au metals contained a large density of GBs [29]. To verify this conjecture, this group further prepared polycrystalline Au with large grain sizes and designed a sophisticated protocol to directly measure the local catalytic activity across GBs while characterizing the density of GBs at the same time [53]. The results explicitly relate the enhanced CO_2RR catalytic activity with the increased coverage of GB surface terminations. Kim's group proposed a mechanism for the GB-dependent CO_2RR activity through DFT calculations [54]. Briefly, the broken local spatial symmetry near a grain boundary tunes the binding energy of Au metal, thereby stabilizing the *COOH intermediate for CO_2RR and boosting the CO formation.

The regulation of metal-support interactions is another effective strategy for catalyst design. Common support/substrate materials for catalytic metals include carbon black (CB), reduced graphene oxide (rGO), carbon nanotubes (CNTs), graphitic carbon nitride (C_3N_4) and inorganic metal oxides at the nanometer scale [55, 56]. A charge transfer between the catalytic metal and the support can occur due to their electronic difference [57]. The interaction between the catalyst and the support has been demonstrated to significantly affect the electronic properties on the surface of the catalytic metal, which is closely related to the stabilization of intermediates and consequentially the CO selectivity [58, 59]. For instance, C_3N_4 supported Au NPs (Au/C_3N_4) exhibit an improved CO_2RR performance than CB supported Au NPs (Au/C) [56]. The structural analysis indicates that the Au surface in Au/C_3N_4 processes abundant electrons donated from N atoms of the C_3N_4 support, and this leads to a negatively charged Au surface. DFT calculations demonstrate that the negatively charged Au surface is favorable for the stabilization of the *COOH intermediate. Particularly, the metal-oxide interface has been proven to be the active site for CO_2 activation and the reduction to CO. As shown in Figure 1.4, Au-CeO_x exhibits remarkably higher CO FE and j_{CO} than Au or CeO_x alone [60]. In situ scanning tunneling microscopy and synchrotron-radiation photoemission spectroscopy reveal that the Au-CeO_x interface is dominant in enhancing CO_2 adsorption and activation. Likewise, a series of MO_x/Ag (M = Cu, Cr, Sn, Bi, Pb and Mn) composites with the metal-oxide interfaces display both superior CO activity and selectivity than the pure Ag NPs at a relatively positive potential range [61].

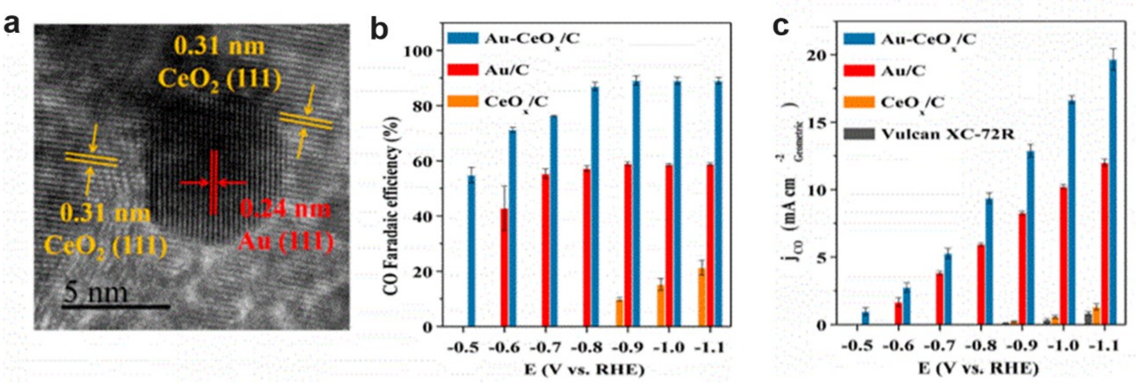

Figure 1.4 Structure and performance of Au-CeO_x catalyst. (a) High-resolution TEM image of Au-CeO_x catalyst. (b) CO FE and (c) geometric j_{CO} over Au, CeO_x and Au-CeO_x catalysts in CO_2-saturated 0.1 M $KHCO_3$ solution. Reprinted with permission from Reference [60]. Copyright (2017) American Chemical Society.

1.3.2 Non-noble metal-based catalysts

Efficient non-noble metal-based catalysts are highly desirable for the large-scale applications of electrochemical CO_2RR due to their low costs. In recent years, several earth-abundant transition metals, metal oxides and chalcogenides have been developed for electrochemical CO_2RR to CO. Different from noble metals, it is challenging to control the morphologies of those non-noble metal-based catalysts. Moreover, the catalyst design principles for non-noble metal-based catalysts are normally material-dependent. Therefore, in this section, the catalysts are categorized according to the types of non-noble metals. For each type, the main factors governing the CO_2RR performance are discussed.

Cu is the only known metal capable of electrochemically converting CO_2 to various hydrocarbons and alcohols besides CO. This is ascribed to its strong binding strength with the *CO intermediate, which facilitates the further protonation or C−C coupling reaction [9, 62]. Alloying Cu with other metals has been recognized as the most effective approach to breaking the linear scaling relationships, thereby steering the CO_2RR to the only product CO. The bimetallic Cu catalysts can be classified into two groups according to the dominant CO_2RR selectivity of the guest metals. The first group is Cu-M bimetallic catalysts, where M represents the CO producing metals (i.e., Au, Ag and Pd) [63-67]. In this group, the atoms of the guest metal serve as the reactive centers with an enhanced *COOH adsorption ability and *CO desorption ability in the presence of Cu [63, 65]. Cu atoms contribute to the activity by altering the electronic structure of their neighboring M atoms and/or adjusting the atomic arrangement in the active sites. As a result, the CO selectivity of these Cu-M bimetallic catalysts rises with increasing content of the guest metal.

The second group is Cu-N bimetallic catalysts, where N denotes the HCOOH producing metals (i.e., In and Sn) [68-74]. In contrast to the first group, a tiny amount of the guest metal is typically incorporated into Cu in the second group to achieve the maximum FE of CO. Further increasing the content of the guest metal will lead to an improved selectivity of HCOOH. Taking Cu core SnO_2 shell NPs (Cu/SnO_2) as an example (Figure 1.5), the thinner SnO_2 shell (0.8 nm) results in a remarkably high FE of CO (> 90%), while the thicker (1.8 nm) shell is more favorable for HCOOH production instead (CO FE < 1%) [70]. The authors ascribed the enhanced selectivity of CO over HCOOH to the coexistence of the uniaxial compression of the SnO_2 shell and the self-doping of Cu atoms diffusing out from the core to the shell. However, a more acceptable mechanism is that the interfaces between In/Sn and

Cu are the key factors contributing to the high CO selectivity on these bimetallic catalysts [69, 73, 74]. These interfaces have been demonstrated to lower the barrier for *COOH formation while still granting the facile release of *CO, and weakly adsorb *H and *OCHO (the key intermediate for HCOOH production). Consequently, the regulation of these key intermediates leads to the improved CO production while suppressing HER and other reduced products.

Zn holds the promise as a potential alternative to noble metals due to its abundance and moderate intrinsic selectivity for CO production [75]. However, the catalytic activity of polycrystalline Zn is far from being satisfactory, and highly negative potentials are required to obtain desirable FEs of CO. Several strategies have been developed for Zn catalysts to overcome these limitations. Firstly, it has been recognized that a facet ratio of Zn(101) to Zn(002) is closely related to the CO selectivity on Zn catalysts [76-78]. A representative study on the sub-microscale hexagonal Zn suggests that the increase in the facet ratio of Zn(101) to Zn(002) contributes to a higher FE of CO (85.4% at −0.95 V vs. RHE) as compared to Zn foil (25.1% at −0.95 V vs. RHE) [76]. Secondly, introducing catalytically more active sites (e.g., edge sites) into the Zn catalysts can significantly improve their selectivity and catalytic activity towards CO production [79-81]. For instance, due to a high density of edge sites, multilayered Zn nanosheets exhibit an increased FE of CO (86%) and a 14-fold higher j_{CO} (5.2 mA cm^{-2}) than bulk Zn foil at −1.13 V vs. RHE [80]. Lastly, constructing porous structures has been demonstrated to remarkably boost the CO_2RR catalytic activity on Zn catalysts [31, 82]. A highly porous Zn catalyst prepared by an electrodeposition method reaches a considerably high j_{CO} of 27 mA cm^{-2} at −0.95 V vs. RHE.

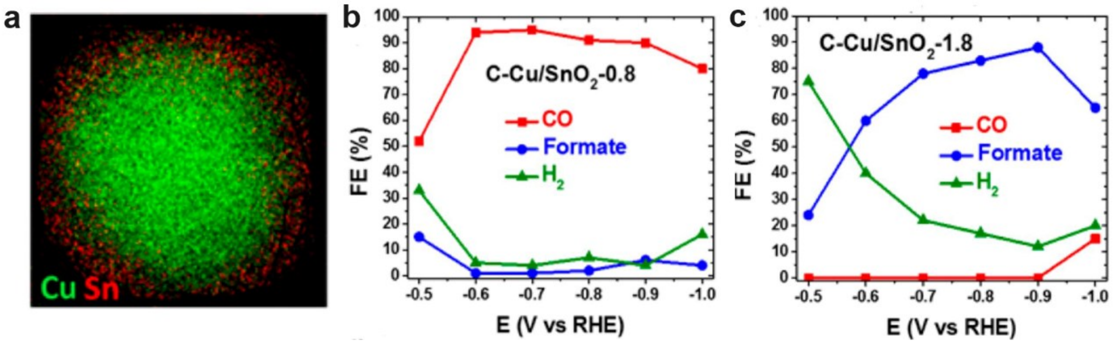

Figure 1.5 (a) Electron energy loss spectroscopy (EELS) elemental mapping of Cu and Sn of a 7/0.8 nm Cu/SnO$_2$ NP. Potential-dependent FEs of all reduction products on (b) Cu/SnO$_2$ NPs with 0.8 nm shell and (c) Cu/SnO$_2$ NPs with 1.8 nm shell in CO$_2$-saturated 0.5 M KHCO$_3$ solution. Reprinted with permission from Reference [70]. Copyright (2017) American Chemical Society.

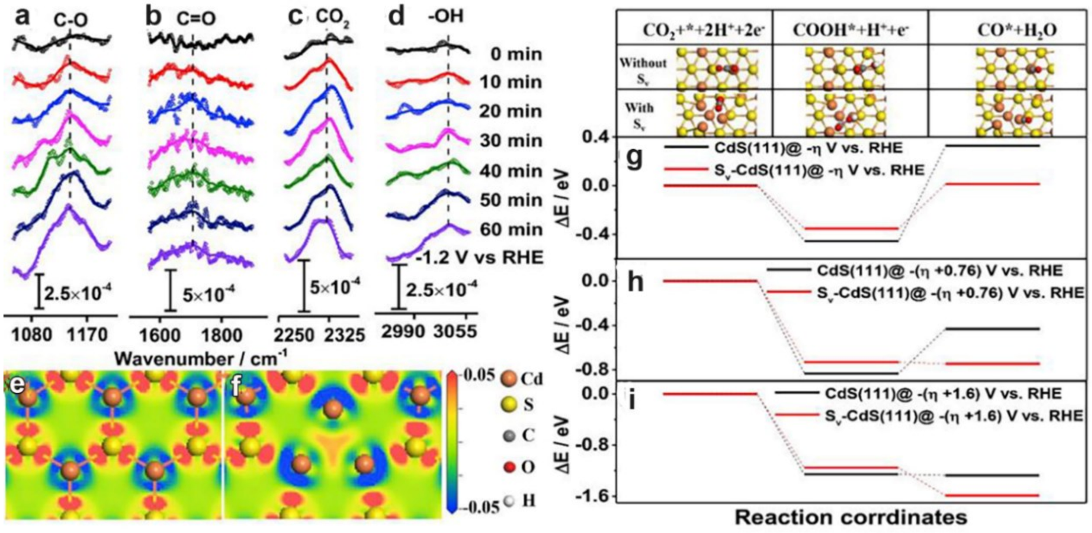

Figure 1.6 (a-d) In-situ ATR-IRAS (IRAS with attenuated total reflection mode) analyses of CdS-CNTs for CO$_2$RR. The distribution of electron deformation density for CdS(111) (e) without sulfur vacancy and (f) with sulfur vacancy. (g-i) DFT calculation results of relative energy for possible intermediates during CO$_2$RR on CdS(111) without sulfur vacancy and

CdS(111) with sulfur vacancy (S_v) at different potentials. Reprinted with permission from Reference [85]. Copyright (2019) Elsevier.

Recently, Cd-based catalysts have been explored as CO_2RR catalysts because of their low activity for HER [83]. Cadmium sulfoselenide (CdS_xSe_{1-x}) alloyed nanorods were first examined by Zeng and co-workers as a CO_2RR catalyst for syngas production [84]. The results indicate that among the various CdS_xSe_{1-x} nanorods, CdS nanorods exhibit the highest FE of 81% for CO production with a j_{CO} of 21.9 mA cm^{-2} achieved at −1.2 V vs. RHE. Hereafter, many experimental and computational studies have been conducted based on CdS to achieve selective CO production [85-89]. The high CO selectivity of CdS is associated with sulfur vacancies which are in-situ generated on the catalyst surface during the CO_2RR, as demonstrated by Qin et al. [85]. They performed in-situ infrared reflection absorption spectroscopy (IRAS) and DFT calculations on CdS NPs decorated CNTs (CdS-CNTs) (Figure 1.6) and concluded that the formation of sulfur vacancies modified the electron density of the catalyst surface and decreased the energy barrier for the conversion of *COOH to *CO. The beneficial effect of the sulfur vacancies is further confirmed by the studies of Li’s group [86, 87]. They proposed that the catalytic activity and CO selectivity on the CdS catalysts could be further improved by introducing an appropriate content of surface sulfur vacancies. More recently, $CdCO_3$ was reported to selectively convert CO_2 to CO at less negative potentials (–0.25 to –0.45 V) [90]. However, the current density is still unsatisfactory (< 1 mA cm^{-2}).

Besides the above catalysts, encouraging CO_2RR performance has been achieved in the catalyst systems that adopt ionic liquids, instead of aqueous solutions, as the electrolytes. 1-ethyl-3-methylimidazolium tetrafluoroborate (EMIM-BF_4) is the representative ionic liquid utilized for the electrochemical CO_2RR. It has been demonstrated that the $[EMIM]^+$ cations in CO_2-saturated media can form the $[EMIM\text{-}CO_2]^+$ complexes [91]. These $[EMIM\text{-}CO_2]^+$ complexes could physically adsorb on the negatively charged catalyst and subsequently increase the solubility of CO_2 [91-93]. Moreover, the $[EMIM\text{-}CO_2]^+$ complexes significantly lower the energy barrier of the initial electron-transfer process, which consequently lowers the overpotential required for the CO_2RR to CO [92, 94], as illustrated in Figure 1.7. As an outstanding cocatalyst, ionic liquid has been combined with several metals (e.g., Bi [95, 96], In [97] and Pb [98]) and metal chalcogenides (e.g., MoS_2 [91], WSe_2 [93] and MoSeS [99]) for highly efficient CO_2RR towards CO production. Unfortunately, the high price of ionic liquids impedes their commercial use in the CO_2RR.

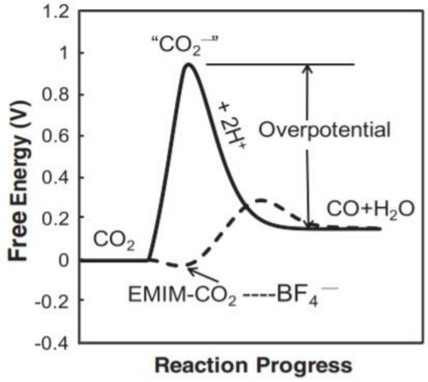

Figure 1.7 Schematic diagram of how the free energy of the system changes during the CO_2RR to CO in water (solid line) or EMIM-BF_4 (dashed line). Reprinted with permission from Reference [92]. Copyright (2011) American Association for the Advancement of Science.

1.3.3 Carbon-based catalysts

Although carbon materials themselves are electrochemically inert for CO_2RR, carbon-based materials doped with heteroatoms have recently been demonstrated as promising alternatives to metal-based catalysts owing to their natural abundance, good stability and relatively large surface area [100]. Moreover, heteroatoms are able to modulate the electronic properties (e.g., the charge and spin density) of adjacent carbon atoms and hence, they can be tuned to further enhance the CO_2RR activity of carbon-based catalysts [100, 101]. Nitrogen is the most commonly used atom for incorporation into a carbon network because of its similar size to the carbon atom and higher electronegativity. The higher electronegativity of N implies that the adjacent carbon atoms are more easily polarized and electrons are attracted toward the N-doped carbon, resulting in an increased electronic conductivity [102].

The CO_2RR performance over N-doped CNTs was initially evaluated by Ajayan's group in 0.1 M $KHCO_3$ solution (Figure 1.8).[103]. The N-doped CNTs exhibit remarkably higher FE (80%) for CO production as compared to pure CNTs (< 5%). To further pinpoint the active sites, this group conducted an extensive study on the effects of various nitrogen functionalities, i.e., graphitic, pyridinic and pyrrolic N defects, on the CO_2RR performance [104]. The experimental results indicate that the presence of graphitic and pyridinic N defects significantly decreases the overpotential and increases the CO selectivity of N-doped CNTs in comparison to pristine CNTs. On the contrary, pyrrolic N defects seem to have little impact on the CO_2RR activity. DFT calculation results suggest that pyridinic N defects retain a lone pair of electrons that are capable of binding CO_2, thereby promoting the CO_2RR. As for graphitic N defects, they can lower the energy barrier of *COOH formation in comparison to pristine CNTs. A subsequent study on N-doped three-dimensional (3D) graphene foam confirms that pyrrolic N is the most active site for the CO_2RR [105]. Inspired by these results, numerous N-doped carbon-based materials with a high content of pyrrolic N have been developed as the CO_2RR catalysts and have achieved high CO selectivity, such as quaternary

N-doped CNTs [106], N-doped graphene nanoribbon networks [107] and N, F-codoped holey carbon layers [108].

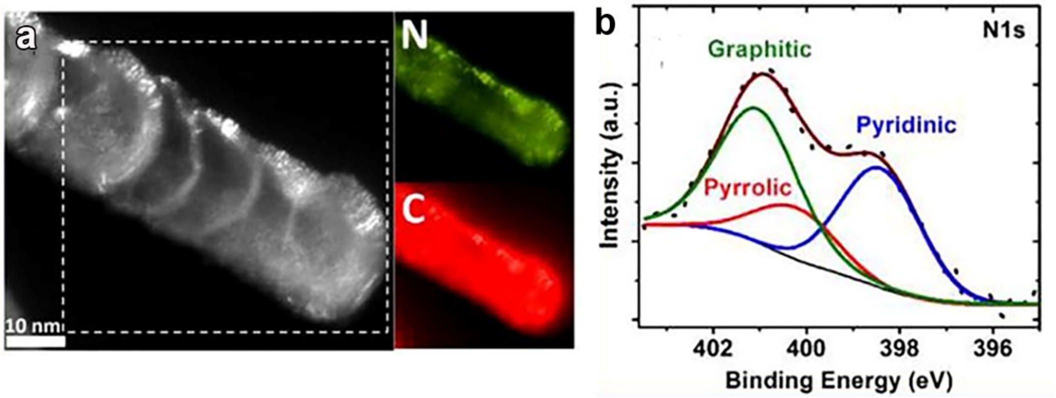

Figure 1.8 (a) EELS element mappings of N and C for N-doped CNTs. (b) Representative X-ray photoelectron spectroscopy (XPS) spectrum of N 1s for N-doped CNTs. The N 1s is deconvoluted into three peaks representing three different N functionalities. Reprinted with permission from Reference [73]. Copyright (2015) American Chemical Society.

1.4 Current status and remaining challenges

To date, nanostructured noble metals, including Au, Ag and Pd, are the most selective and efficient catalysts for the CO_2RR towards CO production. The noble metal-based catalysts are able to strongly bind the *COOH intermediate and thus lower the energy barrier for CO_2 activation, while weakly binding the *CO to facilitate the release of CO products. As a result, these catalysts deliver high FEs of CO (> 90%) at less negative potentials (> −1.0 V), together with good catalytic activities (j_{CO}) and stability. However, their scarcity and high costs inevitably limit their large-scale applications. Therefore, it is imperative to develop inexpensive catalysts with the CO_2RR performance comparable to the noble metal-based catalysts.

In response, various non-noble metal-based materials and carbon-based materials have been explored as the CO_2RR catalysts for selective CO production. In particular, Zn- and Cd-based catalysts exhibit good CO selectivity (FE > 80%) in aqueous solutions, endorsing them as promising alternatives to noble metals. However, some problems still remain and further research work needs to be conducted on the Zn- and Cd-based catalysts. For example, there is a controversy about whether the Zn(101) crystal facets govern the CO_2RR process on Zn catalysts, since the Zn(101) facets are not exposed and the role of the catalysts' shape has not been identified. The remaining issues regarding Zn- and Cd-based catalysts are summarized as follows:

(1) Highly negative potentials (< -1.0 V) are generally required for Zn- and Cd-based catalysts to obtain considerable CO selectivity, thus significantly decreasing the energy efficiency of CO_2RR;

(2) It remains as a challenge for Zn- and Cd-based catalysts to simultaneously achieve high j_{CO} and FE of CO;

(3) The roles of the structure and morphology as well as the local environment of catalysts on the CO_2RR performance over Zn- and Cd-based catalysts have not been fully understood.

Based on the above remaining challenges, the research objectives of this thesis are listed below:

(1) To rationally design Zn- and Cd-based architectures to simultaneously achieve high j_{CO} and FE of CO at less negative potentials;

(2) To investigate the effects of structure, morphology and local environment on the CO_2RR performance over Zn- and Cd-based catalysts.

1.5 References

[1] J. Rogelj, D. Huppmann, V. Krey, et al., A new scenario logic for the Paris Agreement long-term temperature goal, Nature 573 (2019) 357-363.

[2] S. Fawzy, A.I. Osman, J. Doran, et al., Strategies for mitigation of climate change: a review, Environ. Chem. Lett. 18 (2020) 2069-2094.

[3] P. De Luna, C. Hahn, D. Higgins, et al., What would it take for renewably powered electrosynthesis to displace petrochemical processes?, Science 364 (2019) 3506.

[4] E.S. Rubin, J.E. Davison, H.J. Herzog, The cost of CO_2 capture and storage, Int. J. Greenh. Gas Control 40 (2015) 378-400.

[5] A. Saravanan, D.-V.N. Vo, S. Jeevanantham, et al., A comprehensive review on different approaches for CO_2 utilization and conversion pathways, Chem. Eng. Sci. 236 (2021) 116515.

[6] R. Zhao, P. Ding, P. Wei, et al., Recent progress in electrocatalytic methanation of CO_2 at ambient conditions, Adv. Funct. Mater. 31 (2021) 2009449.

[7] Y. Zheng, W. Zhang, Y. Li, et al., Energy related CO_2 conversion and utilization: Advanced materials/nanomaterials, reaction mechanisms and technologies, Nano Energy 40 (2017) 512-539.

[8] K.P. Kuhl, T. Hatsukade, E.R. Cave, et al., Electrocatalytic conversion of carbon dioxide to methane and methanol on transition metal surfaces, J. Am. Chem. Soc. 136 (2014) 14107-14113.

[9] S. Nitopi, E. Bertheussen, S.B. Scott, et al., Progress and perspectives of electrochemical CO_2 reduction on copper in aqueous electrolyte, Chem. Rev. 119 (2019) 7610-7672.

[10] A.J. Martín, G.O. Larrazábal, J. Pérez-Ramírez, Towards sustainable fuels and chemicals through the electrochemical reduction of CO_2: lessons from water electrolysis, Green Chem. 17 (2015) 5114-5130.

[11] M. Valenti, N.P. Prasad, R. Kas, et al., Suppressing H_2 evolution and promoting selective CO_2 electroreduction to CO at low overpotentials by alloying Au with Pd, ACS Catal. 9 (2019) 3527-3536.

[12] W. Zhu, R. Michalsky, O. Metin, et al., Monodisperse Au nanoparticles for selective electrocatalytic reduction of CO_2 to CO, J. Am. Chem. Soc. 135 (2013) 16833-16836.

[13] R. Kortlever, I. Peters, S. Koper, et al., Electrochemical CO_2 reduction to formic acid at low overpotential and with high faradaic efficiency on carbon-supported bimetallic Pd–Pt nanoparticles, ACS Catal. 5 (2015) 3916-3923.

[14] P. Ding, H. Zhao, T. Li, et al., Metal-based electrocatalytic conversion of CO_2 to formic acid/formate, J. Mater. Chem. A 8 (2020) 21947-21960.

[15] K. Nakata, T. Ozaki, C. Terashima, et al., High‐yield electrochemical production of formaldehyde from CO_2 and seawater, Angew. Chem. Int. Ed. 53 (2014) 871-874.

[16] J.-M. Saveant, C. Tard, Attempts to catalyze the electrochemical CO_2-to-methanol conversion by biomimetic $2e^- + 2H^+$ transferring molecules, J. Am. Chem. Soc. 138 (2016) 1017-1021.

[17] W.-J. Ong, L.-L. Tan, S.-P. Chai, et al., Self-assembly of nitrogen-doped TiO_2 with exposed {001} facets on a graphene scaffold as photo-active hybrid nanostructures for reduction of carbon dioxide to methane, Nano Res. 7 (2014) 1528-1547.

[18] Y. Li, F. Cui, M.B. Ross, et al., Structure-Sensitive CO_2 electroreduction to hydrocarbons on ultrathin 5-fold twinned copper nanowires, Nano Lett. 17 (2017) 1312-1317.

[19] T.-C. Chou, C.-C. Chang, H.-L. Yu, et al., Controlling the oxidation state of the Cu electrode and reaction intermediates for electrochemical CO_2 reduction to ethylene, J. Am. Chem. Soc. 142 (2020) 2857-2867.

[20] S. Lee, G. Park, J. Lee, Importance of Ag–Cu biphasic boundaries for selective electrochemical reduction of CO_2 to ethanol, ACS Catal. 7 (2017) 8594-8604.

[21] J. Qiao, Y. Liu, F. Hong, et al., A review of catalysts for the electroreduction of carbon dioxide to produce low-carbon fuels, Chem. Soc. Rev. 43 (2014) 631-675.

[22] K.P. Kuhl, E.R. Cave, D.N. Abram, et al., New insights into the electrochemical reduction of carbon dioxide on metallic copper surfaces, Energy Environ. Sci. 5 (2012) 7050-7059.

[23] F.-Y. Gao, R.-C. Bao, M.-R. Gao, et al., Electrochemical CO_2-to-CO conversion: electrocatalysts, electrolytes, and electrolyzers, J. Mater. Chem. A 8 (2020) 15458-15478.

[24] A.Y. Khodakov, W. Chu, P. Fongarland, Advances in the development of novel cobalt Fischer− Tropsch catalysts for synthesis of long-chain hydrocarbons and clean fuels, Chem. Rev. 107 (2007) 1692-1744.

[25] R. Kortlever, J. Shen, K.J.P. Schouten, et al., Catalysts and reaction pathways for the electrochemical reduction of carbon dioxide, J. Phys. Chem. Lett. 6 (2015) 4073-4082.

[26] J. Rosen, G.S. Hutchings, Q. Lu, et al., Mechanistic insights into the electrochemical reduction of CO_2 to CO on nanostructured Ag surfaces, ACS Catal. 5 (2015) 4293-4299.

[27] S. Back, M.S. Yeom, Y. Jung, Active sites of Au and Ag nanoparticle catalysts for CO_2 electroreduction to CO, ACS Catal. 5 (2015) 5089-5096.

[28] Y. Hori, H. Wakebe, T. Tsukamoto, et al., Electrocatalytic process of CO selectivity in electrochemical reduction of CO_2 at metal electrodes in aqueous media, Electrochim. Acta 39 (1994) 1833-1839.

[29] Y. Chen, C.W. Li, M.W. Kanan, Aqueous CO_2 reduction at very low overpotential on oxide-derived Au nanoparticles, J. Am. Chem. Soc. 134 (2012) 19969-19972.

[30] C. Kim, H.S. Jeon, T. Eom, et al., Achieving selective and efficient electrocatalytic activity for CO_2 reduction using immobilized silver nanoparticles, J. Am. Chem. Soc. 137 (2015) 13844-13850.

[31] W. Luo, J. Zhang, M. Li, et al., Boosting CO production in electrocatalytic CO_2 reduction on highly porous Zn catalysts, ACS Catal. 9 (2019) 3783-3791.

[32] A. Wuttig, Y. Yoon, J. Ryu, et al., Bicarbonate is not a general acid in Au-catalyzed CO_2 electroreduction, J. Am. Chem. Soc. 139 (2017) 17109-17113.

[33] M. Ma, B.J. Trześniewski, J. Xie, et al., Selective and efficient reduction of carbon dioxide to carbon monoxide on oxide-derived nanostructured silver electrocatalysts, Angew. Chem. 128 (2016) 9900-9904.

[34] R. Chaplin, A. Wragg, Effects of process conditions and electrode material on reaction pathways for carbon dioxide electroreduction with particular reference to formate formation, J. Appl. Electrochem. 33 (2003) 1107-1123.

[35] J. Qiao, Y. Liu, J. Zhang, Electrochemical reduction of carbon dioxide: fundamentals and technologies, CRC Press, 2016.

[36] Q. Lu, J. Rosen, Y. Zhou, et al., A selective and efficient electrocatalyst for carbon dioxide reduction, Nat. Commun. 5 (2014) 3242.

[37] C. Delacourt, P.L. Ridgway, J.B. Kerr, et al., Design of an electrochemical cell making syngas (CO+ H_2) from CO_2 and H_2O reduction at room temperature, J. Electrochem. Soc. 155 (2008) B42-B49.

[38] S. Liu, H. Tao, L. Zeng, et al., Shape-dependent electrocatalytic reduction of CO_2 to CO on triangular silver nanoplates, J. Am. Chem. Soc. 139 (2017) 2160-2163.

[39] C. Shi, H.A. Hansen, A.C. Lausche, et al., Trends in electrochemical CO_2 reduction activity for open and close-packed metal surfaces, Phys. Chem. Chem. Phys. 16 (2014) 4720-4727.

[40] Y. Li, Q. Sun, Recent advances in breaking scaling relations for effective electrochemical conversion of CO_2, Adv. Energy Mater. 6 (2016) 1600463.

[41] W. Zhu, Y.-J. Zhang, H. Zhang, et al., Active and selective conversion of CO_2 to CO on ultrathin Au nanowires, J. Am. Chem. Soc. 136 (2014) 16132-16135.

[42] C. Chen, B. Zhang, J. Zhong, et al., Selective electrochemical CO_2 reduction over highly porous gold films, J. Mater. Chem. A 5 (2017) 21955-21964.

[43] S. Liu, X.-Z. Wang, H. Tao, et al., Ultrathin 5-fold twinned sub-25 nm silver nanowires enable highly selective electroreduction of CO_2 to CO, Nano Energy 45 (2018) 456-462.

[44] D. Gao, H. Zhou, J. Wang, et al., Size-dependent electrocatalytic reduction of CO_2 over Pd nanoparticles, J. Am. Chem. Soc. 137 (2015) 4288-4291.

[45] D. Gao, H. Zhou, F. Cai, et al., Pd-containing nanostructures for electrochemical CO_2 reduction reaction, ACS Catal. 8 (2018) 1510-1519.

[46] A. Salehi-Khojin, H.-R.M. Jhong, B.A. Rosen, et al., Nanoparticle silver catalysts that show enhanced activity for carbon dioxide electrolysis, J. Phys. Chem. C 117 (2013) 1627-1632.

[47] N. Hoshi, M. Kato, Y. Hori, Electrochemical reduction of CO_2 on single crystal electrodes of silver Ag (111), Ag (100) and Ag (110), J. Electroanal. Chem. 440 (1997) 283-286.

[48] A. Klinkova, P. De Luna, C.-T. Dinh, et al., Rational design of efficient palladium catalysts for electroreduction of carbon dioxide to formate, ACS Catal. 6 (2016) 8115-8120.

[49] N. Hoshi, M. Noma, T. Suzuki, et al., Structural effect on the rate of CO_2 reduction on single crystal electrodes of palladium, J. Electroanal. Chem. 421 (1997) 15-18.

[50] H.-E. Lee, K.D. Yang, S.M. Yoon, et al., Concave rhombic dodecahedral Au nanocatalyst with multiple high-index facets for CO_2 reduction, ACS Nano 9 (2015) 8384-8393.

[51] Q. Zhang, H. Wang, Facet-dependent catalytic activities of Au nanoparticles enclosed by high-index facets, ACS Catal. 4 (2014) 4027-4033.

[52] K.D. Yang, C.W. Lee, J.H. Jang, et al., Rise of nano effects in electrode during electrocatalytic CO_2 conversion, Nanotechnology 28 (2017) 352001.

[53] R.G. Mariano, K. McKelvey, H.S. White, et al., Selective increase in CO_2 electroreduction activity at grain-boundary surface terminations, Science 358 (2017) 1187-1192.

[54] K.-S. Kim, W.J. Kim, H.-K. Lim, et al., Tuned chemical bonding ability of Au at grain boundaries for enhanced electrochemical CO_2 reduction, ACS Catal. 6 (2016) 4443-4448.

[55] C. Rogers, W.S. Perkins, G. Veber, et al., Synergistic enhancement of electrocatalytic CO_2 reduction with gold nanoparticles embedded in functional graphene nanoribbon composite electrodes, J. Am. Chem. Soc. 139 (2017) 4052-4061.

[56] L. Zhang, F. Mao, L.R. Zheng, et al., Tuning metal catalyst with metal–C_3N_4 interaction for efficient CO_2 electroreduction, ACS Catal. 8 (2018) 11035-11041.

[57] V.R. Stamenkovic, B. Fowler, B.S. Mun, et al., Improved oxygen reduction activity on Pt_3Ni (111) via increased surface site availability, Science 315 (2007) 493-497.

[58] J.-H. Kim, H. Woo, J. Choi, et al., CO_2 electroreduction on Au/TiC: enhanced activity due to metal–support interaction, ACS Catal. 7 (2017) 2101-2106.

[59] J.-H. Kim, H. Woo, S.-W. Yun, et al., Highly active and selective Au thin layer on Cu polycrystalline surface prepared by galvanic displacement for the electrochemical reduction of CO_2 to CO, Appl. Catal. B 213 (2017) 211-215.

[60] D. Gao, Y. Zhang, Z. Zhou, et al., Enhancing CO_2 electroreduction with the metal-oxide interface, J. Am. Chem. Soc. 139 (2017) 5652-5655.

[61] X. Yuan, Y. Wu, B. Jiang, et al., Interface engineering of silver-based heterostructures for CO_2 reduction reaction, ACS Appl. Mater. Interfaces 12 (2020) 56642-56649.

[62] X. Feng, K. Jiang, S. Fan, et al., A direct grain-boundary-activity correlation for CO electroreduction on Cu nanoparticles, ACS Cent. Sci. 2 (2016) 169-174.

[63] M. Li, J. Wang, P. Li, et al., Mesoporous palladium–copper bimetallic electrodes for selective electrocatalytic reduction of aqueous CO_2 to CO, J. Mater. Chem. A 4 (2016) 4776-4782.

[64] Z. Yin, D. Gao, S. Yao, et al., Highly selective palladium-copper bimetallic electrocatalysts for the electrochemical reduction of CO_2 to CO, Nano Energy 27 (2016) 35-43.

[65] D. Kim, J. Resasco, Y. Yu, et al., Synergistic geometric and electronic effects for electrochemical reduction of carbon dioxide using gold–copper bimetallic nanoparticles, Nat. Commun. 5 (2014) 4948.

[66] J. Choi, M.J. Kim, S.H. Ahn, et al., Electrochemical CO_2 reduction to CO on dendritic Ag–Cu electrocatalysts prepared by electrodeposition, Chem. Eng. J. 299 (2016) 37-44.

[67] C. Roy, J. Galipaud, L. Fréchette-Viens, et al., CO_2 electroreduction at Au_xCu_{1-x} obtained by pulsed laser deposition in O_2 atmosphere, Electrochim. Acta 246 (2017) 115-122.

[68] S. Rasul, D.H. Anjum, A. Jedidi, et al., A highly selective copper–indium bimetallic electrocatalyst for the electrochemical reduction of aqueous CO_2 to CO, Angew. Chem. Int. Ed. 54 (2015) 2146-2150.

[69] S. Sarfraz, A.T. Garcia-Esparza, A. Jedidi, et al., Cu–Sn bimetallic catalyst for selective aqueous electroreduction of CO_2 to CO, ACS Catal. 6 (2016) 2842-2851.

[70] Q. Li, J. Fu, W. Zhu, et al., Tuning Sn-catalysis for electrochemical reduction of CO_2 to CO via the core/shell Cu/SnO_2 structure, J. Am. Chem. Soc. 139 (2017) 4290-4293.

[71] Y. Zhao, C. Wang, G.G. Wallace, Tin nanoparticles decorated copper oxide nanowires for selective electrochemical reduction of aqueous CO_2 to CO, J. Mater. Chem. A 4 (2016) 10710-10718.

[72] A. Jedidi, S. Rasul, D. Masih, et al., Generation of Cu–In alloy surfaces from $CuInO_2$ as selective catalytic sites for CO_2 electroreduction, J. Mater. Chem. A 3 (2015) 19085-19092.

[73] G.O. Larrazábal, T. Shinagawa, A.J. Martín, et al., Microfabricated electrodes unravel the role of interfaces in multicomponent copper-based CO_2 reduction catalysts, Nat. Commun. 9(1) (2018) 1477.

[74] W. Luo, W. Xie, R. Mutschler, et al., Selective and stable electroreduction of CO_2 to CO at the copper/indium interface, ACS Catal. 8 (2018) 6571-6581.

[75] Y. Hori, K. Kikuchi, S. Suzuki, Production of CO and CH_4 in electrochemical reduction of CO_2 at metal electrodes in aqueous hydrogencarbonate solution, Chem. Lett. 14 (1985) 1695-1698.

[76] W.D. Hye, S. Hyeyoung, K. Jaekang, et al., Highly efficient, selective, and stable CO_2 electroreduction on a hexagonal Zn catalyst, Angew. Chem. Int. Ed. 55 (2016) 9297-9300.

[77] B. Qin, Y. Li, H. Fu, et al., Electrochemical reduction of CO_2 into tunable syngas production by regulating the crystal facets of earth-abundant Zn catalyst, ACS Appl. Mater. Interfaces 10 (2018) 20530-20539.

[78] P. Moreno-García, N. Schlegel, A. Zanetti, et al., Selective electrochemical reduction of CO_2 to CO on Zn-based foams produced by Cu^{2+} and template-assisted electrodeposition, ACS Appl. Mater. Interfaces 10 (2018) 31355-31365.

[79] D.L.T. Nguyen, M.S. Jee, D.H. Won, et al., Selective CO_2 reduction on zinc electrocatalyst: the effect of zinc oxidation state induced by pretreatment environment, ACS Sustain. Chem. Eng. 5 (2017) 11377-11386.

[80] T. Zhang, X. Li, Y. Qiu, et al., Multilayered Zn nanosheets as an electrocatalyst for efficient electrochemical reduction of CO_2, J. Catal. 357 (2018) 154-162.

[81] M. Morimoto, Y. Takatsuji, K. Hirata, et al., Visualization of catalytic edge reactivity in electrochemical CO_2 reduction on porous Zn electrode, Electrochim. Acta 290 (2018) 255-261.

[82] K. Liu, J. Wang, M. Shi, et al., Simultaneous achieving of high Faradaic efficiency and CO partial current density for CO_2 reduction via robust, noble-metal-free Zn nanosheets with favorable adsorption energy, Adv. Energy Mater. 9 (2019) 1900276.

[83] J. Greeley, T.F. Jaramillo, J. Bonde, et al., Computational high-throughput screening of electrocatalytic materials for hydrogen evolution, Nat. Mater. 5 (2006) 909-913.

[84] R. He, A. Zhang, Y. Ding, et al., Achieving the widest range of syngas proportions at high current density over cadmium sulfoselenide nanorods in CO_2 electroreduction, Adv. Mater. 30 (2018) 1705872.

[85] B. Qin, Y. Li, H. Wang, et al., Efficient electrochemical reduction of CO_2 into CO promoted by sulfur vacancies, Nano Energy 60 (2019) 43-51.

[86] Y.H. Li, L. Cheng, P.F. Liu, et al., Simple cadmium sulfide compound with stable 95 % selectivity for carbon dioxide electroreduction in aqueous medium, ChemSusChem 11 (2018) 1421-1425.

[87] L. Cheng, Y. Li, A. Chen, et al., Impacts on carbon dioxide electroreduction of cadmium sulfides via continuous surface sulfur vacancy engineering, Chem. Commun. 56 (2020) 563-566.

[88] S.-H. Yu, F.-Y. Gao, S.-J. Hu, et al., High-curvature transition metal chalcogenide nanostructures with profound proximity effect enable fast and selective CO_2 electroreduction, Angew. Chem. 132 (2020) 8784-8790.

[89] N. Meng, C. Liu, Y. Liu, et al., Efficient electrosynthesis of syngas with tunable CO/H_2 ratios over $Zn_xCd_{1-x}S$-amine inorganic-organic hybrids, Angew. Chem. Int. Ed. 58 (2019) 18908-18912.

[90] X. Jiang, X. Wang, Q. Wang, et al., Efficient activation and electroreduction of carbon dioxide on an electrocatalyst cadmium carbonate, ACS Applied Energy Materials 4 (2021) 2073-2080.

[91] M. Asadi, B. Kumar, A. Behranginia, et al., Robust carbon dioxide reduction on molybdenum disulphide edges, Nat. Commun. 5 (2014) 4470.

[92] B.A. Rosen, A. Salehi-Khojin, M.R. Thorson, et al., Ionic liquid–mediated selective conversion of CO_2 to CO at low overpotentials, Science 334 (2011) 643-644.

[93] M. Asadi, K. Kim, C. Liu, et al., Nanostructured transition metal dichalcogenide electrocatalysts for CO_2 reduction in ionic liquid, Science 353 (2016) 467-470.

[94] B.A. Rosen, J.L. Haan, P. Mukherjee, et al., In situ spectroscopic examination of a low overpotential pathway for carbon dioxide conversion to carbon monoxide, J. Phys. Chem. C 116 (2012) 15307-15312.

[95] J.L. DiMeglio, J. Rosenthal, Selective conversion of CO_2 to CO with high efficiency using an inexpensive bismuth-based electrocatalyst, J. Am. Chem. Soc. 135 (2013) 8798-8801.

[96] Z. Zhang, M. Chi, G.M. Veith, et al., Rational design of Bi nanoparticles for efficient electrochemical CO_2 reduction: the elucidation of size and surface condition effects, ACS Catal. 6 (2016) 6255-6264.

[97] C. Ding, A. Li, S.-M. Lu, et al., In situ electrodeposited indium nanocrystals for efficient CO_2 reduction to CO with low overpotential, ACS Catal. 6 (2016) 6438-6443.

[98] L. Sun, G.K. Ramesha, P.V. Kamat, et al., Switching the reaction course of electrochemical CO_2 reduction with ionic liquids, Langmuir 30 (2014) 6302-6308.

[99] J. Xu, X. Li, W. Liu, et al., Carbon dioxide electroreduction into syngas boosted by a partially delocalized charge in molybdenum sulfide selenide alloy monolayers, Angew. Chem. Int. Ed. 56 (2017) 9121-9125.

[100] T. Liu, S. Ali, Z. Lian, et al., CO_2 electoreduction reaction on heteroatom-doped carbon cathode materials, J. Mater. Chem. A 5 (2017) 21596-21603.

[101] D. Voiry, H.S. Shin, K.P. Loh, et al., Low-dimensional catalysts for hydrogen evolution and CO_2 reduction, Nat. Rev. Chem. 2(1) (2018) 0105.

[102] T. Zheng, K. Jiang, H. Wang, Recent Advances in electrochemical CO_2-to-CO conversion on heterogeneous catalysts, Adv. Mater. 30 (2018) 1802066.

[103] J. Wu, R.M. Yadav, M. Liu, et al., Achieving highly efficient, selective, and stable CO_2 reduction on nitrogen-doped carbon nanotubes, ACS nano 9 (2015) 5364-5371.

[104] P.P. Sharma, J. Wu, R.M. Yadav, et al., Nitrogen-doped carbon nanotube arrays for high-efficiency electrochemical reduction of CO_2: on the understanding of defects, defect density, and selectivity, Angew. Chem. 127 (2015) 13905-13909.

[105] J. Wu, M. Liu, P.P. Sharma, et al., Incorporation of nitrogen defects for efficient reduction of CO_2 via two-electron pathway on three-dimensional graphene foam, Nano Lett. 16 (2016) 466-470.

[106] J. Xu, Y. Kan, R. Huang, et al., Revealing the origin of activity in nitrogen-doped nanocarbons towards electrocatalytic reduction of carbon dioxide, ChemSusChem 9 (2016) 1085-1089.

[107] S. Liu, H. Yang, X. Huang, et al., Identifying active sites of nitrogen-doped carbon materials for the CO_2 reduction reaction, Adv. Funct. Mater. 28 (2018) 1800499.

[108] F. Pan, B. Li, X. Xiang, et al., Efficient CO_2 electroreduction by highly dense and active pyridinic nitrogen on holey carbon layers with fluorine engineering, ACS Catal. 9 (2019) 2124-2133.

Chapter 2. Methodologies and Characterizations

2.1 The specifications of chemicals and gases

Zinc foil (0.25 mm of thickness, 99.95%), zinc chloride (anhydrous, 99.95%), cadmium acetate dihydrate (98%), cadmium carbonate (99+% powder), cadmium nitrate tetrahydrate (98.5%), sodium bicarbonate and sodium hydroxide (97%), polyvinylpyrrolidone (average Mw 58,000) and Nafion® N-117 membrane (0.18 mm of thickness) were all purchased from Alfa Aesar. Hydrogen peroxide solution (30 wt% in H_2O), zinc acetate dihydrate (⩾ 98%), carbon nanofibers (diameter of ~ 100 nm), potassium phosphate dibasic (⩾ 98%), potassium perchlorate (⩾ 99%), and Nafion perfluorinated ion-exchange resin solution (5 wt% in mixture of lower aliphatic alcohol and H_2O) were purchased from Sigma-Aldrich. Potassium bicarbonate (> 99.99%), isopropanol, and ethanol were purchased from Fisher Scientific Company. Carbon papers (Toray TGP-H-060) were purchased from Toray Industries Inc. Deionized water was taken from a Millipore Autopure system. All chemicals are of analytical grade and used without further purification. Hydrogen (99.995%), argon (99.998%), compressed air (extra dry) and carbon dioxide (99.99%) were purchased from Prexair.

2.2 Materials synthesis

2.2.1 Synthesis of hexagonal Zn nanoplates

To synthesize hexagonal Zn nanoplates (H-Zn-NPs), flower-like ZnO clusters were firstly prepared by a cathodic electrochemical deposition method in a three-electrode electrochemical cell. A Zn foil (1.0 × 1.5 cm^2), a saturated calomel electrode (SCE) and a Pt sheet were used as the working, reference and counter electrodes, respectively. The electrolyte was prepared by adding 80 μL of H_2O_2 solution (30 wt% in H_2O) to 150 mL of a 16 mM $ZnCl_2$ aqueous solution at 80 °C under stirring condition. Prior to the deposition, the Zn foil was mechanically polished and then ultrasonically cleaned in acetone and deionized water. A potential of –1.4 V vs. SCE was applied on the cleaned Zn substrate for 30 min while maintaining the bath temperature at 80 °C. After the deposition, the prepared black ZnO clusters were immediately rinsed with deionized water and dried in air. The prepared flower-like ZnO clusters were then electrochemically reduced at –0.96 V vs. RHE for 30 min in CO_2-bubbled 0.1 M $KHCO_3$ solution to obtain the H-Zn-NPs.

To clarify the shape effect on the catalytic activity of H-Zn-NPs for CO_2RR, similarly sized Zn nanoparticles (S-Zn-NPs) were also prepared by reducing spherical-like ZnO nanoparticles under identical conditions. The spherical-like ZnO nanoparticles were synthesized by annealing ground zinc acetate dihydrate in an alumina crucible at 600 °C for 3 h. Then, a homogeneous ink prepared by mixing the obtained white ZnO powder, ethanol and 5 wt% Nafion solution was subsequently loaded on a clean Zn foil and dried in air. To prevent oxidation, the obtained Zn samples were directly used for electrochemical measurements or immediately transferred and characterized.

2.2.2 Synthesis of $CdCO_3$ NPs decorated CNFs

$CdCO_3$ NPs decorated carbon nanofibers ($CdCO_3$-CNFs) were constructed to increase the catalytic activity through a strong catalyst-support interaction. 0.5 g of CNFs were heated at 70 °C for 4 h in the solution containing 12.5 mL of 70% nitric acid and 37.5 mL of 96% sulfuric acid. The products were repeatedly washed with deionized water by filtration until the washing water was neutral and then dried overnight in an oven at 60 °C. The acidic treatment creates oxygen functional groups on the surface of CNFs, which are necessary to better anchor the particles of catalysts [1]. 0.05 g of the pretreated CNFs were dispersed in 18 mL ethanol with ultrasonication for 20 min to obtain solution A, while 1.0 mmol cadmium acetate dihydrate was dissolved in 2 mL deionized water under stirring to get solution B. Then, solution A was added dropwise to solution B under vigorous stirring. After continually stirring for about 30 min, CO_2 was pumped into the mixture at a flow rate of 20 mL min^{-1} for 15 min. The products were collected through filtration and washed with deionized water and ethanol, and then dried at 60 °C. The sample is denoted as $CdCO_3$-CNFs.

To investigate the influence of the amount of Cd source on the CO_2RR performance, three additional samples were prepared by the same method except that 0.5, 1.5 and 2.0 mmol of cadmium acetate dihydrate were added. The sample prepared by the above method without adding CNFs is denoted as $CdCO_3$ NPs. To clarify the effect of the catalyst-support interaction on the CO_2RR performance, the sample synthesized by substituting CNFs with carbon black (CB, VXC-72R) is also prepared and denoted as $CdCO_3$-CB.

2.2.3 Synthesis of in-situ grown $CdCO_3$

Firstly, CdO porous nanosheets (PNSs) were prepared. 5 mL of NaOH (2 M) solution was added dropwise to 30 mL of 0.1 M $Cd(NO_3)_2$ solution under continuous stirring. After 30 min of stirring, the obtained mixture (pH = ~12) was transferred to a water bath and heated for 12 h at 60 °C. The white precipitate was collected through filtration, washed with deionized water and ethanol, and then dried at 60 °C. Finally, the sample was annealed at 400 °C in air for 2 h. The as-synthesized CdO PNSs were then loaded on carbon paper to fabricate the working electrode. Before electrochemical CO_2RR measurements, the fabricated electrode was pretreated to obtain in-situ grown $CdCO_3$ (i-$CdCO_3$) by applying a constant potential of −1.26 V vs. RHE for 90 min in CO_2-bubbled 0.1 M $KHCO_3$ electrolyte till the steady current was obtained.

For comparison, similarly sized $CdCO_3$ (s-$CdCO_3$) was prepared as follows. 0.154 g of $Cd(NO_3)_2 \cdot 4H_2O$ and 1 g of polyvinylpyrrolidone (average Mw ~58,000) were dissolved in 30 mL of deionized water to form a clear solution [2]. Then, 20 mL of 5 mM $NaHCO_3$ solution was added dropwise to the obtained mixture and stirred for 1 h at room temperature. The product was washed and collected by filtration and then dried at 60 °C overnight.

2.3 Materials characterizations

X-ray diffraction (XRD): The crystalline structures of catalysts were identified by XRD using a Rigaku Rotaflex Cu Kα radiation at 40 kV, 44 mA) and the diffraction patterns are analyzed using Jade 6.0 software.

Scanning electron microscopy (SEM): The microstructures and morphologies were observed using a high-resolution Zeiss Sigma field emission scanning electron microscopy (FE-SEM) equipped with an energy-dispersive spectroscopy (EDS) detector.

Transmission electron microscopy (TEM): The TEM characterization was performed using a JEOL JEM-ARM200CF electron microscopy equipped with an EDS detector. TEM with a cold field emission gun was operated at an accelerating voltage of 200 kV. Images were achieved using a Gatan digital imaging system through Digital Micrograph software.

X-ray photoelectron spectroscopy (XPS): XPS was employed to investigate the surface chemical states of catalysts using Kratos AXIS Ultra with monochromatic Al Kα source (hν

= 1486.6 eV). The binding energies of XPS spectra were calibrated by referencing to the adventitious C 1s peak at 284.8 eV.

Ultraviolet photoelectron spectroscopy (UPS): The work functions of catalysts were measured by UPS using the Kratos AXIS Ultra with He I source (hν =21.2 eV) at –10 V.

CO_2/N_2 adsorption/desorption: The CO_2 adsorption isotherms were measured using an Autosorb iQ apparatus. The pore size of CdO PNSs was measured by N_2 adsorption/desorption method using the same apparatus.

Thermalgravimetric analysis (TGA): The weight losses of $CdCO_3$ NPs and CdCO3-CNFs were determined by TGA on a TA SDT Q600 instrument at a heating rate of 5 °C min^{-1} from room temperature to 900 °C in air.

2.4 Electrochemical measurements and product analysis

Electrochemical measurements, including linear sweep voltammetry (LSV), potentiostaic tests and cyclic voltammetry (CV), were conducted in an H-cell separated by Nafion 117 membrane. A Solartron 1255 frequency response analyzer and a Solartron 1286 electrochemical interface instrument were used in the work about H-Zn-NPs, while an Autolab electrochemical workstation was employed in the studies on $CdCO_3$-CNFs and i-$CdCO_3$.

The schematic diagram of the H-cell is shown in Figure 2.1. A platinum plate and a SCE were used as the reference and the counter electrodes, respectively. The catalysts coated Zn foils were used as the working electrodes in the study on H-Zn-NPs. The typical preparation procedure of working electrodes in the study on $CdCO_3$-CNFs is described below. 5 mg of as-prepared catalysts were dispersed in 1 mL of a mixed solvent containing 700 μL isopropanol, 250 μL deionized water and 50 μL of 5 wt% Nafion solution, followed by ultrasonic treatment for 2 hours to form a homogeneous suspension. Next, 50 μL of the mixture was spread on a carbon paper (0.5×1 cm^2) and then dried at room temperature before testing. The working electrodes in the study on i-$CdCO_3$ were prepared by a similar procedure except that 1 mg of catalysts and 4 mg CB were dispersed in 1 mL of the mixed solvent, and 50 μL of the mixture was spread on a carbon paper (0.5×1 cm^2).

0.1 M $KHCO_3$ (pH = 6.8) was utilized as the electrolyte in the studies on H-Zn-NPs and i-$CdCO_3$, while 0.5 M $KHCO_3$ (pH = 7.2) was employed in the work on $CdCO_3$-CNFs. To remove the oxygen in the electrolyte, the bicarbonate solution was bubbled with CO_2 at a flow rate of 20 mL min^{-1} for 30 min until saturated before the tests. During the CO_2RR, CO_2 was continuously bubbled through the electrolyte to maintain the CO_2-saturated state. All the applied potentials are referred to the reversible hydrogen electrode (RHE) using the equation:

$$\text{Potential (vs. RHE)}=\text{Potential (vs. SCE)}+0.241\ \text{V}+0.0592\times\text{pH V} \qquad (2.1)$$

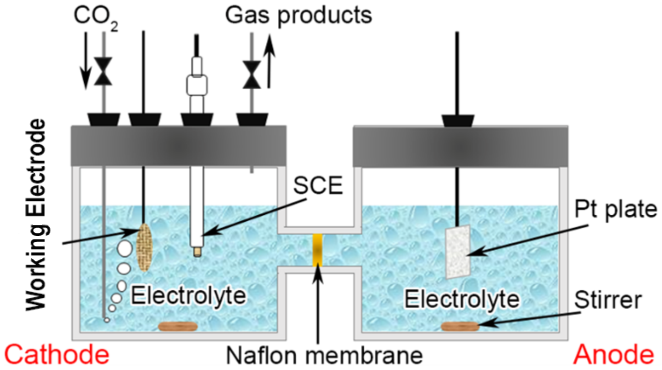

Figure 2.1 Schematic diagram of the H-cell.

The gaseous products from the cathode compartment were analyzed using a gas chromatography (GC, Agilent 6890N) connected directly to the electrochemical cell. The GC was equipped with a packed bed column (HaySep D) operated at 80 °C with Ar as carrier gas. The gaseous products, H_2, CH_4 and CO, were separated in a molecular sieve column (Alltech, part no. 57732) and detected by a thermal conductivity detector, while CO_2 and hydrocarbons flowed through a HaySep column (Alltech, part no. 14487) and detected by a flame ionization detector. The formic acid was analyzed using ion chromatography (IC, 850 Professional IC-AnCat-MCS) equipped with a Metrosep Organic Acids-250/7.8 column. The eluent was 0.5 mmol L^{-1} sulfuric acid mixed with 10% acetone with the standard flow rate of 0.5 mL min^{-1}.

2.5 Electrochemically active surface area measurement

The electrochemically active surface area (ECSA) of catalysts were calculated by the following equation:

$$\mathrm{ECSA} = R_f \times S \tag{2.2}$$

where S stands for the real surface area of the smooth metal electrode, which is generally equal to the geometric area of the substrate (Zn foil or carbon paper). The roughness factor R_f was estimated from the ratio of double-layer capacitance (C_{dl}) for the working electrode and the corresponding smooth catalyst. The C_{dl} was determined by measuring the capacitive current associated with double-layer charging from the scan-rate dependence of cyclic voltammetry (CV). In Chapter 3, CV was performed on the Zn catalysts at various scan rates of 20, 40, 60, 80, 100 and 120 mV s^{-1} in an Ar-bubbled 0.5 M Na_2SO_4 electrolyte. The CV potential range was selected from –1.13 to –1.23 V vs. SCE. In Chapter 4 and 5, CV was performed on the electrodes at various scan rates of 10, 20, 40, 60, 80, and 100 mV s^{-1} in a CO_2-bubbled $KHCO_3$ solution. The CV potential range was selected from –0.2 to –0.3 V vs. SCE. The C_{dl} was estimated by plotting the $\Delta j = (j_a - j_c)$ at –1.18 V (Chapter 3) or –0.25 V

(Chapter 4 and 5) vs. SCE (where j_a and j_c are the anodic and cathodic current densities, respectively) as a function of the scan rate. The linear slope is twice of the C_{dl}.

2.6 References

[1] M. Gangeri, S. Perathoner, S. Caudo, et al., Fe and Pt carbon nanotubes for the electrocatalytic conversion of carbon dioxide to oxygenates, Catal. Today 143 (2009) 57-63.

[2] X. Jiang, X. Wang, Q. Wang, et al., Efficient activation and electroreduction of carbon dioxide on an electrocatalyst cadmium carbonate, ACS Applied Energy Materials 4 (2021) 2073-2080.

Chapter 3. Hexagonal Zn Nanoplates Enclosed by Zn(100) and Zn(002) Facets for Highly Selective CO_2 Electroreduction to CO

Abstract: Electrochemical reduction of CO_2 (CO_2RR) to carbon-neutral fuels is a promising strategy for renewable energy conversion and storage. However, developing earth-abundant and cost-effective electrocatalysts with high catalytic activity and desirable selectivity for target fuel is still challenging and imperative. Herein, hexagonal Zn nanoplates (H-Zn-NPs) enclosed by Zn(100) and Zn(002) facets were successfully synthesized and studied for their feasibility toward CO_2RR. Compared with the similarly sized Zn nanoparticles (S-Zn-NPs), the H-Zn-NPs exhibit remarkably enhanced current density, together with an improved CO Faradaic efficiency (FE) of over 85% in a wide potential window, where a maximum FE of 94.2% is achieved. The enhancement in CO_2RR performance benefits from the substantial catalytically active sites introduced by the special architecture of H-Zn-NPs. Density functional theory calculations reveal that the exposed Zn(100) facets and edge sites on H-Zn-NPs are energetically favorable for CO_2RR to CO, which directly results in the enhanced CO_2RR performance. This study undoubtedly provides a straightforward approach to controlling the catalytic activity and selectivity of CO_2RR through tuning the shape of Zn-based catalysts, so as to maximize the percentage of exposed Zn(100) facets.

3.1 Introduction

The global warming and adverse climate changes caused by the greenhouse gas effect have triggered worldwide efforts to reduce atmospheric CO_2 concentration in a sustainable manner [1, 2]. Electrochemical CO_2 reduction reaction (CO_2RR) has been recognized as an attractive strategy to mitigate CO_2 emissions and enable the conversion of CO_2 to valuable fuels (e.g., CO, HCOOH, and CH_4), especially when integrated with the utilization of intermittent energy sources (e.g., solar, wind and tidal energy) [3, 4]. However, a high overpotential is generally required to initiate CO_2RR due to the thermodynamic stability of CO_2 molecules [5]. Concurrently, the kinetically preferable hydrogen evolution reaction (HER) invariably competes with CO_2RR in aqueous electrolytes, which further decreases the CO_2RR activity and the selectivity of target products [4]. Therefore, it is imperative to search for highly active and selective catalysts to enable the electrochemical CO_2RR with low overpotentials.

Nanostructured noble metals, such as Au [6-8], Ag [9-11] and Pd [12, 13], have been reported as the benchmarking electrocatalysts to selectively convert CO_2 to CO. However, the scarcity and the associated high cost of noble metals inevitably limit their large-scale applications. Among the possible candidate non-noble metals in replacement of the noble metals mentioned above, Zn holds the promise as a potential alternative to noble metals due to its earth-abundance and intrinsic selectivity for CO production [14]. Nevertheless, the CO_2RR performance over Zn catalysts is still unsatisfactory, especially in bicarbonate electrolytes [15-20]. Currently, the shape effects of various nanostructures (Au- [6, 7], Ag- [9] and Cu-based [21] catalysts), which can significantly influence the CO_2RR activity and selectivity, have been identified. However, the effect of shape on CO_2RR over Zn catalysts remains unclear. To this end, several Zn architectures (e.g., dendritic Zn [15], hexagonal Zn [16], and porous Zn [17] structures) have been investigated, and demonstrated to show enhanced catalytic activity and CO selectivity as compared to their bulk counterparts. Particularly, a representative study about sub-microscale hexagonal Zn claims that the increase in crystal facet ratio of Zn(101) to Zn(002) contributes to a higher CO Faradaic efficiency (FE) as compared to Zn foil [16]. However, the morphological evidence provided for this claim may not be sufficient, and meanwhile, the specific role of the hexagonal shape in the selectivity improvement still needs to be explored. Moreover, as of this writing, there are few reports about CO_2RR activity based on nanoscale Zn catalysts, and the structural and morphological features of Zn nanostructures that govern the CO_2RR process have not been fully understood. Therefore, experimental and computational work is still needed to clarify the effect of morphology on CO_2RR activity and selectivity over structurally well-defined Zn nanostructures, so as to provide a feasible strategy for designing highly active and selective non-noble metal-based catalysts for CO_2RR.

In this study, flower-like ZnO clusters were synthesized by an electrodeposition method and then electrochemically reduced to metallic hexagonal Zn nanoplates (H-Zn-NPs) for CO_2RR. The H-Zn-NPs are found to efficiently promote CO_2RR toward CO production with improved catalytic activity, good stability and remarkably high CO selectivity of over 85% in a broad potential range. DFT calculations reveal that the exclusive hexagonal Zn nanostructure offers an increased number of Zn(100) and edge atoms that are active for CO_2RR to CO.

3.2 Results and discussion

Figure 3.1a illustrates the schematic diagram of the evolution process of the H-Zn-NPs formation accompanied by the morphologies of ZnO clusters and H-Zn-NPs. Briefly, the flower-like ZnO clusters on a Zn foil with sharp petals were first achieved through electrodepositing a solution containing $ZnCl_2$ and H_2O_2, followed by the electrochemical reduction of ZnO clusters to the final H-Zn-NPs (Figures S3.1 and S3.2, see Section 3.5 for the supporting figures and tables). SEM, XRD and XPS were employed to demonstrate the morphology and structure evolution of ZnO clusters to H-Zn-NPs. Apparently, the final H-Zn-NPs are composed of randomly oriented nanoplates with an average diagonal length of about 155 nm (Figure S3.3). The H-Zn-NPs show a highly porous structure, which ensures a substantial number of active sites, while the XRD patterns (Figure S3.4) demonstrate the reduction of wurtzite ZnO (JCPDS 80-0074) to pure hexagonal close-packed Zn (JCPDS 87-0713). This is further validated by XPS results, since Zn 2p peaks shift towards lower binding energies after the reduction process (Figure S3.5).

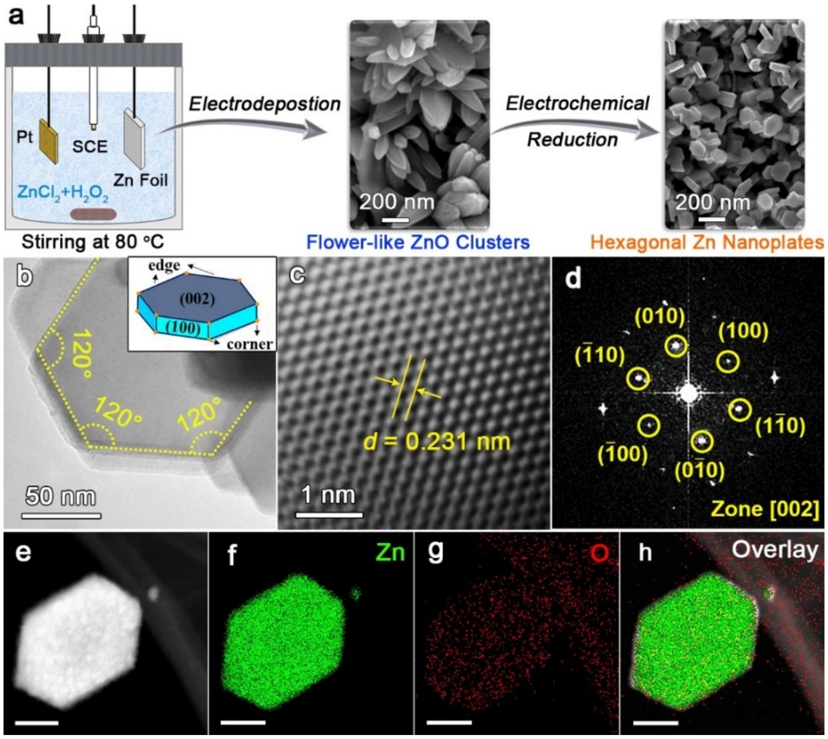

Figure 3.1 (a) Schematic diagram of the synthesis process for H-Zn-NPs; (b) low- and (c) high-resolution TEM images of H-Zn-NPs, the inset in b shows a schematic diagram of a typical hexagonal nanoplate; (d) the corresponding FFT pattern; (e) scanning TEM image and (f-h) the corresponding EDS mappings showing the elemental distribution of Zn and O (scale bar: 30 nm).

To acquire the structural property of H-Zn-NPs, TEM equipped with an EDS detector was performed and the image is shown in Figure 3.1b. Clearly, the TEM image of a typical hexagonal nanoplate shows a characteristic angle of 120°, well confirming the hexagonal nanostructure. A closer inspection of the high-resolution TEM image (Figure 3.1c) finds that the interplanar d-spacing value is 0.231 nm, which accords with the value for the (100) plane of hexagonal Zn crystal [18]. Besides, the well-ordered fast Fourier transformation (FFT) pattern (Figure 3.1d) further implies the pure crystalline structure of the as-prepared H-Zn-NPs, and the [002] zone axis indicates that the exposed hexagonal facet is Zn(002). Based on the hexagonal symmetry, it can be concluded that the prepared H-Zn-NPs are bounded by (100) and (002) facets. The EDS mappings (Figure 3.1e–h) further verify that no oxygen-containing species were formed on the nanoplate since the nanoplate and carbon substrate show almost the equivalent oxygen signals without distinguishable contrast. Likewise, XPS analysis indicates the identical surface chemical states of H-Zn-NPs and Zn foil since no obvious shifts of Zn 2p peaks are observed (Figure S3.5). The evidence collectively demonstrates the successful preparation of H-Zn-NPs without any impurity.

Using Zn foil as the reference, the electrocatalytic activity of H-Zn-NPs was evaluated in CO_2- or Ar-saturated 0.1 M $KHCO_3$ electrolyte within a custom-built cell separated by a Nafion 117 membrane. The cathodic polarization curves of all catalysts were recorded by linear sweep voltammetry (LSV) at a scan rate of 20 mV s^{-1}; all the applied potentials hereafter are with reference to the reversible hydrogen electrode (RHE). The current densities were calculated based on geometric area of the catalysts. To convincingly clarify the shape effect on the catalytic activity of H-Zn-NPs for CO_2RR, identical measurements were also conducted on similarly sized Zn nanoparticles (S-Zn-NPs; Figure S3.3). Remarkably, all catalysts show comparably higher current densities in CO_2-saturated media than in Ar-saturated media (Figure S3.6), indicating their activities for CO_2RR. Moreover, H-Zn-NPs exhibit a current density of 14.3 mA cm^{-2} at –1.26 V, which is roughly 2-fold higher than that of Zn foil and 4.5 mA cm^{-2} higher than that of S-Zn-NPs in the CO_2-saturated electrolyte (Figure 3.2a), suggesting that the enhanced catalytic activity over H-Zn-NPs may originate from the shape-controlled hexagonal nanostructures.

However, the current densities acquired from the LSV curves are not entirely derived from CO_2RR due to the simultaneous occurrence of HER during electrolysis. To distinguish CO_2RR and HER on H-Zn-NPs, potentiostatic CO_2 electrolyses were performed at potentials ranging from −0.66 to −1.26 V, and each potential was applied for 25 min (Figure S3.7). The gaseous products were quantitatively analyzed using an online gas chromatograph (GC) for 3 times (every 8 min) at each potential to obtain the average values. The results show that CO and H_2 are the only two products with a total FE of 98.8±1.5% over the entire potential range (Figure S3.8). Figure 4.2b exhibits the CO FEs as a function of potential. Apparently, H-Zn-NPs manifest the highest CO FE throughout the measured potential range and reach a remarkably higher maximum CO FE of 94.2% at –0.96 V as compared to S-Zn-NPs (71.5% at –0.96 V) and Zn foil (43.1% at –1.06 V). Additionally, H-Zn-NPs have a CO FE of 58.7% at the potential of −0.66 V, only 0.55 V higher than the theoretical equilibrium potential of −0.11 V [4], whereas the CO FEs of S-Zn-NPs and Zn foil are about half and one-quarter of the value, respectively. This indicates that the selectivity of CO_2RR is significantly enhanced by the well-designed H-Zn-NPs. More importantly, H-Zn-NPs exhibit considerably high selectivity with FEs over 85% for CO formation in a wide potential window ranging from –0.76 to –1.26 V. This evidence makes H-Zn-NPs stand out among the state-of-the-art Zn-based catalysts, since such a high selectivity has not been either achieved or observed previously in a broad potential window on these catalysts in bicarbonate electrolytes (Figure 3.2c and Table S3.1) [15-20, 22-24].

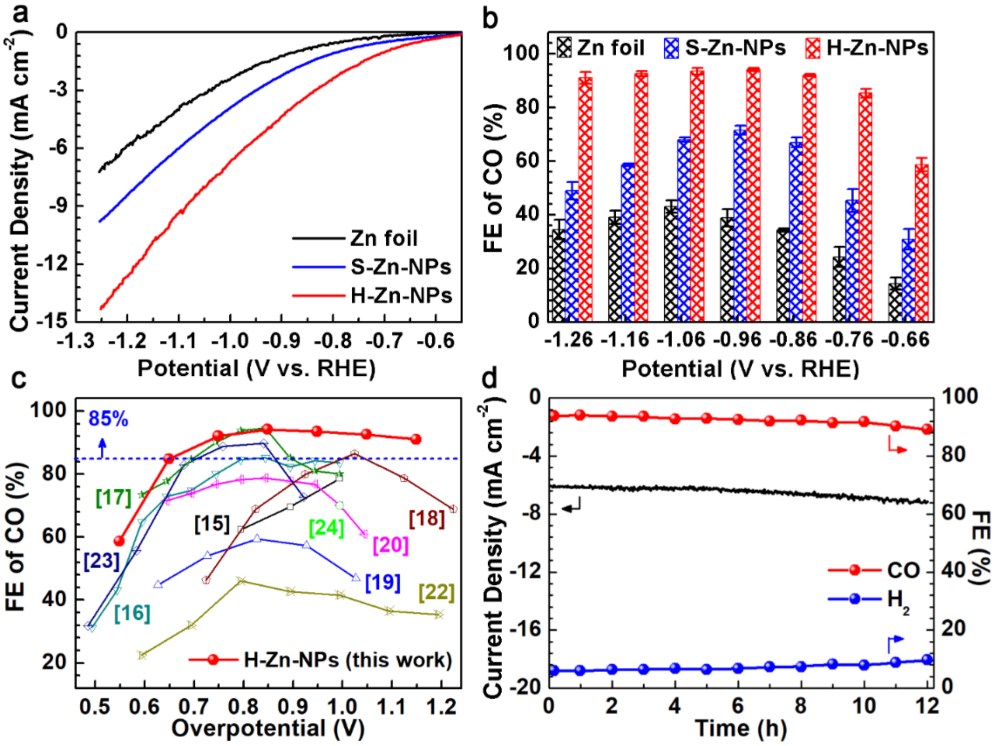

Figure 3.2 (a) LSV results in Ar- or CO_2-saturated 0.1 M $KHCO_3$ electrolyte; (b) CO FEs of Zn foil, S-Zn-NPs and H-Zn-NPs at various potentials; (c) comparison of overpotential-dependent CO FEs measured in bicarbonate electrolytes over H-Zn-NPs and other state-of-the-art Zn-based catalysts, including Zn dendrites [15], hexagonal Zn [16], porous Zn [17], multilayered Zn nanosheets [18], nanoscale Zn [19], reduced Zn [20], Zn nanoflakes [22], $Zn_{94}Cu_6$ foam [23], and 6.8 nm Zn nanoparticles [24]; (d) stability test for H-Zn-NPs at a potential of –0.96 V. The current densities shown in this figure were all calculated based on geometric area.

As another crucial criterion, the stability of H-Zn-NPs was examined by conducting electrolysis at a fixed potential of –0.96 V over an extended period of 12 h (Figure 3.2d). The recorded current density is slightly increased during the stability test. This variation may be attributed to the dissolution and redeposition of H-Zn-NPs during the prolonged operation, since dissolved Zn^{2+} has been identified to promote the reduction of CO_2 to CO [15, 25]. The crystal structure and the chemical state of H-Zn-NPs remain unchanged after the stability test, while a decrease in angular sharpness and the formation of small particles were observed (Figure S3.9). These evidences further confirm the dissolution and redeposition of Zn [25, 26]. In contrast, the product selectivity exhibits negligible degradation with CO FE remaining over 90%. This may be a compromise between morphological degradation and the formation of new active sites due to the redeposition of Zn [25, 26]. Additionally, the stability of H-Zn-NPs has been improved as compared to that of Zn foil (Figure S3.10). Therefore, H-Zn-NPs possess great potential as a promising CO_2RR electrocatalyst with superior CO selectivity and good stability.

To clearly reveal the shape effect on the CO_2RR catalytic activity, the CO partial current densities (j_{CO}) of various Zn catalysts were calculated (Figure 3.3a) based on steady-state current densities and CO FEs at various potentials. At the potential of –1.26 V, a j_{CO} of 12.9 mA cm^{-2} is obtained on H-Zn-NPs, which is about 2.7- and 5.1-fold higher than those on S-Zn-NPs and Zn foil, respectively. Moreover, the overpotential required for H-Zn-NPs to achieve a j_{CO} of ~2 mA cm^{-2} shifts positively by 0.15 V and 0.35 V as compared to those for S-Zn-NPs and Zn foil, respectively (Figure S3.11). The differences in j_{CO} and overpotential suggest that the catalytic activity for CO_2RR is significantly promoted by the distinctive hexagonal nanostructures. Remarkably, the j_{CO} values of H-Zn-NPs are larger than those of most reported Zn-based catalysts measured under similar conditions (Table S3.1) [17, 22, 24]. To exclude the influence of the surface area on the catalytic activity, the electrochemically active surface areas (ECSAs) of all catalysts were determined by measuring double-layer capacitance (C_{dl}, see Section 2.5 for details). The measured C_{dl} values of Zn foil, S-Zn-NPs and H-Zn-NPs are 0.335, 0.750 and 1.105 mF cm^{-2}, respectively (Figure S3.12). Therefore, the ECSA for H-Zn-NPs is estimated to be roughly 1.5 and 3.3 times higher than those for S-Zn-NPs and Zn foil. Therefore, the specific catalytic activity of H-Zn-NPs is calculated to be approximately 1.8-fold higher than that of S-Zn-NPs, implying the presence of intrinsically more active sites introduced by the special shape of H-Zn-NPs. This evidently confirms the shape-driven enhanced activity of H-Zn-NPs for CO_2RR.

As a critical parameter to evaluate conversion efficiency from electrical energy to target product at various overpotentials, the energy efficiencies (EEs) of all catalysts were calculated to further demonstrate the superiority of the shape-controlled H-Zn-NPs. The higher FE of H-Zn-NPs towards CO production, together with the comparatively lower overpotential, leads to remarkably higher EEs than S-Zn-NPs and Zn foil over the entire potential range (Figure 3.3b). Moreover, a maximum EE of 59.0% is achieved on H-Zn-NPs at a considerably low overpotential of 0.75 V, which outperforms most of the non-noble metal-based systems towards CO formation [3, 27, 28], and is even comparable with noble metal catalysts such as Pd nanoparticles [12] and triangular Ag nanoplates [9] (Table S3.2).

To gain deep insights into the reaction kinetics on the Zn catalysts, ECSA-corrected Tafel plots were explored, and the results are presented in Figure 3.3c. In contrast to the Tafel slopes of 148 mV dec^{-1} on S-Zn-NPs and 156 mV dec^{-1} on Zn foil, a lower Tafel slope of 132 mV dec^{-1} is found on H-Zn-NPs, more closer to the theoretical value of 118 mV dec^{-1}

for the initial one-electron transfer process [8]. This implies that the rate-determining step for CO_2RR over the Zn catalysts is the reduction of the adsorbed CO_2 to the key $CO_2^{\bullet-}$ intermediate, which normally requires high energy to change the polar of CO_2 molecules [29, 30]. Hence, the lowered Tafel slope of H-Zn-NPs is indicative of a promoted kinetics for the generation of $CO_2^{\bullet-}$ intermediate, as further confirmed by the results of electrochemical impedance spectroscopy (EIS) measurements in Figure 3.3d. As seen, the high-frequency intersections with the x-axis of all Nyquist plots are quite close, which means that the ohmic resistances (R_s, mainly from electrolyte and contact resistances) are reproducible in this study. The radius of Nyquist plots for H-Zn-NPs is apparently smaller than those for S-Zn-NPs and Zn foil, suggesting their lower charge-transfer resistance (R_{ct}, see Table S3.3 for fitted parameters) and thus a faster electron transfer process. Based on the above evidence, it is clear that the H-Zn-NPs could greatly promote the shape-dependent reaction kinetics for CO_2RR, leading to the highly active and selective CO_2RR.

The origins credited for the enhanced CO_2RR performance of H-Zn-NPs were further explored to better understand the reaction mechanism. The special architecture of H-Zn-NPs introduces more catalytically active sites relative to S-Zn-NPs and Zn foil, as inferred by the increased ECSA (Figure S3.12) [17]. This subsequently endows H-Zn-NPs with increased CO_2 adsorption capacity, as evidenced by the CO_2 adsorption isotherms in Figure 3.4a. Specifically, the amount of adsorbed CO_2 over H-Zn-NPs at 1 atm (1.97 cm^3 g^{-1}) is approximately 1.5 and 3 times higher than that over S-Zn-NPs (1.35 cm^3 g^{-1}) and that over Zn foil (0.66 cm^3 g^{-1}), respectively. Given the fact that CO_2 adsorption is the prerequisite for CO_2RR in aqueous media [31], the significantly increased CO_2 adsorption capacity of H-Zn-NPs ensures enough reactants for CO_2RR without serious concentration polarization.

Additionally, the work functions of H-Zn-NPs, S-Zn-NPs and Zn foil were determined by ultraviolet photoelectron spectroscopy (UPS; Figure S3.13). The results in Figure 3.4b indicate an obviously lower work function of H-Zn-NPs (3.66 eV) as compared to those of S-Zn-NPs (3.77 eV) and Zn foil (3.78 eV). The superior electronic properties of H-Zn-NPs contribute to a faster electron transfer [32], which is in good agreement with the EIS results. The adsorbed CO_2 is thus quickly reduced to $CO_2^{\bullet -}$ intermediate, which consequently results in the enhanced CO_2RR activity.

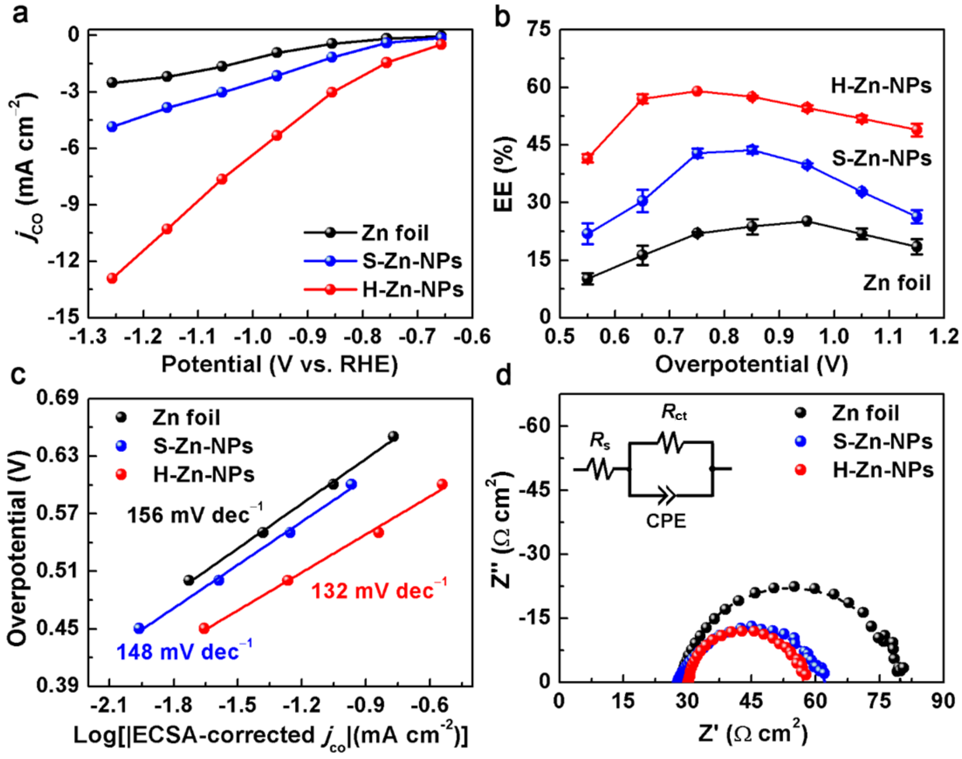

Figure 3.3 (a) Partial current densities (calculated based on geometric area) of CO at various potentials; (b) EE of Zn foil, S-Zn-NPs and H-Zn-NPs at various overpotentials; (c) Tafel plots of Zn foil, S-Zn-NPs and H-Zn-NPs and (d) Nyquist plots obtained at -0.96 V.

To further uncover the origins for the enhanced catalytic activity and high CO selectivity of H-Zn-NPs, DFT calculations were performed (see Section 3.5.1 for calculation details). It is well accepted that the reduction of CO_2 to CO mainly involves the following three elementary steps in aqueous media [6, 17]:

$$CO_2(g) + * + H^+(aq) + e^- \rightarrow *COOH \tag{3.1}$$

$$*COOH + H^+(aq) + e^- \rightarrow *CO + H_2O(l) \tag{3.2}$$

$$*CO \rightarrow CO(g) + * \tag{3.3}$$

where * denotes a catalytically active site. A highly selective catalyst for CO_2RR to CO should possess the catalytically active sites that can strongly bind *COOH to promote the second reduction step, but weakly adsorb the obtained *CO for product liberation. Meanwhile, the catalyst is also required to exhibit low binding affinity with *H to inhibit the competitive HER. From this perspective, the binding energies of the key intermediates, i.e., *COOH, *CO and *H, on the exposed Zn(100) and Zn(002) facets along with the edge and corner sites were calculated at –0.66 V (Figure S3.14 and Table S3.4). The Gibbs free energy (ΔG) diagrams for CO_2RR and HER were then constructed based on the computational hydrogen electrode model [33]. As shown in Figure 3.4c, the formation of *COOH (step 1) encounters large uphill energy barriers on Zn (100) and Zn(002) facets and hence, it is the rate-determining step for CO_2RR on the Zn facets. In contrast, *COOH is very stable on edge and corner sites with their respective energy releases of -0.31 and -0.01 eV due to the high binding affinities of low-coordinated atoms for the key intermediate (Table S3.5). It is inferred that bulk Zn requires a higher overpotential to initiate the CO_2 activation as compared to Zn nanostructures with a high density of edge and corner sites. However, the corner sites tend to overbind *CO and consequently decrease the product liberation rate. Moreover, they are more favorable for HER considering the much lower ΔG of *H (Figure S3.15) relative to that of *COOH (Figure 3.4c). On the other hand, the edge sites are preferable for CO_2RR to CO due to the lower ΔG of *CO relative to the ΔG of *H. Therefore, the well-recognized design principle for noble metals, i.e., increasing edge-to-corner ratio to enhance the CO_2RR activity and selectivity [6, 9, 34], is also applicable to Zn catalysts.

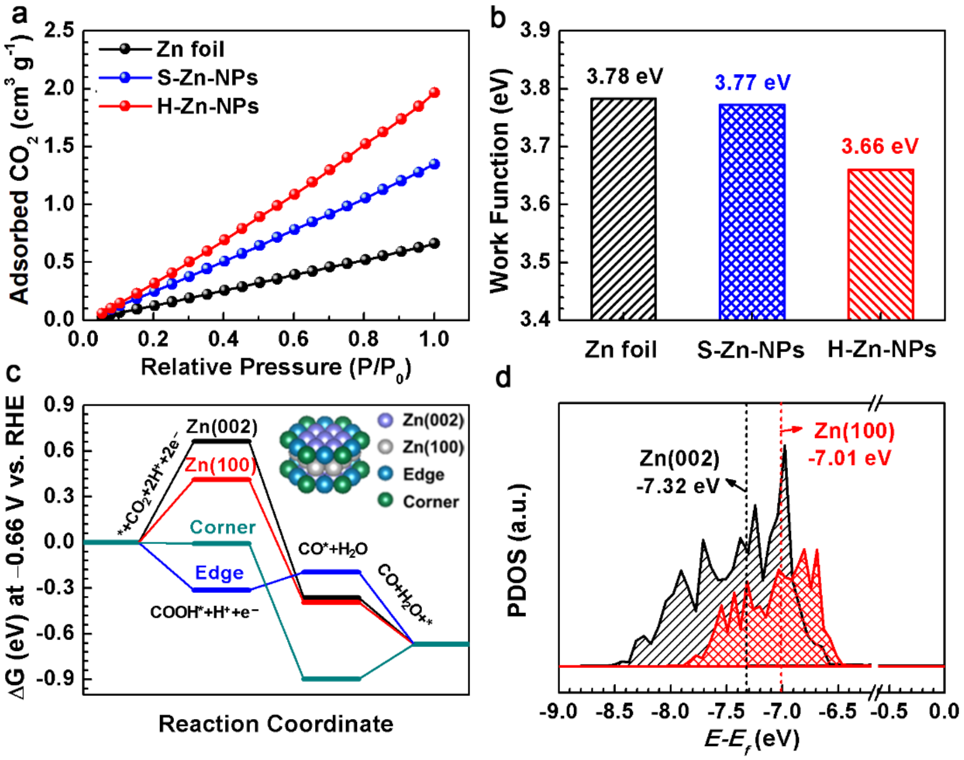

Figure 3.4 (a) CO_2 adsorption isotherms and (b) work functions of Zn foil, S-Zn-NPs and H-Zn-NPs; (c) Free energy diagrams for CO_2RR to CO on Zn(002), Zn(100), edge and corner sites at –0.66 V and (d) calculated PDOS of the surface Zn atoms of Zn(002) and Zn(100) facets.

Attention should also be paid to the Zn(100) and Zn(002) facets, which are predominant on the surface of H-Zn-NPs. The increase in ΔG for the formation of *COOH on Zn(100) facet is much lower than that on Zn(002) facet, indicating a higher catalytic activity of Zn(100) for CO_2RR. Furthermore, the partial densities of states (PDOS) of the surface atoms of Zn(100) and Zn(002) facets were calculated to determine the d-band center, as shown in Figure 3.4d.

It has been proven that the higher the d-band center relative to Fermi energy (E_F) level, the higher in energy the antibonding states are, and then the stronger the adsorption bond [35]. It is apparent that the d-band center of the surface Zn atom of Zn(100) is considerably higher than that of Zn(002). This demonstrates that Zn(100) has a stronger binding ability to the key intermediates, which thus results in lower free energy changes for CO evolution than that of Zn(002). Notably, H-Zn-NPs possess a higher percentage of exposed Zn(100) atoms as compared to S-Zn-NPs surrounded by all facets. The unique hexagonal shape of H-Zn-NPs points to the increased catalytic activity and CO selectivity, which is in good agreement with the experimental results.

Therefore, the superior CO_2RR performance of H-Zn-NPs collectively benefits from the enlarged ECSA, the lowered work function and the increased number of catalytically active sites that facilitate the CO_2RR to CO. According to the DFT results, the catalytic activity and the CO selectivity on Zn catalysts can be tuned by the percentages of catalytically active sites that are correlated to the shape of catalysts. To better our understanding on the shape-dependent catalytic activity of Zn catalysts, the percentages of various surface sites of hexagonal Zn structures as a function of diagonal length or thickness (α) were analyzed. The results (Figures S3.16 and S3.17) imply that the CO_2RR catalytic activity on Zn catalysts can be further enhanced by engineering a hexagonal structure with a small value of α, thus maximizing the percentages of energetically favorable Zn(100) facets and edge sites. This deduction can be evidenced by the decreased EE of CO evolution with a larger value of α as observed on H-Zn-NPs, sub-microscale hexagonal Zn [16] and Zn nanosheets [18] (Figure S3.18). The results in this study provide a scientific basis for structure-versus-performance optimization of Zn-based catalysts in the application of electrochemical CO_2RR to produce CO.

3.3 Conclusions

In summary, we successfully synthesized H-Zn-NPs enclosed by Zn(002) and Zn(100) facets, and explored their shape-driven CO_2RR. Compared with Zn foil and S-Zn-NPs, H-Zn-NPs exhibit remarkably enhanced catalytic activity and CO selectivity. More importantly, H-Zn-NPs show high selectivity with CO FEs of over 85% in a wide potential window ranging from –0.76 to –1.26 V, and reach a maximum value of 94.2% at –0.96 V, which outperforms previously reported Zn-based catalysts. The significantly enhanced CO_2RR performance largely depends on the enlarged ECSA, the lowered work function, and the increased numbers of Zn(100) and edge atoms. These findings can serve as an important stepping stone in advancing our knowledge on CO_2RR mechanism over Zn catalysts and providing new insights into the design strategy for low-cost and efficient electrocatalysts for CO_2RR.

3.4 References

[1] J. Rogelj, D. Huppmann, V. Krey, et al., A new scenario logic for the Paris Agreement long-term temperature goal, Nature 573 (2019) 357-363.

[2] J.M. Spurgeon, B. Kumar, A comparative technoeconomic analysis of pathways for commercial electrochemical CO_2 reduction to liquid products, Energy Environ. Sci. 11 (2018) 1536-1551.

[3] Z.-L. Wang, C. Li, Y. Yamauchi, Nanostructured nonprecious metal catalysts for electrochemical reduction of carbon dioxide, Nano Today 11 (2016) 373-391.

[4] J. Qiao, Y. Liu, F. Hong, et al., A review of catalysts for the electroreduction of carbon dioxide to produce low-carbon fuels, Chem. Soc. Rev. 43 (2014) 631-75.

[5] A.J. Martín, G.O. Larrazábal, J. Pérez-Ramírez, Towards sustainable fuels and chemicals through the electrochemical reduction of CO_2: lessons from water electrolysis, Green Chem. 17 (2015) 5114-5130.

[6] W. Zhu, R. Michalsky, O. Metin, et al., Monodisperse Au nanoparticles for selective electrocatalytic reduction of CO_2 to CO, J. Am. Chem. Soc. 135 (2013) 16833-16836.

[7] W. Zhu, Y.-J. Zhang, H. Zhang, et al., Active and selective conversion of CO_2 to CO on ultrathin Au nanowires, J. Am. Chem. Soc. 136 (2014) 16132-16135.

[8] Y. Chen, C.W. Li, M.W. Kanan, Aqueous CO_2 reduction at very low overpotential on oxide-derived Au nanoparticles, J. Am. Chem. Soc. 134 (2012) 19969-19972.

[9] S. Liu, H. Tao, L. Zeng, et al., Shape-dependent electrocatalytic reduction of CO_2 to CO on triangular silver nanoplates, J. Am. Chem. Soc. 139 (2017) 2160-2163.

[10] Q. Lu, J. Rosen, Y. Zhou, et al., A selective and efficient electrocatalyst for carbon dioxide reduction, Nat. Commun. 5 (2014) 3242.

[11] S. Liu, X.-Z. Wang, H. Tao, et al., Ultrathin 5-fold twinned sub-25 nm silver nanowires enable highly selective electroreduction of CO_2 to CO, Nano Energy 45 (2018) 456-462.

[12] D. Gao, H. Zhou, J. Wang, et al., Size-dependent electrocatalytic reduction of CO_2 over Pd nanoparticles, J. Am. Chem. Soc. 137 (2015) 4288-4291.

[13] D. Gao, H. Zhou, F. Cai, et al., Pd-containing nanostructures for electrochemical CO_2 reduction reaction, ACS Catal. 8 (2018) 1510-1519.

[14] Y. Hori, K. Kikuchi, S. Suzuki, Production of CO and CH_4 in electrochemical reduction of CO_2 at metal electrodes in aqueous hydrogencarbonate solution, Chem. Lett. 14 (1985) 1695-1698.

[15] J. Rosen, G.S. Hutchings, Q. Lu, et al., Electrodeposited Zn dendrites with enhanced CO selectivity for electrocatalytic CO_2 reduction, ACS Catal. 5 (2015) 4586-4591.

[16] W.D. Hye, S. Hyeyoung, K. Jaekang, et al., Highly efficient, selective, and stable CO_2 electroreduction on a hexagonal Zn catalyst, Angew. Chem. Int. Ed. 55 (2016) 9297-9300.

[17] W. Luo, J. Zhang, M. Li, et al., Boosting CO production in electrocatalytic CO_2 reduction on highly porous Zn catalysts, ACS Catal. (2019) 3783-3791.

[18] T. Zhang, X. Li, Y. Qiu, et al., Multilayered Zn nanosheets as an electrocatalyst for efficient electrochemical reduction of CO_2, J. Catal. 357 (2018) 154-162.

[19] F. Quan, D. Zhong, H. Song, et al., A highly efficient zinc catalyst for selective electroreduction of carbon dioxide in aqueous NaCl solution, J. Mater. Chem. A 3 (2015) 16409-16413.

[20] D.L.T. Nguyen, M.S. Jee, D.H. Won, et al., Selective CO_2 reduction on zinc electrocatalyst: the effect of zinc oxidation state induced by pretreatment environment, ACS Sustain. Chem. Eng. 5 (2017) 11377-11386.

[21] Z. Wang, G. Yang, Z. Zhang, et al., Selectivity on etching: creation of high-energy facets on copper nanocrystals for CO_2 electrochemical reduction, ACS Nano 10 (2016) 4559-4564.

[22] B. Qin, Y. Li, H. Fu, et al., Electrochemical reduction of CO_2 into tunable syngas production by regulating the crystal facets of earth-abundant Zn catalyst, ACS Appl. Mater. Interfaces 10 (2018) 20530-20539.

[23] P. Moreno-García, N. Schlegel, A. Zanetti, et al., Selective electrochemical reduction of CO_2 to CO on Zn-based foams produced by Cu^{2+} and template-assisted electrodeposition, ACS Appl. Mater. Interfaces 10 (2018) 31355-31365.

[24] H.S. Jeon, I. Sinev, F. Scholten, et al., Operando evolution of the structure and oxidation state of size-controlled Zn nanoparticles during CO_2 electroreduction, J. Am. Chem. Soc. 140 (2018) 9383-9386.

[25] S. Ikeda, A. Hattori, K. Ito, et al., Zinc ion effect on the electrochemical reduction of carbon dioxide at zinc electrode in aqueous solutions, Electrochem. 67 (1999) 27-33.

[26] Y. Hori, Modern aspects of electrochemistry 42, Springer New York, 2008, pp. 89-189.

[27] G. Zhigang, K. Xiangdong, C. Weiwei, et al., Oxygen vacancies in ZnO nanosheets enhance CO_2 electrochemical reduction to CO, Angew. Chem. Int. Ed. 57 (2018) 6054-6059.

[28] S. Rasul, D.H. Anjum, A. Jedidi, et al., A highly selective copper–indium bimetallic electrocatalyst for the electrochemical reduction of aqueous CO_2 to CO, Angew. Chem. Int. Ed. 54 (2015) 2146-2150.

[29] R. Chaplin, A. Wragg, Effects of process conditions and electrode material on reaction pathways for carbon dioxide electroreduction with particular reference to formate formation, J. Appl. Electrochem. 33 (2003) 1107-1123.

[30] H.-K. Lim, H. Shin, W.A. Goddard, et al., Embedding covalency into metal catalysts for efficient electrochemical conversion of CO_2, J. Am. Chem. Soc. 136 (2014) 11355-11361.

[31] R. Kortlever, J. Shen, K.J.P. Schouten, et al., Catalysts and reaction pathways for the electrochemical reduction of carbon dioxide, J. Phys. Chem. Lett. 6 (2015) 4073-4082.

[32] M. Asadi, K. Kim, C. Liu, et al., Nanostructured transition metal dichalcogenide electrocatalysts for CO_2 reduction in ionic liquid, Science 353 (2016) 467-470.

[33] W.J. Durand, A.A. Peterson, F. Studt, et al., Structure effects on the energetics of the electrochemical reduction of CO_2 by copper surfaces, Surf. Sci. 605 (2011) 1354-1359.

[34] S. Back, M.S. Yeom, Y. Jung, Active sites of Au and Ag nanoparticle catalysts for CO_2 electroreduction to CO, ACS Catal. 5 (2015) 5089-5096.

[35] J.K. Nørskov, F. Abild-Pedersen, F. Studt, et al., Density functional theory in surface chemistry and catalysis, Proc. Natl. Acad. Sci. 108 (2011) 937-943.

3.5 Supporting information

3.5.1 DFT calculations

Density functional theory (DFT) calculations were performed using Vienna Ab initio Simulation Package [S1-3]. Electron-ion interactions and exchange-interaction effect were treated with projector-augmented plane-wave method [S4]. Perdew-Burke-Ernzerhof generalized gradient approximation function was employed to model the exchange-correlation interactions [S5]. A plane-wave cutoff energy of 450 eV was set and spin polarization was selected for all the computations.

Optimization of Zn unit cell was carried out using a k point sampling of Monkhorst-Pack (18×18×18) [S6]. Zn (002) and Zn (100) surfaces modeled with 4×4×4 and 4×2×4 atom slabs, respectively, were constructed based on the optimized unit cell and at least 15 Angstrom of vacuum layers were added in order to avoid the interaction between neighboring slabs. Additionally, a hexagonal Zn cluster with 50 atoms located in the center of a 25×25×25 box was built to simulate the edge and corner sites.

For surface structure optimization calculations, k points sampling was switched to (5×5×1) for both Zn (002) and Zn (100) surfaces. During optimization, only the adsorbate and two top atomic layers were relaxed while the remaining layers were fixed. Relaxation of degree of ions was not terminated until a maximum force component of 0.05 eV/Angstrom achieved. Different adsorption sites and geometries were considered and the one with the lowest adsorption energy was selected for subsequent calculations.

For cluster structure optimization calculations, after fully relaxing a complete clean cluster without any adsorbate, a truncated half model was utilized for subsequent geometry optimization of cluster with adsorbates in order to achieve a balance between accuracy and efficiency. Atoms at the bottom of truncated half model were fixed while adsorbate and remaining Zn atoms were fully relaxed. The k point sampling was set at (1×1×1) and only Gamma point was included for Zn cluster. Fermi-level smearing of 0.1 eV was set for unit cell, surface and cluster structure optimization calculations while for gas-phase species it was adjusted to 0.01 eV. Different adsorption sites and geometries were considered and the one with the lowest adsorption energy was selected for subsequent calculations.

To build Gibbs free energy diagram, computational hydrogen electrode (CHE) model was used where each electrochemical reaction step is treated as a simultaneous transfer of the proton-electron pair as a function of the applied potential [S7]. Gibbs free energies at 298.15 K for relevant species were calculated with the expression [S8]:

$$G=E_{\mathrm{DFT}}+E_{\mathrm{ZPE}}+\int C_{\mathrm{p}}\mathrm{d}T-TS \tag{S3.1}$$

where E_{DFT} is the DFT calculated electronic energy in VASP, E_{ZPE} is the zero-point vibrational energies, T is temperature (298.15K), $\int C_{\mathrm{p}}\mathrm{d}T$ is the enthalpic correction and TS is the entropy contribution. PV contributions was neglected. 3N freedom degrees were treated as frustrated harmonic vibrations to E_{ZPE} and enthalpy correction, entropy contribution was calculated by proposed standard method and transferred to thermodynamic data at room temperature [S9]. E_{ZPE}, $\int C_{\mathrm{p}}\mathrm{d}T$ and TS are all functions of vibration frequencies of ions. The reaction mechanisms of the reduction of CO_2 to CO are shown as below,

$$CO_2(g) + * + 2H^+(aq) + 2e^- \leftrightarrow *COOH + H^+(aq) + e^- \tag{S3.2}$$

$$*COOH + H^+(aq) + e^- \leftrightarrow *CO + H_2O(l) \tag{S3.3}$$

$$*CO + H_2O(l) \leftrightarrow CO(g) + * + H_2O(l) \tag{S3.4}$$

where * means the corresponding surface where molecules or transition state species adsorbed on. Taking the initial state as the reference, the Gibbs free energy change of each step can be expressed by the following equations,

$$\Delta G[*\mathrm{COOH}] = G[*\mathrm{COOH}] - (G[*] + G[\mathrm{CO_2}] + G[\mathrm{H^+} + \mathrm{e^-}]) \tag{S3.5}$$

$$\Delta G[*\mathrm{CO}] = G[*\mathrm{CO}] + G[\mathrm{H_2O}] - \left(G[*] + G[\mathrm{CO_2}] + 2\times G\left[\mathrm{H^+}+\mathrm{e^-}\right]\right) \tag{S3.6}$$

$$\Delta G[\mathrm{CO}] = G[\mathrm{CO}] + G[\mathrm{H_2O}] - \left(G[\mathrm{CO_2}]+2\times G\left[\mathrm{H^+}+\mathrm{e^-}\right]\right) \tag{S3.7}$$

Combing hydrogen evolution reaction (HER) mechanism with CHE model, taking the initial state as reference, the Gibbs free energy change of each step for HER are represented below,

$$\Delta G[*\mathrm{H}] = G\left[\mathrm{H^*}\right] - \left(G[*] + G\left[\mathrm{H^+}+\mathrm{e^-}\right]\right) \tag{S3.8}$$

$$\mathrm{e}U = 0.5 \times G[\mathrm{H_2}] - G\left[\mathrm{H^+}+\mathrm{e^-}\right] \tag{S3.9}$$

where U represents the external applied voltage as the driven force for electroreduction. In this work, the minimum applied potential of –0.66 V was selected as the value of U. All the relevant thermodynamic data used to build Gibbs free energy diagrams is listed in Table S3.4.

To further explore the facet effect on the CO_2RR catalytic activity over Zn, partial density of states (PDOS) of d orbital for the optimized Zn (002) and Zn (100) surfaces was extracted and plotted. The k point sampling for the surfaces is (15×15×1). Dipole correction along z-direction was applied. Relevant structure models listed in this paper were built and visualized with package of Visualization for Electronics and Structural Analysis (VESTA) Ver. 3.4.0.

3.5.2 Supporting figures

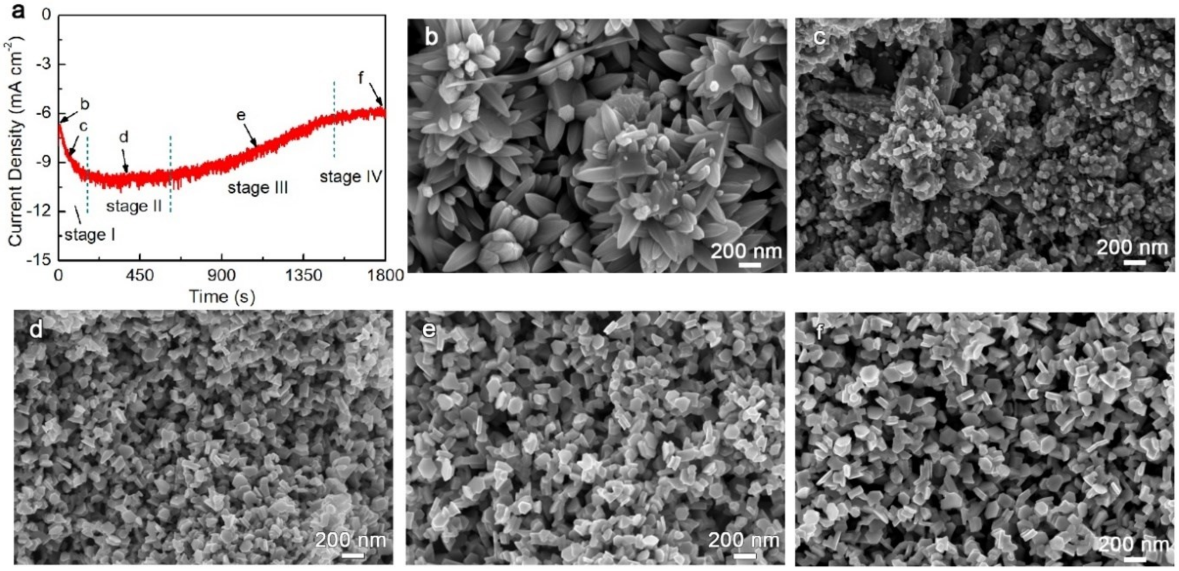

Figure S3.1 (a) Records of current density with time during the reduction of H-Zn-NPs at –0.96 V vs. RHE in CO_2-saturated 0.1 M $KHCO_3$ electrolyte; SEM images of H-Zn-NPs after electrochemically reduced for (b) 0 s, (c) 60 s, (d) 400 s, (e) 1100 s and (f) 1800 s.

Four forming stages can be identified based on the variation of current density recorded during the reduction of ZnO clusters, as shown in Figure S3.1a. The SEM images of original ZnO clusters and the samples reduced for different times (at various forming stages) are shown in Figure S3.1b-f. At the first stage (0-150 s), the absolute current density dramatically increases due to the rapid reduction of surface ZnO clusters (Figure S3.1b) to small hexagonal nanoplates (Figure S3.1c). After all the exposed ZnO clusters are reduced, the current density becomes steady (stage II, 150-600 s), and meanwhile, the reduced hexagonal structures gradually grow (Figure S3.1d). With continued consumption of ZnO, the current density drops slowly (stage III, 600-1500 s). At this stage, the particle size of the hexagonal structures continues to increase (Figure S3.1e). When the ZnO has been depleted, the current density becomes steady again (stage IV, after 1500 s), and hexagonal Zn nanoplates with certain particle sizes are formed (Fgiure S3.1f). During the following potentiostatic measurements (Figure S3.7), no cathodic peaks can be observed, indicating that all the ZnO has been reduced.

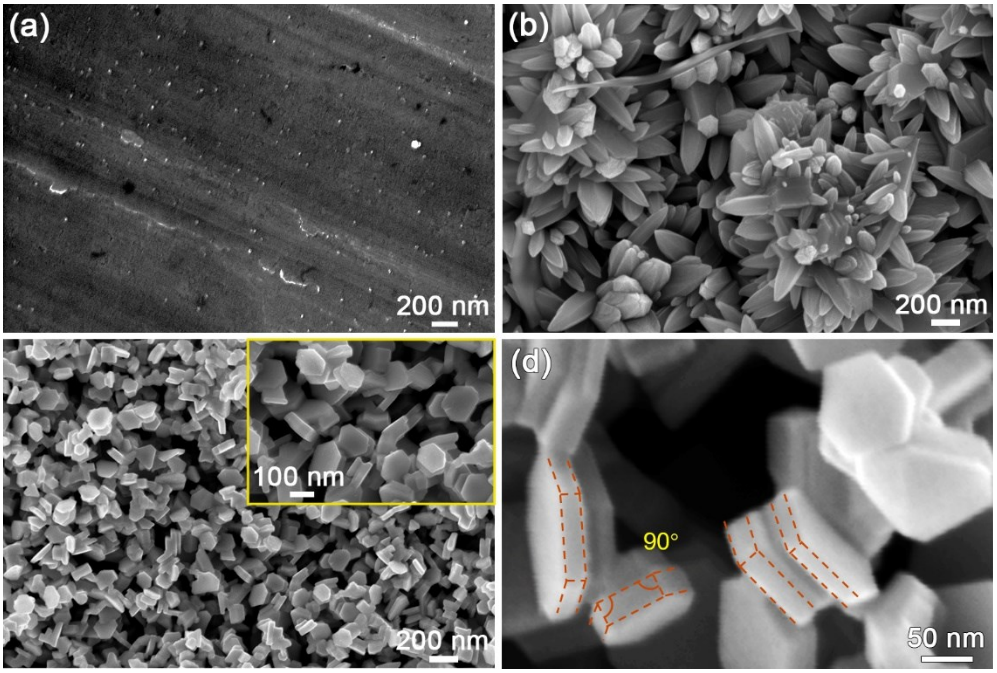

Figure S3.2 SEM images of (a) Zn foil, (b) flower-like ZnO clusters prepared by electrodeposition, (c) H-Zn-NPs. and (d) a magnified SEM image of H-Zn-NPs showing the interfacial angles between {100} and {002} facets.

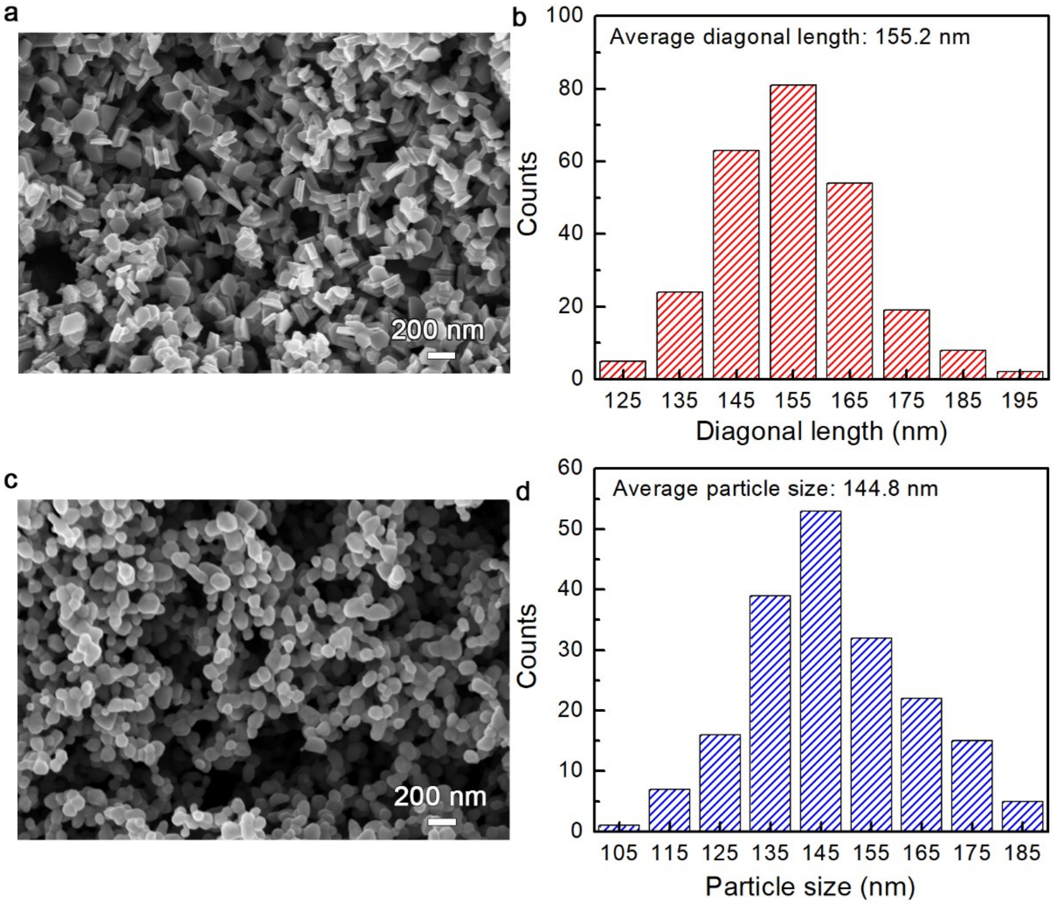

Figure S3.3 (a) SEM image of H-Zn-NPs and (b) the corresponding diagonal length distribution; (c) SEM image of S-Zn-NPs and (d) the corresponding particle size distribution.

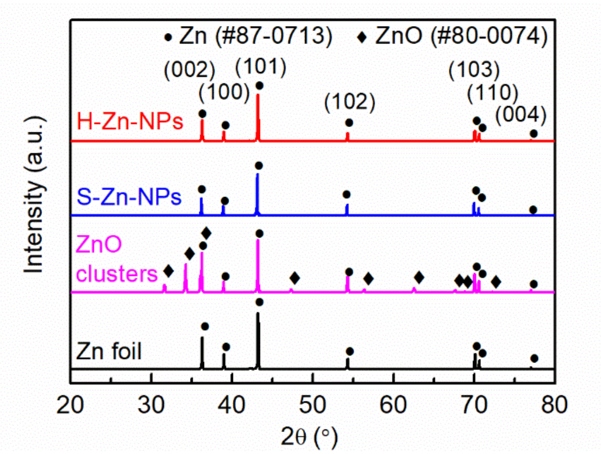

Figure S3.4 XRD patterns of Zn foil, ZnO clusters, S-Zn-NPs and H-Zn-NPs.

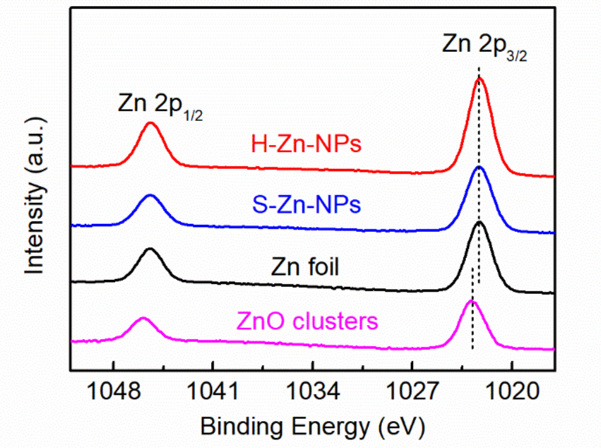

Figure S3.5 XPS spectra of Zn 2p for ZnO clusters, Zn foil, S-Zn-NPs and H-Zn-NPs.

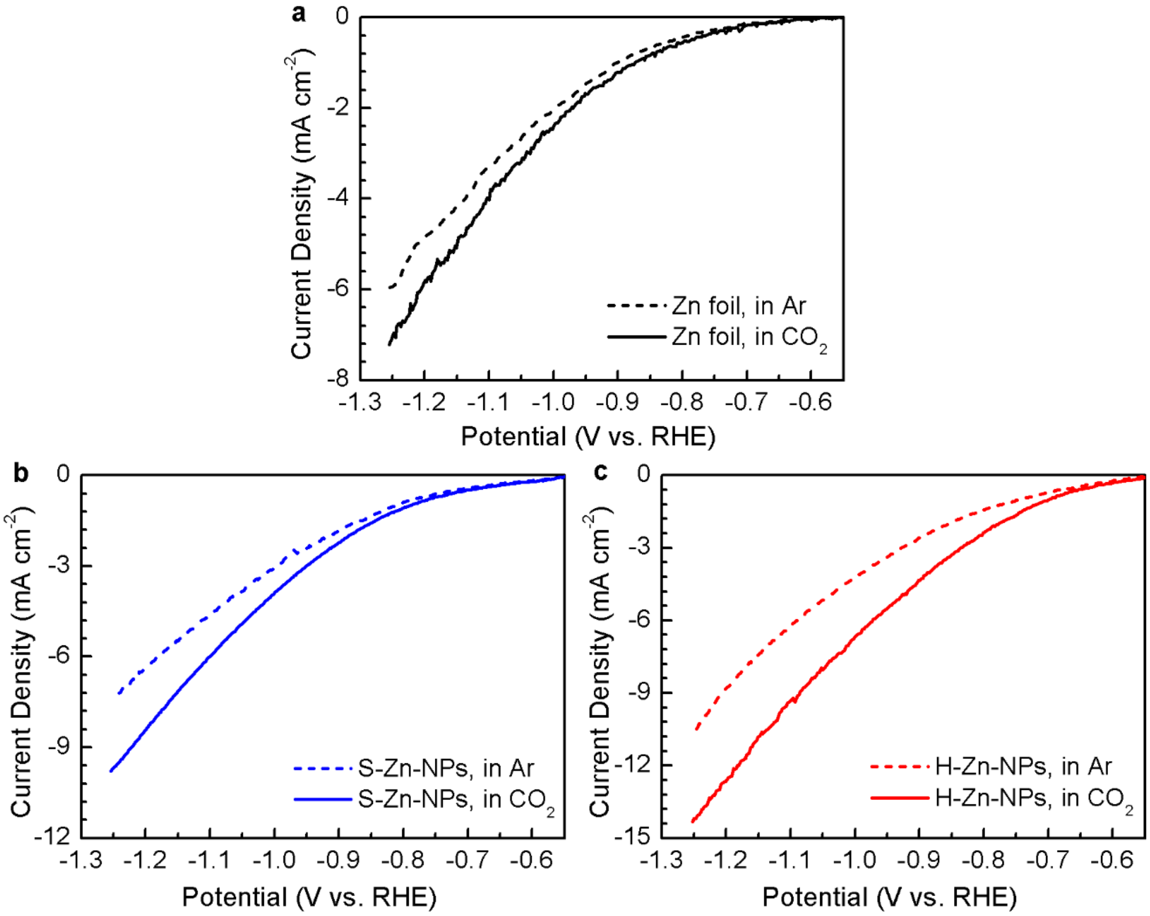

Figure S3.6 LSV results of (a) Zn foil, (b) S-Zn-NPs, and (c) H-Zn-NPs in Ar- or CO_2-saturated 0.1 M $KHCO_3$ electrolyte.

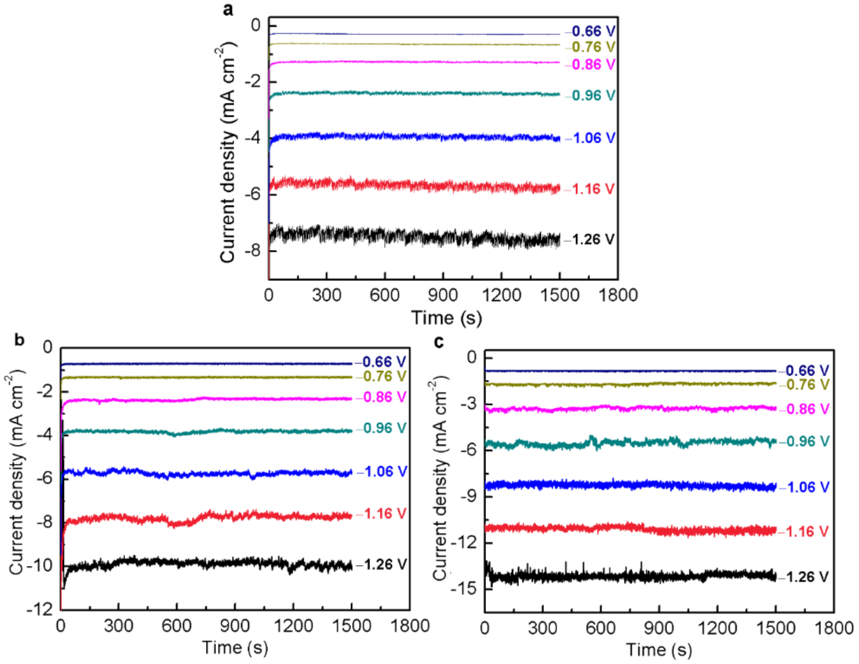

Figure S3.7 Plots of current densities as a function of time for (a) Zn foil, (b) S-Zn-NPs and (c) H-Zn-NPs at −0.66 V to −1.26 V vs. RHE in CO_2-saturated 0.1 M $KHCO_3$ electrolyte.

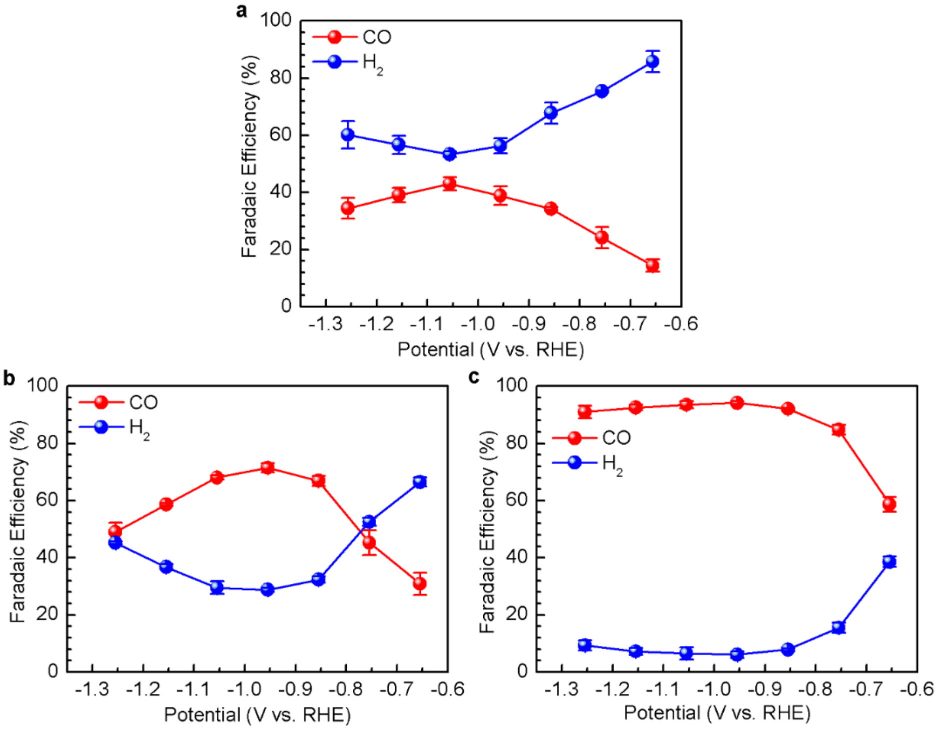

Figure S3.8 FEs of gaseous products over (a) Zn foil, (b) S-Zn-NPs and (c) H-Zn-NPs at different potentials.

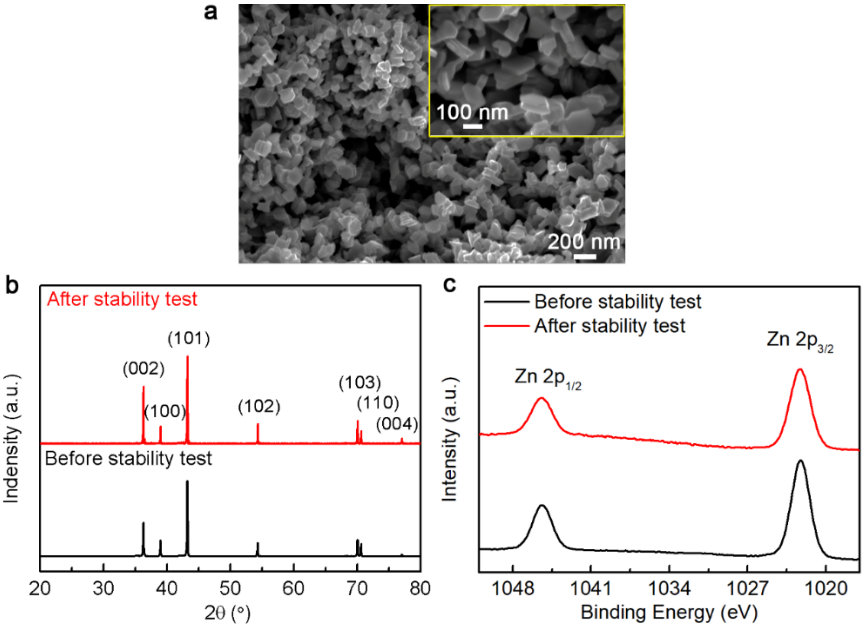

Figure S3.9 (a) SEM image, (b) XRD pattern and (c) XPS spectra of Zn 2p for H-Zn-NPs after the stability test of 12 h.

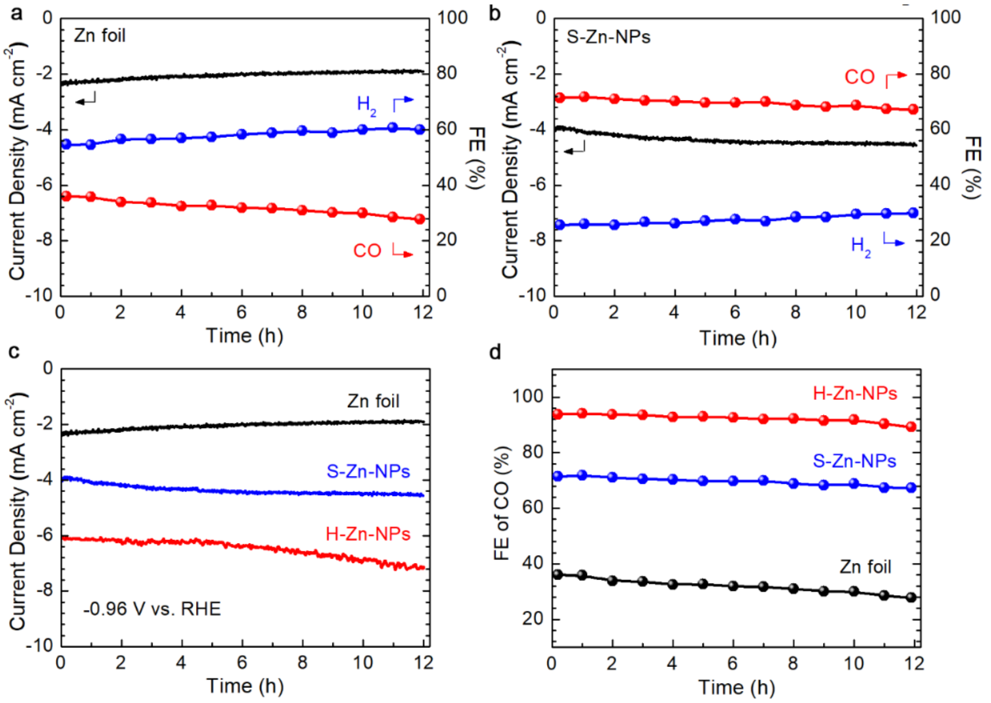

Figure S3.5 Stability tests for (a) Zn foil and (b) H-Zn-NPs at a potential of –0.96 V, and comparisons of (c) current densities and (d) CO FEs of Zn foil, S-Zn-NPs and H-Zn-NPs during the stability tests.

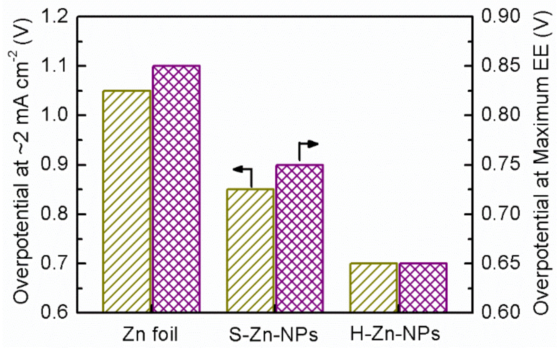

Figure S3.6 Overpotentials at j_{CO} of ~2 mA cm^{-2} and at the maximum EE over Zn foil, S-Zn-NPs and H-Zn-NPs.

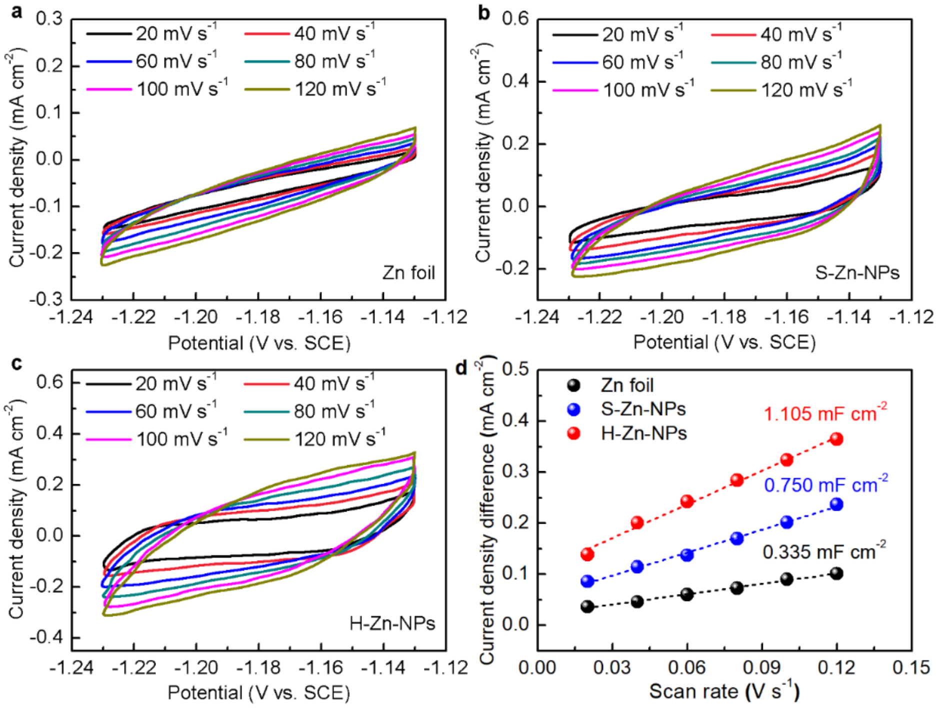

e

Electrodes	C_{dl} (mF cm^{-2})	R_f
Zn foil	0.335	1
S-Zn-NPs	0.750	2.24
H-Zn-NPs	1.105	3.30

Figure S3.7 CVs of (a) Zn foil, (b) S-Zn-NPs and (c) H-Zn-NPs with a potential range from –1.13 to –1.23 V vs. SCE in an Ar-saturated 0.5 M Na_2SO_4 electrolyte; (d) charging current density difference plotted against scan rates and (e) calculated double layer capacitance (C_{dl}) and roughness factors (R_f).

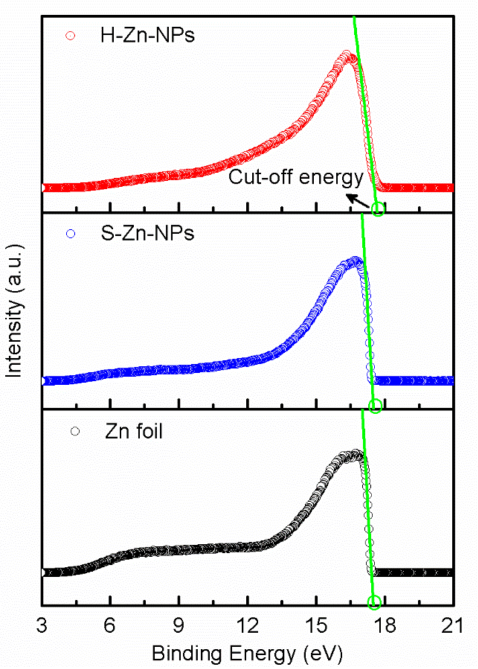

Figure S3.8 UPS plots of Zn foil, S-Zn-NPs and H-Zn-NPs.

The work function of the sample (Φ_s) can be calculated by $\Phi_s = h\nu - E_F$, where $h\nu$ is the exciting photo energy (i.e., 21.2 eV), E_F is the Fermi edge derived by extrapolating the cut-off energies to Vbias = 0.

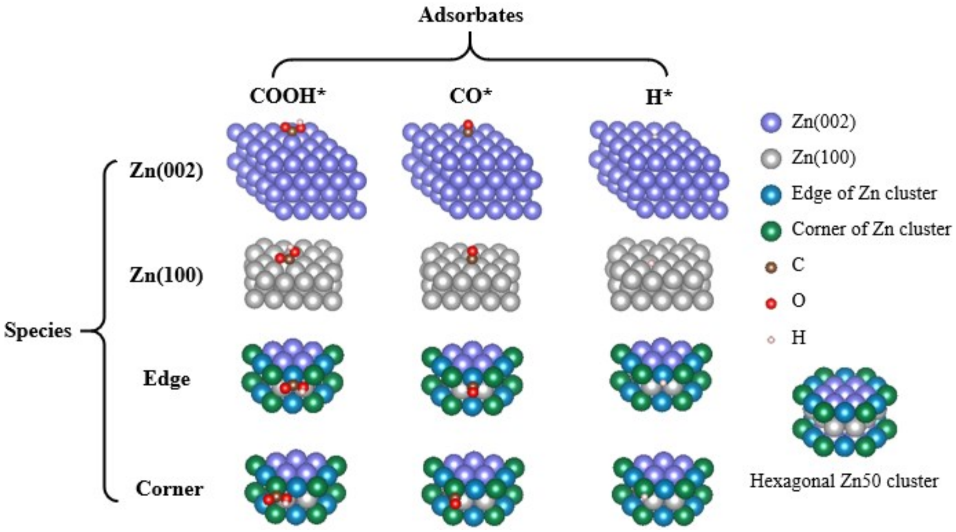

Figure S3.9 Atomistic structures optimized for COOH*, CO* and H* adsorbed on various surface sites of Zn.

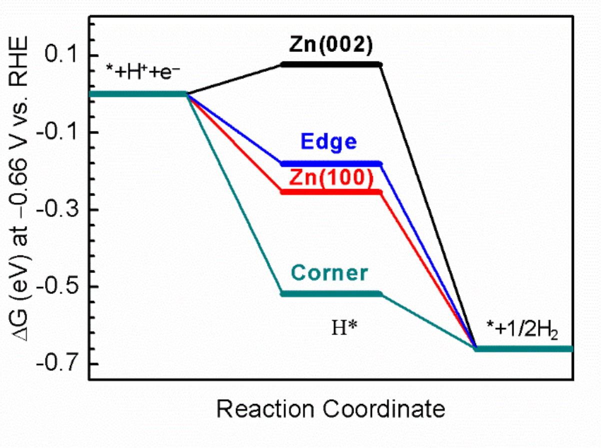

Figure S3.10 Free energy diagram for HER on Zn(002), Zn(100), edge and corner sites at –0.66 V.

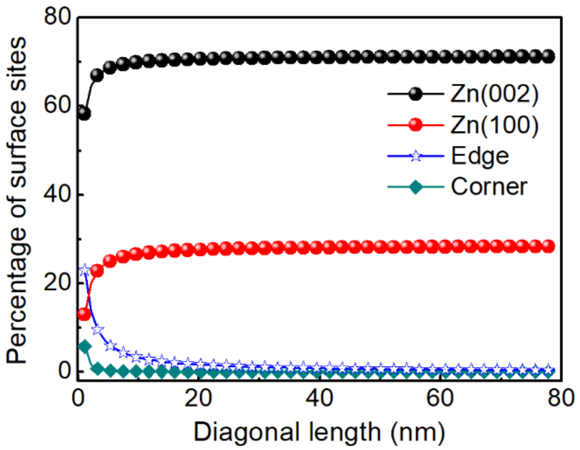

Figure S3.16 Percentages of surface sites on hexagonal Zn plates with a α value of 5 as a function of diagonal length.

According to the SEM results (Figures S3.2 and S3.3), the average diagonal length (D) of the synthesized H-Zn-NPs is about 150 nm, and the thickness is around 30 nm. Therefore, the ratio of diagonal length to thickness, denoted as α, is 5 for H-Zn-NPs. To investigate the diagonal length (size)-dependent catalytic activity, the percentages of surface sites on hexagonal Zn plates with an α value of 5 were calculated at different diagonal lengths.

Likewise, the percentages of surface sites on hexagonal Zn structures with different α values were calculated to study the thickness-dependent catalytic activity.

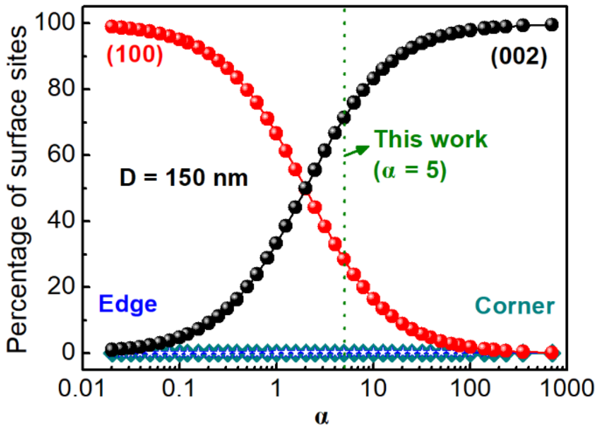

Figure S3.17 Percentages of surface sites on hexagonal Zn structures with a diagonal length (D) of 150 nm as a function of the ratio of diagonal length to thickness (α).

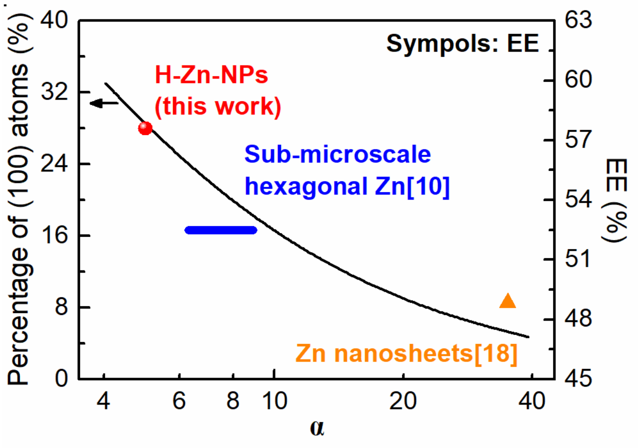

Figure S3.18 Comparisons of the calculated EE for CO evolution and the ratio of diagonal length to thickness (α) over H-Zn-NPs, sub-microscale hexagonal Zn [S10], and hexagonal Zn nanosheets [S11].

Figure S34.16 suggests that decreasing the diagonal length of hexagonal Zn plates contributes to an increase in the percentage of edge sites which are considerably active for CO_2RR according to the DFT results. Therefore, the catalytic activity of H-Zn-NPs can be further enhanced by decreasing the diagonal length. When the diagonal length of hexagonal Zn structures is fixed at 150 nm, as shown in Figure S3.17, the percentages of edge and corner sites (less than 1%) vary little with the thickness. However, increasing the thickness (i.e., decreasing the value of α) can obviously increase the percentage of Zn(100) facets, whereas the percentage of Zn(002) facets decreases accordingly. Namely, a smaller α of hexagonal Zn structures leads to a higher facet ratio of Zn(100)/Zn(002), which consequently promotes the activation of CO_2 to *COOH based on the results in Figure 3.4c and eventually results in enhanced catalytic activity for CO_2RR. This can be evidenced by comparing the EEs for CO evolution and the value of α over H-Zn-NPs, sub-microscale hexagonal Zn [S10], and hexagonal Zn nanosheets [S11] (Figure S3.18). Apparently, the EE over these hexagonal Zn structures tends to decrease with a larger α value, and such a tendency accords well with curve of the percentages of surface Zn(100) atoms. Hence, it can be deduced that hexagonal Zn structures with a small α value (e.g., Zn wires) should have substantial numbers of catalytically active sites for CO_2RR, which would favor the efficient conversion of CO_2 to CO.

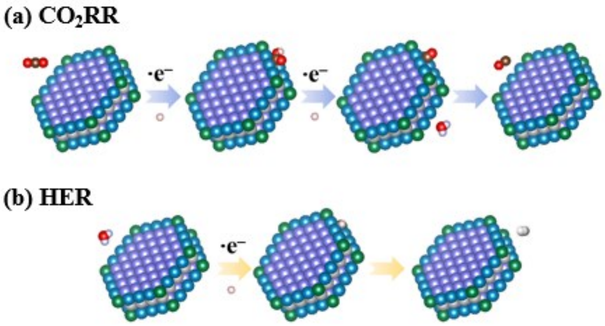

Figure S3.19 Models for each elementary step during (a) CO_2RR and (b) HER over hexagonal Zn nanoplates.

3.5.3 Supporting tables

Table S3.1 Comparison of CO_2RR performance over H-Zn-NPs and other state-of-the-art Zn-based catalysts in bicarbonate electrolytes.

Catalysts	Electrolyte	*E* (V vs. RHE)	j_{co} (mA cm^{-2})	FE of CO	Ref.
H-Zn-NPs	0.1 M $KHCO_3$	–1.26	–12.9	91.0%	This work
		–1.16	–10.3	92.6%	
		–1.06	–7.6	93.5%	
		–0.96	–5.3	94.2%	
		–0.86	–3.0	92.1%	
		–0.76	–1.4	85.3%	
Hexagonal Zn	0.5 M $KHCO_3$	–0.95	–12.7	85.4%	[S10]
Zn nanosheets	0.5 M $NaHCO_3$	–1.13	–5.2	86%	[S11]
6.8 nm Zn NPs	0.1 M $KHCO_3$	–1.10	–2.9	~70%	[S12]
Zn nanoflake	0.1 M $KHCO_3$	–0.90	–4.9	~43%	[S13]
Porous Zn	0.1 M $KHCO_3$	–0.95	–12.7	~95%	[S14]
$Zn_{94}Cu_6$ foam	0.5 M $KHCO_3$	–0.95	–7.9	90%	[S15]
Nanoscale Zn	0.5 M $NaHCO_3$	–0.93	–6.0	57%	[S16]
Zn dendrites	0.5 M $NaHCO_3$	–1.10	–13.0	79%	[S17]
Reduced Zn	0.5 M $KHCO_3$	–0.90	–5.1	77.8%	[S18]

Table S3.2 Comparison of FEs and EEs for the CO_2RR to CO over various catalysts in bicarbonate electrolytes.

Catalysts	***E* (V vs. RHE)**	**η (V)**	**FE of CO**	**EE of CO**	**Ref.**
H-Zn-NPs	-0.86	0.75	92.1	59.0	This work
Zn dendrites	-1.1	0.99	79	45.4	[S17]
Hexagonal Zn	-0.95	0.84	85.4	52.5	[S10]
6.8 nm Zn NPs	-1.1	0.99	70	40.3	[S12]
Porous Zn	-0.95	0.84	95	58.4	[S14]
V_O-riched ZnO	-1.1	0.99	83	47.7	[S19]
$Zn_{94}Cu_6$ foam	-0.95	0.84	90	55.3	[S15]
CuIn	-0.6	0.49	85	62.2	[S20]
Cu_2O-derived Cu rods	-0.35	0.24	45	38.2	[S21]
Ni-N-C	-0.78	0.67	85	56.7	[S22]
Mesoporous PdCu	-0.89	0.78	86	54.4	[S23]
3.7 nm Pd NPs	-0.89	0.78	91.2	57.6	[S24]
8 nm Au NPs	-0.67	0.56	90	63.5	[S25]
Au-CeO_X/C	-0.89	0.78	89.1	56.3	[26]
Ultrathin Ag nanowires	-0.956	0.846	99.3	61.3	[S27]
Triangular Ag nanoplates	-0.856	0.746	96.8	61.7	[S28]

Table S3.3 Ohmic resistance (R_s) and charge-transfer resistance (R_{ct}) fitted from the EIS data using the equivalent circuit shown in Figure 4.3d.

Electrodes	**R_s (Ω cm^{-2})**	**R_{ct} (Ω cm^{-2})**
Zn foil	28.4	51.6
S-Zn-NPs	27.8	34.5
H-Zn-NPs	30.2	27.0

Table S3.4 Electronic energies and thermodynamic data at –0.66 V calculated by DFT.

Species_adsorbate	E_{DFT} (eV)	E_{ZPE} (eV)	$-TS$ (eV)	$\int C_p dT$ (eV)	G (eV)	ΔG (eV)
H_2O	-14.220	0.585	-0.673	0.104	-14.204	
CO	-14.779	0.136	-0.596	0.090	-15.149	
CO_2	-22.960	0.309	-0.663	0.098	-23.216	
H_2	-6.767	0.290	-0.403	0.090	-6.790	
H^++e-	-2.723	0.145	-0.202	0.045	-2.735	
002_	-67.180	0.000	0.000	0.000	-67.180	
002_COOH	-92.844	0.589	-0.362	0.147	-92.470	0.662
002_CO	-82.048	0.165	-0.264	0.120	-82.027	-0.364
002_H	-69.983	0.146	-0.034	0.033	-69.839	0.076
100_	-26.881	0.000	0.000	0.000	-26.881	
100_COOH	-52.913	0.608	-0.246	0.132	-52.419	0.412
100_CO	-41.789	0.168	-0.250	0.117	-41.754	-0.392
100_H	-30.008	0.146	-0.046	0.039	-29.869	-0.254
Edge_	-13.495	0.000	0.000	0.000	-13.495	
Edge_COOH	-40.254	0.612	-0.247	0.131	-39.758	-0.312
Edge_CO	-28.211	0.168	-0.245	0.116	-28.172	-0.195
Edge_H	-16.543	0.146	-0.063	0.049	-16.411	-0.181
Corner_	-13.495	0.000	0.000	0.000	-13.495	
Corner_COOH	-39.858	0.595	-0.337	0.145	-39.455	-0.009
Corner_CO	-28.888	0.168	-0.271	0.117	-28.874	-0.897
Corner_H	-16.879	0.146	-0.064	0.049	-16.748	-0.518

Table S3.5 Binding energies of *COOH, *CO and *H intermediates on the surface sites of Zn(002), Zn(100), edge and corner.

Surface sites	ΔE_{COOH} (eV)	ΔE_{CO} (eV)	ΔE_{H} (eV)
Zn(002)	1.322	0.303	0.736
Zn(100)	1.072	0.276	0.406
Edge	0.348	0.472	0.479
Corner	0.651	-0.230	0.142

3.5.4 Supporting references

[S1] G. Kresse, J. Hafner, Ab initio molecular dynamics for liquid metals. Phys. Rev. B 47 (1993) 558.

[S2] G. Kresse, J. Hafner, Ab initio molecular-dynamics simulation of the liquid-metal–amorphous-semiconductor transition in germanium. Phys. Rev. B 49 (1994) 14251.

[S3] G. Kresse, J. Furthmüller, Efficiency of ab-initio total energy calculations for metals and semiconductors using a plane-wave basis set. Comp. Mater. Sci. 6 (1996) 15-50.

[S4] G. Kresse, J. Furthmüller, Efficient iterative schemes for ab initio total-energy calculations using a plane-wave basis set. Phys. Rev. B 54 (1996) 11169.

[S5] B. Hammer, L.B. Hansen, J.K. Nørskov, Improved adsorption energetics within density-functional theory using revised Perdew-Burke-Ernzerhof functionals. Phys. Rev. B 59 (1999) 7413.

[S6] H.J. Monkhorst, J.D. Pack, Special points for brillouin-zone integrations. Phys. Rev. B 13 (1976) 5188.

[S7] W.J. Durand, A.A. Peterson, F. Studt, et al., Structure effects on the energetics of the electrochemical reduction of CO_2 by copper surfaces. Surf. Sci. 605 (2011) 1354-1359.

[S8] Y. Xu, W.A. Shelton, O_2 reduction by lithium on Au (111) and Pt (111). J. Chem. Phys. 133 (2010) 024703.

[S9] V. Tripković, E. Skúlason, S. Siahrostami, et al., J. The oxygen reduction reaction mechanism on Pt (111) from density functional theory calculations. Electrochim. Acta 55 (2010) 7975-7981.

[S10] W.D. Hye, S. Hyeyoung, K. Jaekang, et al., Highly efficient, selective, and stable CO_2 electroreduction on a hexagonal Zn catalyst, Angew. Chem. Int. Ed. 55 (2016) 9297-9300.

[S11] B. Qin, Y. Li, H. Fu, et al., Electrochemical reduction of CO_2 into tunable syngas production by regulating the crystal facets of earth-abundant Zn catalyst, ACS Appl. Mater. Interfaces 10 (2018) 20530-20539.

[S12] H.S. Jeon, I. Sinev, F. Scholten, et al., Operando evolution of the structure and oxidation state of size-controlled Zn nanoparticles during CO_2 electroreduction, J. Am. Chem. Soc. 140 (2018) 9383-9386.

[S13] W. Luo, J. Zhang, M. Li, et al., Boosting CO production in electrocatalytic CO_2 reduction on highly porous Zn catalysts, ACS Catal. (2019) 3783-3791.

[S14] P. Moreno-García, N. Schlegel, A. Zanetti, et al., Selective electrochemical reduction of CO_2 to CO on Zn-based foams produced by Cu^{2+} and template-assisted electrodeposition, ACS Appl. Mater. Interfaces 10 (2018) 31355-31365.

[S15] F. Quan, D. Zhong, H. Song, et al., A highly efficient zinc catalyst for selective electroreduction of carbon dioxide in aqueous NaCl solution, J. Mater. Chem. A 3 (2015) 16409-16413.

[S16] J. Rosen, G.S. Hutchings, Q. Lu, et al., Electrodeposited Zn dendrites with enhanced CO selectivity for electrocatalytic CO_2 reduction, ACS Catal. 5 (2015) 4586-4591.

[S17] D.L.T. Nguyen, M.S. Jee, D.H. Won, et al., Selective CO_2 reduction on zinc electrocatalyst: the effect of zinc oxidation state induced by pretreatment environment, ACS Sustain. Chem. Eng. 5 (2017) 11377-11386.

[S18] T. Zhang, X. Li, Y. Qiu, et al., Multilayered Zn nanosheets as an electrocatalyst for efficient electrochemical reduction of CO_2, J. Catal. 357 (2018) 154-162.

[S19] G. Zhigang, K. Xiangdong, C. Weiwei, et al., Oxygen vacancies in ZnO nanosheets enhance CO_2 electrochemical reduction to CO, Angew. Chem. Int. Ed. 57 (2018) 6054-6059.

[S20] S. Rasul, D.H. Anjum, A. Jedidi, et al., A highly selective copper–indium bimetallic electrocatalyst for the electrochemical reduction of aqueous CO_2 to CO, Angew. Chem. Int. Ed. 54 (2015) 2146-2150.

[S21] C.W. Li, M.W. Kanan, CO_2 reduction at low overpotential on Cu electrodes resulting from the reduction of thick Cu_2O films, J. Am. Chem. Soc. 134 (2012) 7231-7234.

[S22] W. Ju, A. Bagger, G.-P. Hao, et al., Understanding activity and selectivity of metal-nitrogen-doped carbon catalysts for electrochemical reduction of CO_2, Nat. Commun. 8 (2017) 944.

[S23] Z. Yin, D. Gao, S. Yao, et al., Highly selective palladium-copper bimetallic electrocatalysts for the electrochemical reduction of CO_2 to CO, Nano Energy 27 (2016) 35-43.

[S24] D. Gao, H. Zhou, J. Wang, et al., Size-dependent electrocatalytic reduction of CO_2 over Pd nanoparticles, J. Am. Chem. Soc. 137 (2015) 4288-4291.

[S25] W. Zhu, R. Michalsky, O. Metin, et al., Monodisperse Au nanoparticles for selective electrocatalytic reduction of CO_2 to CO, J. Am. Chem. Soc. 135 (2013) 16833-16836.

[S26] D. Gao, Y. Zhang, Z. Zhou, et al., Enhancing CO_2 electroreduction with the metal-oxide interface, J. Am. Chem. Soc. 139 (2017) 5652-5655.

[S27] S. Liu, X.-Z. Wang, H. Tao, et al., Ultrathin 5-fold twinned sub-25 nm silver nanowires enable highly selective electroreduction of CO_2 to CO, Nano Energy 45 (2018) 456-462.

[S28] S. Liu, H. Tao, L. Zeng, et al., Shape-dependent electrocatalytic reduction of CO_2 to CO on triangular silver nanoplates, J. Am. Chem. Soc. 139 (2017) 2160-2163.

Chapter 4. Rational Design of $CdCO_3$ Nanoparticles Decorated Carbon Nanofibers for Boosting Electrochemical CO_2 Reduction

Abstract: Efficient, robust and inexpensive catalysts are highly desirable to drive the electrochemical CO_2 reduction reaction (CO_2RR) to value-added fuels. Herein, low-cost $CdCO_3$ nanoparticles (NPs) decorated carbon nanofibers ($CdCO_3$-CNFs) were synthesized by a facile one-pot method to boost the performance of CO_2RR to CO. The obtained $CdCO_3$-CNFs show a high Faradaic efficiency (93.4%) and a good partial current density (~10 mA cm^{-2}) at a potential of –0.83 V. Moreover, $CdCO_3$-CNFs achieve high CO production rates at moderately negative potentials and a good stability of 24 h with negligible degradation. The superior performance is attributed to the increased number of catalytically active sites, and the strong interaction between $CdCO_3$ NPs and CNFs which promotes electron transfer and secures active sites. This study provides a promising strategy for the efficient and durable CO_2RR by designing a carbonate/carbon system with a strong catalyst-support interaction.

4.1 Introduction

The extensive consumption of fossil fuels has caused an increasing accumulation of atmospheric CO_2, resulting in the adverse climate changes [1-3]. To mitigate these issues, the capture and storage of CO_2 (CCS) and the conversion and utilization of CO_2 have gained widespread attentions [4,5]. However, CCS process is limited by its high costs and safety risks [6]. The conversion of CO_2 into value-added carbon-neutral fuels is a promising strategy towards the sustainable carbon cycle. Typical approaches for CO_2 conversion include (bio)chemical, thermochemical, photochemical and electrochemical catalysis [4, 6, 7]. Among them, electrochemical CO_2 reduction reaction (CO_2RR) is considered as an appealing technology when integrated with renewable electricity [8-10]. Additionally, it can be conducted under mild conditions in aqueous solution, in which water instead of H_2 gas is employed as a hydrogen source [6]. However, the sluggish kinetics for initial CO_2 activation and the inevitable competitive hydrogen evolution reaction (HER) in aqueous electrolytes are the big challenges that hinder the practical applications of CO_2RR [9,11]. To date, nanostructured noble metals, such as Au [12-14], Ag [15,16] and Pd [17,18], are the most active catalysts for CO_2RR, but their scarcity and high costs remarkably limit their large-scale applications. Thus, designing inexpensive electrocatalysts with high catalytic activity and high selectivity for target products is imperative to advance the development of CO_2RR technology.

To that end, various transition metals (e.g., Cu [19-21], Sn [22, 23], and Zn [24-26]), along with some compounds (e.g., Cu_2O [27], CdS [28], and MoP [29]), have been demonstrated to be electrochemically active towards CO_2RR. However, the present catalytic performances on these catalysts are still unsatisfactory due to their high overpotentials, low current densities (j), and insufficient Faradaic efficiencies (FE). Moreover, metal oxides, such as SnO_2 [30], CuO [31] and In_2O_3 [32], generally undergo self-reduction under electrochemical CO_2RR conditions, leading to the dominance of HER and thereby, decreasing the selectivity of desired products. Recently, basic lead carbonate has been proven to be a highly stable and selective catalyst for CO_2RR while suppressing self-reduction [33]. This opens a new avenue for achieving efficient CO_2RR, i.e., carbonates or basic carbonates can be developed as the catalysts that would not be self-reduced under electrochemical CO_2RR conditions. Although the carbonates and basic carbonates (e.g., $CdCO_3$ and $Co_2(OH)_2CO_3$) have shown excellent activity in oxygen reduction reaction and photocatalysis [34-37], they have rarely been studied for the electrochemical CO_2RR.

In addition to highly efficient catalysts, appropriate supporting carbon materials are also of crucial importance for CO_2RR. Strong interaction between catalysts and carbon supports is effective in improving the catalytic properties by regulating the electronic structure, accelerating electron transfer, stabilizing active sites, and adjusting adsorption properties with various reaction intermediates [38,39]. For instance, compared with carbon black (CB) support, carbon nitride supported Au nanoparticles exhibit enhanced electron donation, which favors the CO_2RR to CO process through stabilizing the key intermediate *COOH [40]. Through the rational design of the catalyst/support structure, the number of active sites and also the intrinsic activity of each site are expected to substantially increase, thus simultaneously achieving considerable partial current density and FE of target products on inexpensive catalysts.

Recently, $CdCO_3$ was first explored as a catalyst for CO_2RR by Jiang et al. [41]. The results indicate that $CdCO_3$ is highly selective (FE of 90%) for CO production at less negative potentials. However, the reported current density (j) is only around ~1 mA cm^{-2} at –0.75 V, which is far from being satisfactory. A strong catalyst-support interaction may provide opportunities to significantly increase the j on $CdCO_3$ while maintaining the high selectivity. Therefore, $CdCO_3$ nanoparticles (NPs) decorated carbon nanofibers ($CdCO_3$-CNFs) were prepared by a facile one-pot method and examined as an electrocatalyst for CO_2RR. The $CdCO_3$-CNFs display high FE (maximum value of 93.4%) and partial current density (j_{CO}), as well as outstanding stability towards CO production. The enhanced CO_2RR performance benefits from the increased surface area and the promoted electron transfer induced by the strong interaction between $CdCO_3$ NPs and CNFs.

4.2 Results and discussion

4.2.1 Theoretical considerations of $CdCO_3$ as a CO_2RR catalyst

The feasibility of $CdCO_3$ as a catalyst for CO_2RR to CO was firstly examined by DFT calculations, considering the relatively simple two-electron transfer pathway of CO production [9]. To be electrochemically reduced to CO, CO_2 is initially adsorbed onto the surface of catalysts and forms *COOH intermediate through a proton-coupled electron transfer process [13, 42]. The adsorbed *COOH will be further reduced to *CO by one electron, and finally desorbed from the catalysts. Therefore, the adsorption strength of catalysts and the key intermediates, i.e., *COOH and *CO, directly affects the selectivity for CO formation. Hence, based on the XRD pattern of $CdCO_3$ [43], the binding energies of *COOH and *CO (ΔE_{COOH} and ΔE_{CO}) on the main facets $CdCO_3$(012) and $CdCO_3$(104) were determined (Table S4.1 and S4.2, see Section 4.5 for the supporting tables and figures) by DFT calculations [44-46]. Figure 4.1a and 4.1b illustrate the atomistic structures optimized for *COOH and *CO adsorbed on these two facets. Clearly, both *COOH and *CO intermediates are adsorbed on $CdCO_3$(012) and $CdCO_3$(104) facets through the binding of C and Cd atoms. The results of the calculated binding energies are shown in Figure 4.1c. For comparison, the binding energy data for (211) step facets on transition metals were also included in Figure 4.1c [47]. As the benchmark catalysts to selectively convert CO_2 to CO, Au and Ag have comparably strong bindings with *COOH but have weak adsorption with *CO, which facilitates both the CO_2 activation (*COOH formation) and the *CO desorption steps. In this study, the calculated ΔE_{COOH} and ΔE_{CO} on $CdCO_3$(012) and $CdCO_3$(104) are relatively close to those on Au and Ag. Especially, $CdCO_3(012)$ exhibits the lower ΔE_{COOH} (0.309 eV) and the higher ΔE_{CO} (–0.025 eV) than those of Au and Ag, suggesting the superior adsorption property of $CdCO_3$ for CO production.

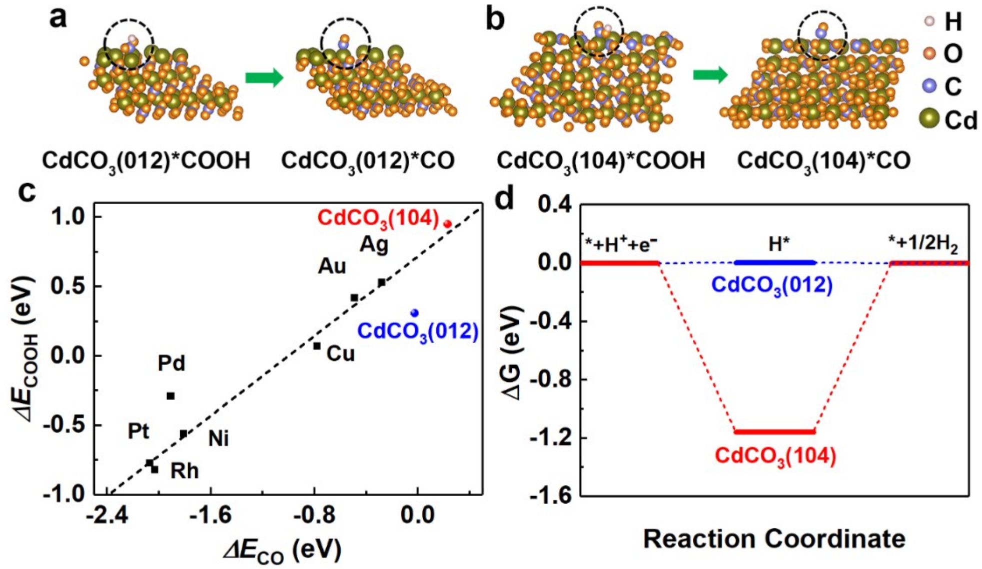

Figure 4.1 Atomistic structures optimized for *COOH and *CO adsorbed on (a) $CdCO_3(012)$ and (b) $CdCO_3(104)$ facets. (c) Correlation of binding energies for *COOH and *CO on various catalysts. The data (black squares) for (211) step facets on transition metals are retrieved from reference [47]. Copyright (2013) American Chemical Society. (d) Free energy diagram for HER on $CdCO_3(012)$ and $CdCO_3(104)$.

Meanwhile, hydrogen binding was also taken into consideration to evaluate the potential of $CdCO_3$ for CO_2RR, given that HER is a prominent competitive reaction that usually accounts for a considerable part of FE in CO_2RR [48]. The Gibbs free energy (ΔG) diagram for HER on $CdCO_3(012)$ and $CdCO_3(104)$ was constructed and displayed in Figure 4.1d. Interestingly, although $CdCO_3(104)$ exhibits a higher ΔE_{COOH} than $CdCO_3(012)$, which makes it relatively difficult for CO_2 activation, $CdCO_3(104)$ tends to overbind *H with a large uphill energy barrier (1.158 eV) encountered in the desorption step. Therefore, $CdCO_3$(104) can facilitate CO_2RR in view of the significantly suppressed HER. Moreover, the structural stability of $CdCO_3$ under electrochemical CO_2RR conditions was explored by relevant thermodynamic data and Pourbaix diagram (see Figure S4.1 and Section 4.6.2 for details) [49,50]. The results indicate that $CdCO_3$ will not be reduced and remain stable under the CO_2RR conditions. Overall, the theoretical results suggest that $CdCO_3$ holds the promise as a potential alternative to noble metals for selective CO_2RR to CO.

4.2.2 Characterizations of $CdCO_3$-CNFs

Guided by the above theoretical calculations, we constructed a $CdCO_3$-CNFs architecture to further enlarge the surface area and modulate the electronic structures of $CdCO_3$ by a strong catalyst-support interaction, so as to achieve the highly efficient CO_2RR. The $CdCO_3$-CNFs were synthesized by a facile one-pot method at room temperature. According to the SEM results (Figure S4.2), the $CdCO_3$ NPs are well dispersed on the CNFs with a diameter of ~100 nm, whereas an agglomeration is observed on the sample without introducing CNFs (Figure S4.3). The improved dispersion benefits CO_2RR with an increased exposure and accessibility of the active sites. The XRD pattern (Figure S4.4) of $CdCO_3$-CNFs, except for a small characteristic peak of CNFs at 25.8°, matches well with the standard pattern of otavite $CdCO_3$ (JCPDS No.42-1342) with trigonal structure, indicating the successful synthesis of $CdCO_3$-CNFs. By comparing the final weights of $CdCO_3$ NPs and $CdCO_3$-CNFs after they were at 900 °C in air in Figure S4.5, the content of CNFs in the composite can be calculated to be 25.8 wt%. This is the optimal content that balances the increased active sites and unfavorable agglomeration of $CdCO_3$ nanoparticles (Figure S4.6 and Table S4.3).

The structural properties of $CdCO_3$-CNFs were further investigated by TEM analysis. The TEM image shown in Figure 4.2a demonstrates the uniform size (average of 11.7 nm, Figure S4.7) of the attached $CdCO_3$ NPs, while the corresponding high-resolution TEM image (Figure 4.2b) displays an interplanar distance of 0.296 nm, which is consistent with the (104) plane of trigonal $CdCO_3$ crystals. This evidence suggests that $CdCO_3$-CNFs are favorable for CO_2RR, since $CdCO_3$(104) facet is proved to suppress HER according to the abovementioned DFT calculations. Moreover, the diffraction rings in the selected-area electron-diffraction (SAED) pattern (Figure 4.2c) reveal the polycrystalline nature of $CdCO_3$ NPs. The EDS elemental line scan (Figure 4.2d) and mapping profiles (Figure 4.2e-i) collectively demonstrate that the $CdCO_3$ NPs are heavily coated on the outer surface of the hollow CNFs.

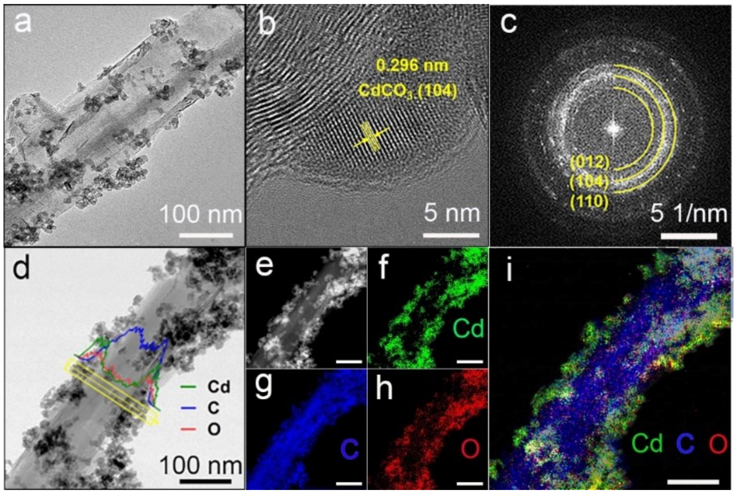

Figure 4.2 (a) Low- and (b) high-resolution TEM images of $CdCO_3$-CNFs. (c) SAED pattern, (d) scanning TEM image with corresponding EDS elemental line scan and (e-i) mapping profiles of $CdCO_3$-CNFs.

4.2.3 Electrocatalytic activity of $CdCO_3$-CNFs for CO_2RR

The electrocatalytic activity of $CdCO_3$-CNFs was then evaluated using pure CNFs, $CdCO_3$ NPs, and bulk $CdCO_3$ powder (Figure S4.3a) as the reference catalysts. 0.5 M $KHCO_3$ (instead of 0.1 M $KHCO_3$) solution was employed as the electrolyte to promote the reaction kinetics over the catalysts (Figure S4.8) [51]. To persuasively clarify the effect of the catalyst-support interaction on the CO_2RR performance, $CdCO_3$-CB (Figure S4.9) was prepared by a similar method and also evaluated for CO_2RR. The linear sweep voltammetry (LSV) curves of all the catalysts were recorded at a scan rate of 10 mV s^{-1}. As shown in Figure 4.3a, $CdCO_3$-CNFs exhibit the highest j among the five samples, and achieve a remarkably high j of –57.8 mA cm^{-2} (normalized by geometric area) at the potential of –1.23 V, suggesting the enhanced catalytic activity of $CdCO_3$-CNFs. Remarkably, the j reaches ~13.6 mA cm^{-2} on $CdCO_3$-CNFs at –1.0 V, which is roughly 3.2 times of the value on the recently reported $CdCO_3$ [41], confirming that a strong catalyst-support interaction is effective in boosting the catalytic activity of $CdCO_3$.

To further pinpoint the reduction products of $CdCO_3$-CNFs, stepped potentiostatic CO_2 electrolyzes were performed at potentials ranging from −0.23 to −1.23 V to periodically quantify the gaseous and liquid products by GC and IC, respectively. The results show that CO and H_2 are the major products over the entire potential range, and a small amount of HCOOH was detected at highly negative potentials (Figure 4.3b). The net total FE of all reduction products is 99.8 ± 1.6%. Clearly, $CdCO_3$-CNFs are highly selective towards CO production with FE over 90% in a broad potential range from −0.73 to −0.93 V, where a maximum FE of 93.4% was obtained at −0.83 V, which is remarkably higher than the values (Figure 4.3c) from $CdCO_3$-CB (84.2% at −0.83 V) and $CdCO_3$ NPs (73.8% at −0.73 V).

Moreover, $CdCO_3$-CNFs started to generate CO (FE of 7.5%) at an onset potential of −0.23 V, which is considerably less negative than the values from most of the other reported non-noble metal-based catalysts [25, 28, 45, 52], whereas CO was not detectable under this potential for $CdCO_3$-CB, $CdCO_3$ NPs and bulk $CdCO_3$. It is noteworthy that the bulk $CdCO_3$ also shows moderate CO selectivity and achieves a maximum FE of 56.8% at −0.83 V, which further validates the abovementioned theoretical results that $CdCO_3$ is a potential candidate for CO production. Figure 4.3d shows the j_{CO}s of all the catalysts calculated based on steady-state j and CO FEs at various potentials. It clearly demonstrates the exclusively high catalytic activity of $CdCO_3$-CNFs towards CO production with a j_{CO} of –37.8 mA cm^{-2} on $CdCO_3$-CNFs at −1.23 V, which is 1.8- and 3.2-fold higher than those on $CdCO_3$-CB and $CdCO_3$ NPs, respectively. This confirms the advantages of the well-designed $CdCO_3$-CNFs architecture.

To further reveal the superior CO_2RR performance over $CdCO_3$-CNFs, the j_{CO} and FE of CO for $CdCO_3$-CNFs were compared with other state-of-the-art catalysts [14, 15, 17, 24, 25, 28, 53-58] (Figure 4.4a and Table S4.4). As can be seen, high FEs and one of the highest j_{CO} values are simultaneously achieved on $CdCO_3$-CNFs at moderately negative potentials. This evidence contributes to the remarkably high CO production rate (PR) on $CdCO_3$-CNFs, as shown in Figure 4.4b. Moreover, a CO PR of 705 μmol h^{-1} cm^{-2} was obtained on $CdCO_3$-CNFs at −1.23 V, outperforming most of the benchmark systems towards CO formation [45]. Additionally, the potential to achieve a CO PR of ~100 μmol h^{-1} cm^{-2} shifts positively by 0.10 and 0.23 V over $CdCO_3$-CNFs as compared to $CdCO_3$-CB and $CdCO_3$ NPs, respectively. Likewise, $CdCO_3$-CNFs exhibit the lowest potential (−0.56 V) to obtain a j_{CO} of 1.0 mA cm^{-}

^{2} among the three catalysts (Figure 4.4c), indicating the promoted kinetics for CO_2RR over $CdCO_3$-CNFs.

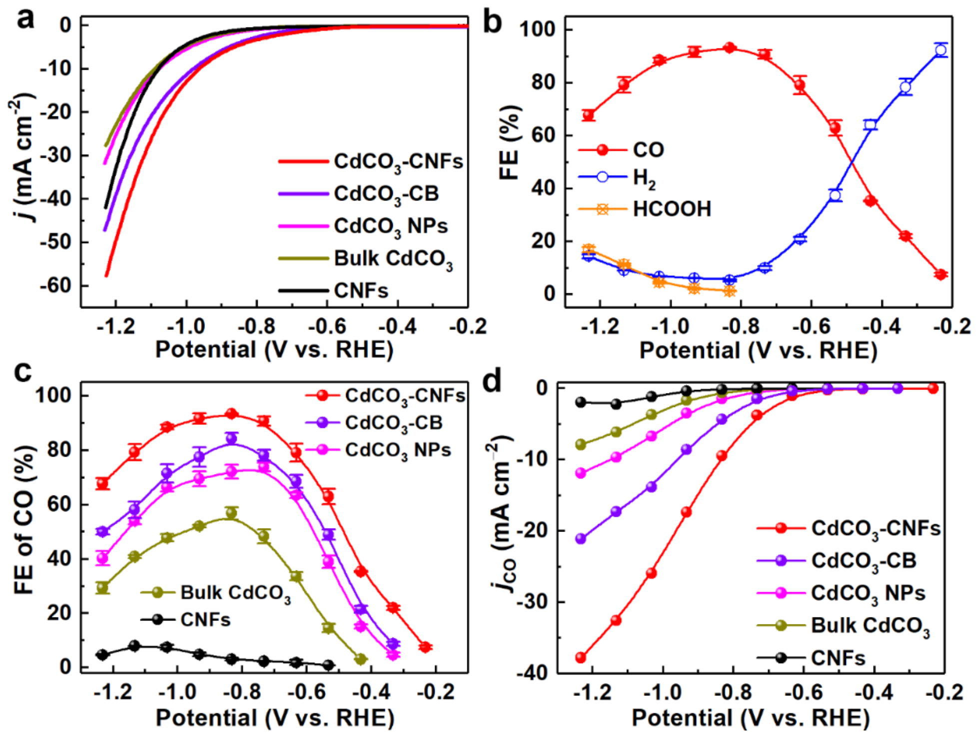

Figure 4.3 (a) LSV curves in CO_2-saturated 0.5 M $KHCO_3$ electrolyte. (b) FEs of all reduction products over $CdCO_3$-CNFs. (c) FEs of CO and (d) j_{CO}s of $CdCO_3$-CNFs, $CdCO_3$-CB, $CdCO_3$ NPs, bulk $CdCO_3$, and CNFs.

Furthermore, the stability of $CdCO_3$-CNFs is another crucial criterion to evaluate a catalyst for CO_2RR and was examined by performing electrolysis at a fixed potential of –0.83 V over an extended period of 24 h. As shown in Figure 4.4d, the recorded j of $CdCO_3$-CNFs exhibits negligible degradation and stabilizes at –9.6 mA cm^{-2} together with FE of CO remaining over 90%, whereas the j of $CdCO_3$-CB experiences visible variation during the stability test (Figure S4.10). This evidence suggests that the $CdCO_3$ NPs are well stabilized by the CNFs, which is further confirmed by SEM, TEM and the corresponding EDS elemental mapping results. As shown in Figure S4.11, the morphology and distribution of $CdCO_3$ NPs were well-preserved after the stability test. Moreover, XRD and XPS analyses reveal that only negligible changes can be observed on the crystal structure and the surface chemical state of $CdCO_3$ NPs after the test (Figure S4.12). This evidence indicates that the structure of $CdCO_3$ is stable under such electrochemical CO_2RR conditions, which is consistent with the results reported by Jiang et al. who conducted CO_2 electrolysis on $CdCO_3$ at –0.75 V for 8 h [41]. Therefore, the $CdCO_3$-CNFs are a promising CO_2RR catalyst with excellent catalytic activity, CO selectivity and good long-term stability.

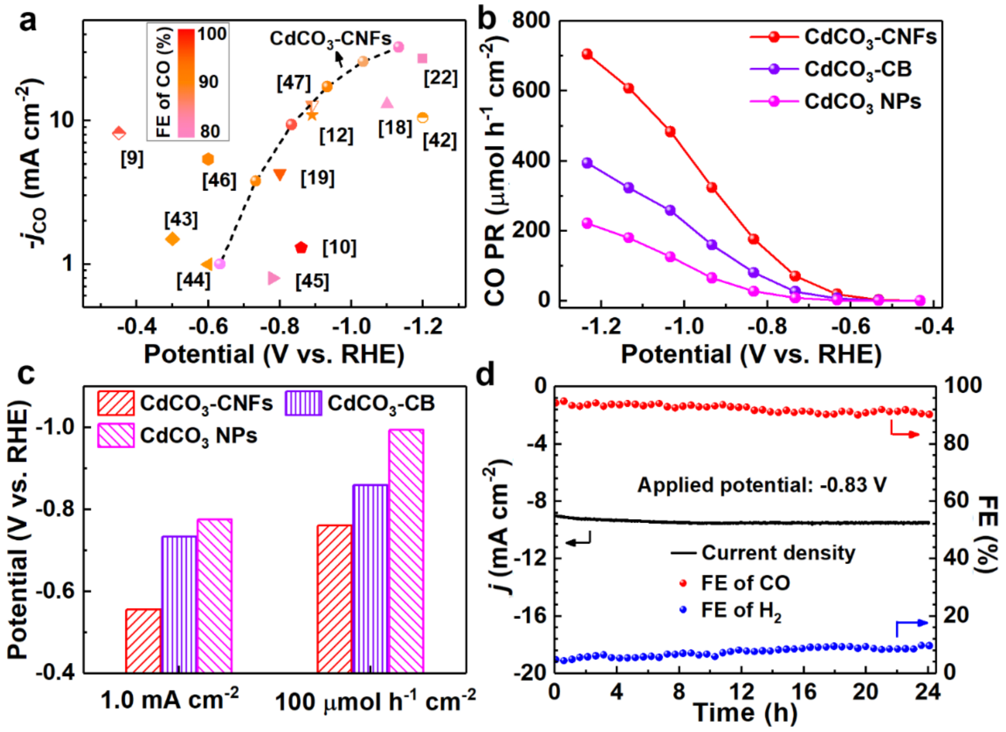

Figure 4.4 (a) Comparison of potential-dependent j_{CO}s and FEs of CO measured in aqueous electrolytes over $CdCO_3$-CNFs (solid circles) and other state-of-the-art catalysts for CO formation, including Au nanowires [14], Ag nanoplates [15], 3.7 nm Pd NPs [17], Zn dendrites [24], S-Zn-S nanosheets [25], CdS nanorods [28], CdS-CNTs [53], Cu-In [54], Cu-Sn [55], N-CNTs [56], Fe-N-C [57], and Au-CeO_2/C [58]. (b) CO PRs of $CdCO_3$-CNFs,

$CdCO_3$-CB, and $CdCO_3$ NPs at various potentials. (c) Potentials at j_{CO} of 1.0 mA cm^{-2} and potentials at CO PR of ~100 μmol h^{-1} cm^{-2} over various catalysts. (d) Stability test for $CdCO_3$-CNFs.

4.3.4 Origins of the superior CO_2RR performance over $CdCO_3$-CNFs

The significantly enhanced catalytic activity of $CdCO_3$-CNFs may partially originate from the increase in electrochemically active surface area (ECSA) since larger ECSA could provide more catalytically active sites [29]. Therefore, the ECSAs for $CdCO_3$-CNFs, $CdCO_3$-CB, and $CdCO_3$ NPs were determined by measuring double-layer capacitance (C_{dl}, see Section 2.5 and Figure S4.13 for details), and the results are shown in Figure 4.5a. As expected, the $CdCO_3$-CNFs achieve the largest ECSA among these catalysts, with the C_{dl} value being roughly 1.4 and 2.6 times higher than those of $CdCO_3$-CB and $CdCO_3$ NPs, respectively. It can be inferred that the introduction of CNFs is effective in increasing the number of catalytically active sites, which subsequently contributes to the increased CO_2 adsorption capacity, as verified by the CO_2 adsorption isotherms in Figure 4.5b. Specifically, the amount of adsorbed CO_2 over $CdCO_3$-CNFs at 1 atm is 20.3 cm^3 g^{-1}, about 2-fold and 3.8 cm^3 g^{-1} higher than the values over $CdCO_3$ NPs and $CdCO_3$-CB, respectively, which ensures enough reactants for the CO_2RR. However, the increased ECSA is only one of contributors to the enhanced conversion performance, given that $CdCO_3$-CNFs exhibit a higher specific j_{CO} than the other two counterparts at each potential (Figure S4.14), which implies the presence of intrinsically more active sites on $CdCO_3$-CNFs.

The improved intrinsic activity of $CdCO_3$-CNFs is further confirmed by the decreased Tafel slope as presented in Figure 4.5c. In details, a relatively lower Tafel slope of 122 mV dec^{-1} is obtained on $CdCO_3$-CNFs as compared to those of $CdCO_3$-CB (126 mV dec^{-1}) and $CdCO_3$

NPs (132 mV dec^{-1}). Moreover, this value is close to the theoretical value of 118 mV dec^{-1} [12], implying that the initial one-electron transfer process is the rate-determining step over $CdCO_3$-CNFs. This is in accordance with the DFT calculation results which suggest that the values of ΔE_{COOH} on $CdCO_3$(012) and $CdCO_3$(104) facets are considerably higher than those of ΔE_{CO} (Table S4.2). The lower Tafel slope of $CdCO_3$-CNFs also indicates a promoted kinetics for the first electron transfer step, which is further demonstrated by the results of electrochemical impedance spectroscopy (EIS) measurements. Based on the radius of the Nyquist plots (Figure 4.5d), the charge transfer resistance (R_{ct}) of $CdCO_3$-CNFs is apparently smaller than those of $CdCO_3$-CB and $CdCO_3$ NPs, suggesting a faster electron transfer. Additionally, according to the fitting parameters of constant phase element (CPE) for the catalysts (Table S4.5), $CdCO_3$-CNFs exhibit a higher capacitance (C) as compared to the other two counterparts, indicating an increased number of charge carriers on the surface and thus a higher catalytic activity [59]. The results of Tafel analysis and EIS measurements imply that the reaction kinetics of CO_2RR is dependent on the catalyst-support interaction.

To further uncover the origin of the high intrinsic catalytic activity of $CdCO_3$-CNFs, XPS was performed to probe the surface electronic structures of $CdCO_3$-CNFs and $CdCO_3$-CB. Figure 4.6a shows the high-resolution Cd 3d XPS spectra, the binding energies for $CdCO_3$-CB located at 405.5 and 412.2 eV can be attributed to the $3d_{5/2}$ and $3d_{3/2}$ of Cd^{2+}, respectively [60]. In contrast, an appreciable binding energy shift (~0.6 eV) to lower energy is observed for both Cd $3d_{5/2}$ and $3d_{3/2}$ in $CdCO_3$-CNFs. The significant decrease in binding energy is indicative of the electron shifts from the carbon support to $CdCO_3$ NPs [40], thus suggesting the strong interaction between $CdCO_3$ NPs and CNFs. UPS plots were further explored to investigate such interaction by evaluating the work functions of the catalysts (Figure S4.15).

The results in Figure 4.6b indicate an obviously lower work function of $CdCO_3$-CNFs (3.49 eV) than that of $CdCO_3$-CB (4.15 eV) and therefore, the easier escape of electrons on the surface of $CdCO_3$-CNFs, verifying the strong catalyst-support interaction. Moreover, the low work function gives rise to a fast electron transfer [61], which is consistent with the EIS results and consequently results in an enhanced CO_2RR catalytic activity.

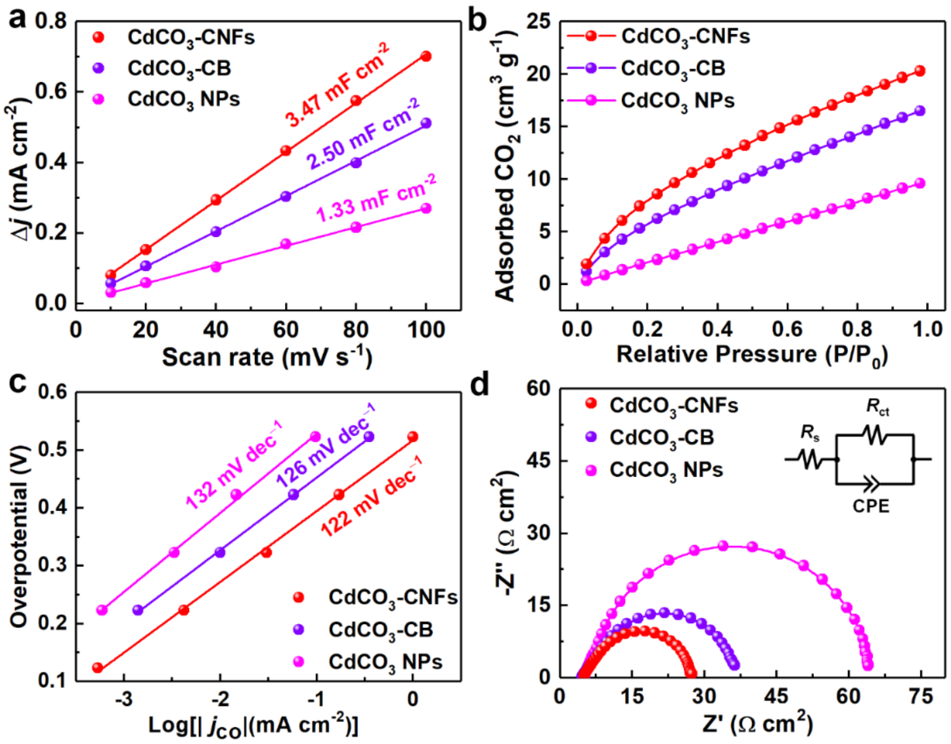

Figure 4.5 (a) Charging current density difference (Δ*j*) plotted against scan rates. (b) CO_2 adsorption isotherms and (c) Tafel plots of $CdCO_3$-CNFs, $CdCO_3$-CB, and $CdCO_3$ NPs. (d) Nyquist plots obtained at −0.83 V. The inset shows the corresponding equivalent circuit.

Collectively, the superior CO_2RR performance over the $CdCO_3$-CNFs primarily originates from the high surface area and the strong interaction between $CdCO_3$ NPs and CNFs. The presence of the strong catalyst-support interaction induces a negatively charged surface of $CdCO_3$, thereby promoting the electron transfer on the catalyst, which is favorable for the enhanced catalytic activity. Moreover, it has been demonstrated that the negatively charged metal components benefit the stabilization of the key *COOH intermediate [38, 40, 62]. From this point of view, the specific electronic structure of $CdCO_3$-CNFs also contributes to their outstanding selectivity for CO_2RR to CO. Furthermore, the strong catalyst-support interaction helps to immobilize the active $CdCO_3$ NPs during CO_2RR, thus improving the catalytic stability of $CdCO_3$-CNFs. The above results indicate that developing a carbonate/carbon system with a strong catalyst-support interaction is an effective strategy for enhancing the activity, selectivity and stability of the electrochemical CO_2RR.

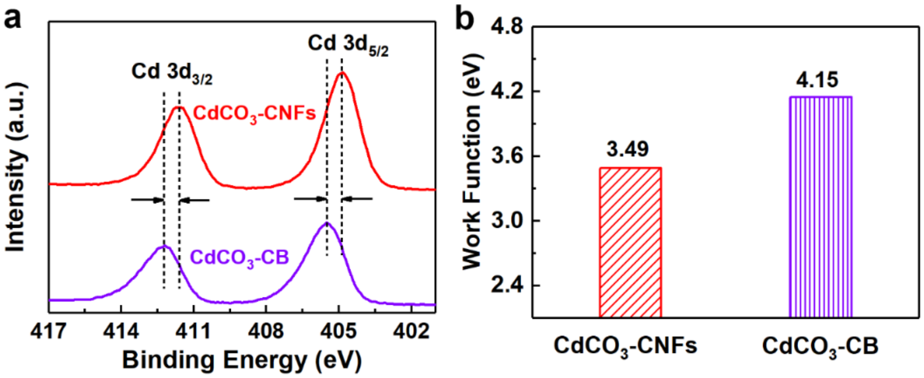

Figure 4.6 (a) Cd 3d XPS spectra and (b) work functions for $CdCO_3$-CNFs and $CdCO_3$-CB

4.3 Conclusions

In summary, as a proof-of-concept experiment, the well-designed $CdCO_3$-CNFs were successfully synthesized for efficient and stable CO_2RR. DFT calculations demonstrate that $CdCO_3$ is selective towards CO production by holding the appropriate binding energies of the key intermediates. $CdCO_3$ NPs were then decorated on hollow CNFs to further boost CO_2RR through the increased surface area and the strong interaction between $CdCO_3$ NPs and CNFs. The presence of such interaction, which is evidenced by XPS and UPS results, enables the fast electron transfer and the stabilization of active sites on $CdCO_3$-CNFs during

CO_2RR. As a result, $CdCO_3$-CNFs are able to achieve high partial current density and selectivity of CO simultaneously at moderately negative potential. The achieved outstanding CO production rate outperforms most of the state-of-the-art catalysts. The superior catalytic activity, along with good stability of over 24 h, endows the $CdCO_3$-CNFs as a promising CO_2RR electrocatalyst to replace noble metals towards CO production. This study exemplifies a rational design for fabricating highly efficient, robust and inexpensive catalysts for the electrochemical CO_2RR via developing a strong catalyst-support interaction.

4.4 References

[1] J. Rogelj, D. Huppmann, V. Krey, et al., A new scenario logic for the Paris Agreement long-term temperature goal, Nature 573 (2019) 357-363.

[2] D.U. Nielsen, X.-M. Hu, K. Daasbjerg, et al., Chemically and electrochemically catalysed conversion of CO_2 to CO with follow-up utilization to value-added chemicals, Nat. Catal. 1 (2018) 244-254.

[3] Y. Zheng, W. Zhang, Y. Li, et al., Energy related CO_2 conversion and utilization: Adv. Mater./nanomaterials, reaction mechanisms and technologies, Nano Energy 40 (2017) 512-539.

[4] A. Modak, P. Bhanja, S. Dutta, et al., Catalytic reduction of CO_2 into fuels and fine chemicals. Green Chem. 22 (2020) 4002-4033.

[5] J.B. Branco, P.E. Brito, A.C. Ferreira, Methanation of CO_2 over nickel-lanthanide bimetallic oxides supported on silica. Chem. Eng. J. 380 (2020) 122465.

[6] R. Zhao, P. Ding, P. Wei, et al., Recent progress in electrocatalytic methanation of CO_2 at ambient conditions. Adv. Funct. Mater. 31 (2021) 2009449.

[7] A. Modak, A. Ghosh, A. Bhaumik, et al., CO_2 hydrogenation over functional nanoporous polymers and metal-organic frameworks. Adv. Colloid Interface Sci. 290 (2021) 102349.

[8] P. Ding, H. Zhao, T. Li, et al., Metal-based electrocatalytic conversion of CO_2 to formic acid/formate. J. Mater. Chem. A 8 (2020) 21947-21960.

[9] J. Qiao, Y. Liu, F. Hong, et al., A review of catalysts for the electroreduction of carbon dioxide to produce low-carbon fuels, Chem. Soc. Rev. 43 (2014) 631-675.

[10] S. Nitopi, E. Bertheussen, S.B. Scott, et al., Progress and perspectives of electrochemical CO_2 reduction on copper in aqueous electrolyte, Chem. Rev. 119 (2019) 7610-7672.

[11] D.D. Zhu, J.L. Liu, S.Z. Qiao, Recent advances in inorganic heterogeneous electrocatalysts for reduction of carbon dioxide, Adv. Mater. 28 (2016) 3423-3452.

[12] Y. Chen, C.W. Li, M.W. Kanan, Aqueous CO_2 reduction at very low overpotential on oxide-derived Au nanoparticles, J. Am. Chem. Soc. 134 (2012) 19969-19972.

[13] W. Zhu, R. Michalsky, O. Metin, et al., Monodisperse Au nanoparticles for selective electrocatalytic reduction of CO_2 to CO, J. Am. Chem. Soc. 135 (2013) 16833-16836.

[14] W. Zhu, Y.-J. Zhang, H. Zhang, et al., Active and selective conversion of CO_2 to CO on ultrathin Au nanowires, J. Am. Chem. Soc. 136 (2014) 16132-16135.

[15] S. Liu, H. Tao, L. Zeng, et al., Shape-dependent electrocatalytic reduction of CO_2 to CO on triangular silver nanoplates, J. Am. Chem. Soc. 139 (2017) 2160-2163.

[16] Q. Lu, J. Rosen, Y. Zhou, et al., A selective and efficient electrocatalyst for carbon dioxide reduction, Nat. Commun. 5 (2014) 3242.

[17] D. Gao, H. Zhou, J. Wang, et al., Size-dependent electrocatalytic reduction of CO_2 over Pd nanoparticles, J. Am. Chem. Soc. 137 (2015) 4288-4291.

[18] D. Gao, H. Zhou, F. Cai, et al., Pd-containing nanostructures for electrochemical CO_2 reduction reaction, ACS Catal. 8 (2018) 1510-1519.

[19] R. Reske, H. Mistry, F. Behafarid, et al., Particle size effects in the catalytic electroreduction of CO_2 on Cu nanoparticles, J. Am. Chem. Soc. 136 (2014) 6978-6986.

[20] Y. Li, F. Cui, M.B. Ross, et al., Structure-sensitive CO_2 electroreduction to hydrocarbons on ultrathin 5-fold twinned copper nanowires, Nano Lett.. 17 (2017) 1312-1317.

[21] S. Mou, Y. Li, L. Yue, et al., Cu_2Sb decorated Cu nanowire arrays for selective electrocatalytic CO_2 to CO conversion. Nano Res. 14 (2021) 2831-2836.

[22] S. Zhang, P. Kang, T.J. Meyer, Nanostructured tin catalysts for selective electrochemical reduction of carbon dioxide to formate, J. Am. Chem. Soc. 136 (2014) 1734-1737.

[23] F. Lei, W. Liu, Y. Sun, et al., Metallic tin quantum sheets confined in graphene toward high-efficiency carbon dioxide electroreduction, Nat. Commun. 7 (2016) 12697.

[24] J. Rosen, G.S. Hutchings, Q. Lu, et al., Electrodeposited Zn dendrites with enhanced CO selectivity for electrocatalytic CO_2 reduction, ACS Catal. 5 (2015) 4586-4591.

[25] C. Li, G. Shen, R. Zhang, et al., Zn nanosheets coated with a ZnS subnanometer layer for effective and durable CO_2 reduction, J. Mater. Chem. A 7 (2019) 1418-1423.

[26] J. Xiao, M.-R. Gao, S. Liu, et al., Hexagonal Zn nanoplates enclosed by Zn (100) and Zn (002) facets for highly selective CO_2 electroreduction to CO, ACS Appl. Mater. Interfaces12 (2020) 31431-31438.

[27] H. Jung, S.Y. Lee, C.W. Lee, et al., Electrochemical fragmentation of Cu_2O nanoparticles enhancing selective C–C coupling from CO_2 reduction reaction, J. Am. Chem. Soc. 141 (2019) 4624-4633.

[28] R. He, A. Zhang, Y. Ding, et al., Achieving the widest range of syngas proportions at high current density over cadmium sulfoselenide nanorods in CO_2 electroreduction, Adv. Mater. 30 (2018) 1705872.

[29] X. Sun, L. Lu, Q. Zhu, et al., MoP nanoparticles supported on indium-doped porous carbon: outstanding catalysts for highly efficient CO_2 electroreduction, Angew. Chem. Int. Ed. 57 (2018) 2427-2431.

[30] A. Dutta, A. Kuzume, V. Kaliginedi, et al., Probing the chemical state of tin oxide NP catalysts during CO_2 electroreduction: A complementary operando approach, Nano Energy 53 (2018) 828-840.

[31] D. Raciti, K.J. Livi, C. Wang, Highly dense Cu nanowires for low-overpotential CO_2 reduction, Nano Lett.. 15 (2015) 6829-6835.

[32] Y. Liang, W. Zhou, Y. Shi, et al., Unveiling in situ evolved In/In_2O_{3-x} heterostructure as the active phase of In_2O_3 toward efficient electroreduction of CO_2 to formate, Sci. Bull. 65 (2020) 1547-1554.

[33] Y. Shi, Y. Ji, J. Long, et al., Unveiling hydrocerussite as an electrochemically stable active phase for efficient carbon dioxide electroreduction to formate, Nat. commun. 11 (2020) 3415.

[34] Y. Wang, W. Ding, S. Chen, et al., Cobalt carbonate hydroxide/C: an efficient dual electrocatalyst for oxygen reduction/evolution reactions. Chem. Commun. 50 (2014) 15529-15532.

[35] D. Vidyasagar, S.G. Ghugal, A. Kulkarni, et al., Microwave assisted in situ decoration of a g-C_3N_4 surface with $CdCO_3$ nanoparticles for visible light driven photocatalysis, New J. Chem. 42 (2018) 6322-6331.

[36] C. Xin, M. Hu, K. Wang, et al., Significant enhancement of photocatalytic reduction of CO_2 with H_2O over ZnO by the formation of basic zinc carbonate, Langmuir 33 (2017) 6667-6676.

[37] T. Tang, W.-J. Jiang, S. Niu, et al., Electronic and morphological dual modulation of cobalt carbonate hydroxides by Mn doping toward highly efficient and stable bifunctional electrocatalysts for overall water splitting, J. Am. Chem. Soc. 139 (2017) 8320-8328.

[38] L.-P. Yuan, W.-J. Jiang, X.-L. Liu, et al., Molecularly engineered strong metal oxide–support interaction enables highly efficient and stable CO_2 electroreduction, ACS Catal. 10 (2020) 13227-13235.

[39] H. Li, C. Chen, D. Yan, et al., Interfacial effects in supported catalysts for electrocatalysis, J. Mater. Chem. A 7 (2019) 23432-23450.

[40] L. Zhang, F. Mao, L.R. Zheng, et al., Tuning metal catalyst with metal–C_3N_4 interaction for efficient CO_2 electroreduction, ACS Catal. 8 (2018) 11035-11041.

[41] X. Jiang, X. Wang, Q. Wang, et al., Efficient activation and electroreduction of carbon dioxide on an electrocatalyst cadmium carbonate. ACS Appli. Energy Mater. 4 (2021) 2073-2080.

[42] F.-Y. Gao, R.-C. Bao, M.-R. Gao, et al., Electrochemical CO_2-to-CO conversion: electrocatalysts, electrolytes, and electrolyzers, J. Mater. Chem. A 8 (2020) 15458-15478.

[43] X. He, Z. Han, F. Kong, et al., Facile synthesis of $CdCO_3$ cubic particles/graphene composite with enhanced electrochemical performance for lithium-ion batteries, Mater. Lett. 236 (2019) 672-675.

[44] G. Kresse, J. Furthmüller, Efficiency of ab-initio total energy calculations for metals and semiconductors using a plane-wave basis set, Comput. Mater. Sci. 6 (1996) 15-50.

[45] W.J. Durand, A.A. Peterson, F. Studt, et al., Structure effects on the energetics of the electrochemical reduction of CO_2 by copper surfaces, Surf. Sci. 605 (2011) 1354-1359.

[46] G. Kresse, J. Hafner, Ab initio molecular-dynamics simulation of the liquid-metal–amorphous-semiconductor transition in germanium. Phys. Rev. B 49 (1994) 14251.

[47] H.A. Hansen, J.B. Varley, A.A. Peterson, et al., Understanding trends in the electrocatalytic activity of metals and enzymes for CO_2 reduction to CO, J. Phys. Chem. Lett. 4 (2013) 388-392.

[48] T. Zheng, K. Jiang, H. Wang, Recent advances in electrochemical CO_2-to-CO conversion on heterogeneous catalysts, Adv. Mater. 30 (2018) 1802066.

[49] H. Gamsjäger, W. Preis, E. Königsberger, et al., Solid-solute phase equilibria in aqueous solution. XI. Aqueous solubility and standard Gibbs energy of cadmium carbonate. J. solution chem. 28 (1999) 711-720.

[50] D.R. Lide, CRC handbook of chemistry and physics, CRC press, 2004.

[51] S. Verma, X. Lu, S. Ma, et al., The effect of electrolyte composition on the electroreduction of CO_2 to CO on Ag based gas diffusion electrodes. Phys. Chem. Chem. Phys. 18 (2016) 7075-7084.

[52] Z.-L. Wang, C. Li, Y. Yamauchi, Nanostructured nonprecious metal catalysts for electrochemical reduction of carbon dioxide, Nano Today 11 (2016) 373-391.

[53] B. Qin, Y. Li, H. Wang, et al., Efficient electrochemical reduction of CO_2 into CO promoted by sulfur vacancies, Nano Energy 60 (2019) 43-51.

[54] S. Rasul, D.H. Anjum, A. Jedidi, et al., A highly selective copper–indium bimetallic electrocatalyst for the electrochemical reduction of aqueous CO_2 to CO, Angew. Chem. Int. Ed. 54 (2015) 2146-2150.

[55] S. Sarfraz, A.T. Garcia-Esparza, A. Jedidi, et al., Cu–Sn bimetallic catalyst for selective aqueous electroreduction of CO_2 to CO, ACS Catal. 6 (2016) 2842-2851.

[56] J. Wu, R.M. Yadav, M. Liu, et al., Achieving highly efficient, selective, and stable CO_2 reduction on nitrogen-doped carbon nanotubes, ACS nano 9 (2015) 5364-5371.

[57] T.N. Huan, N. Ranjbar, G. Rousse, et al., Electrochemical reduction of CO_2 catalyzed by Fe-N-C materials: A structure–selectivity study, ACS Catal. 7 (2017) 1520-1525.

[58] D. Gao, Y. Zhang, Z. Zhou, et al., Enhancing CO_2 electroreduction with the metal-oxide interface, J. Am. Chem. Soc. 139 (2017) 5652-5655.

[59] A.R. Bredar, A.L. Chown, A.R. Burton, et al., Electrochemical impedance spectroscopy of metal oxide electrodes for energy applications. ACS Appl. Energy Mater., 3 (2020) 66-98.

[60] F. Zhang, X. Wang, D. Yin, et al., Efficiency and mechanisms of Cd removal from aqueous solution by biochar derived from water hyacinth (Eichornia crassipes), J. Environ. Manage., 153 (2015) 68-73.

[61] M. Asadi, K. Kim, C. Liu, et al., Nanostructured transition metal dichalcogenide electrocatalysts for CO_2 reduction in ionic liquid, Science, 353 (2016) 467-470.

[62] J. Wang, J. Kim, S. Choi, et al., A review of carbon-supported nonprecious metals as energy-related electrocatalysts, Small Methods, 4 (2020) 2000621.

4.5 Supporting information

4.5.1 Calculations of free energies and binding energies

The Gibbs free energies for relevant species were calculated with the expression [S1]:

$$G=E_{\mathrm{DFT}}+E_{\mathrm{ZPE}}+\int C_{\mathrm{p}}\mathrm{d}T-TS \tag{S4.1}$$

where E_{DFT} is the DFT calculated electronic energy in VASP, E_{ZPE} is the zero-point vibrational energies, T is the temperature (298.15K), $\int C_{\mathrm{p}}\mathrm{d}T$ is the enthalpic correction and TS is the entropy contribution. PV contributions were neglected. 3N freedom degrees were treated as frustrated harmonic vibrations to E_{ZPE} and enthalpy correction, entropy contribution was calculated by proposed standard method and transferred to thermodynamic data at room temperature [S2]. E_{ZPE}, $\int C_{\mathrm{p}}\mathrm{d}T$, and TS are all functions of vibration frequencies of ions. All the relevant thermodynamic data are listed in Table S4.1.

The binding energy of an adsorbate (ΔE_{ad}) was defined by the following equation [S3]:

$$\Delta E_{\mathrm{ad}} = E[\text{ad on CdCO}_3]-(E[\text{CdCO}_3\text{ without ad}]+E_{\mathrm{ref}}[\text{ad}]) \tag{S4.2}$$

where ad is the abbreviation of adsorbate and it could be *COOH, *CO, or *H in this study. E[ad on $CdCO_3$] is the electronic energy with an adsorbate on $CdCO_3$(012) or $CdCO_3$(104) facets. All possible initial adsorption sites in each case were tried and the lowest electronic energy configuration was chosen and recorded as E[ad on $CdCO_3$]. E[$CdCO_3$ without ad] is the electronic energy without any adsorbate on $CdCO_3$ facets. E_{ref}[ad] is the reference electronic energy of the adsorbate. In details,

$$E_{\mathrm{ref}}[\mathrm{COOH}] = E[\mathrm{CO_2}]+\tfrac{1}{2}E[\mathrm{H_2}] \tag{S4.3}$$

$$E_{\mathrm{ref}}[\mathrm{CO}] = E[\mathrm{CO}] \tag{S4.4}$$

$$E_{\mathrm{ref}}[\mathrm{H}] = \tfrac{1}{2}E[\mathrm{H_2}] \tag{S4.5}$$

where E[COOH], E[CO] and $E[H_2]$ are the electronic energies of corresponding molecules (see Table S4.1). The calculated binding energies of *COOH, *CO and *H intermediates on $CdCO_3$(012) or $CdCO_3$(104) facets are listed in Table S4.2.

4.5.2 Structural stability of $CdCO_3$ under CO_2RR conditions

Firstly, the standard electrode potential (E^o) for the reduction of $CdCO_3$ was calculated. The reduction of $CdCO_3$ can be expressed by the following equation:

$$CdCO_3(s)+2e^- \rightarrow Cd(s)+ CO_3^{2-}(aq) \tag{S4.6}$$

Based on the thermodynamic data [S4, S5], the standard Gibbs free energy for this reaction is 147.6 kJ mol^{-1}. Hence, the E^o was determined to be –0.76 V vs. standard hydrogen electrode (SHE), or –0.76 V vs. reversible hydrogen electrode (RHE).

Secondly, the equilibrium electrode potential (E^{eq}) for the reduction of $CdCO_3$ was determined through Pourbaix diagram. Since the experimental condition in this work is quite different from the standard conditions of reaction S4.6, we used an HSC Chemistry 9 software to construct a Pourbaix diagram according to the experimental conditions, so as to determine the E^{eq}. The molality concentration of Cd species was set to 4.85×10^{-5} mol/kg_{H2O}, because ~0.25 mg $CdCO_3$ was used to catalyze CO_2RR in 30 mL of 0.5 M $KHCO_3$ solution. Given that the solubility of CO_2 is 0.033 M in water [S4], the molality concentration of the total dissolved carbon species was fixed at 0.133 mol/kg_{H2O}. The obtained Pourbaix diagram of a Cd-C-H-O system is shown in Figure S4.1. It is worth to note that the local pH (~10 in 0.5 M $KHCO_3$) near the electrode is higher than the value of the bulk electrolyte under electrochemical CO_2RR conditions [S6-8]. Therefore, the E^{eq} for the reduction of $CdCO_3$ was estimated to be –0.70 V vs. SHE (pH = 10).

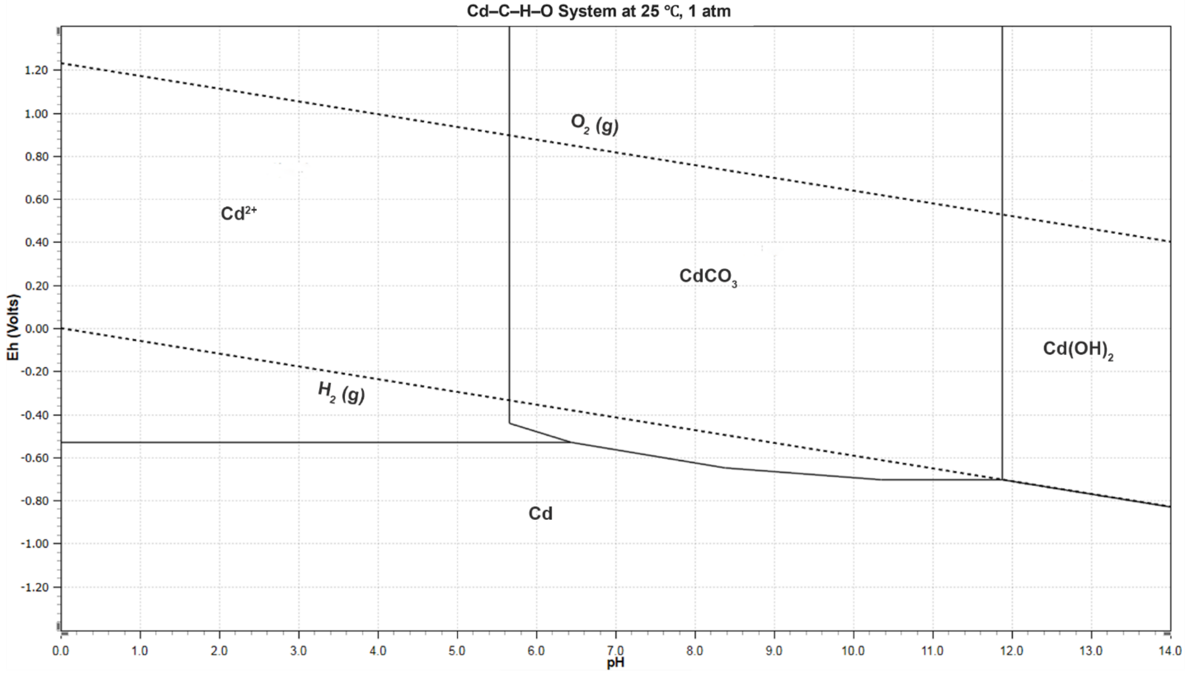

Figure S4.1 Pourbaix diagram for a Cd-C-H-O system. The molality concentration of Cd and carbon species are 4.85×10^{-5} and 0.133 mol/kg$_{H2O}$, respectively, at 25 °C and 1 atm of pressure.

Finally, *iR* drop and activation overpotential (η_{act}) were considered. The stability test for $CdCO_3$-CNFs was performed at –0.83 V and a current density (*j*) of –9.6 mA cm^{-2} was achieved (Figure 4.4d). However, the true potential on the catalyst was more positive than the applied potentials due to the *iR* drop [S9, S10]. The ohmic resistance (R_s) is 6.61 Ω cm^2 at –0.83 V, determined by EIS measurements (Figure 4.5d and Table S4.5). Therefore, the *iR*-corrected potential is calculated to be –0.77 V.

In order to achieve a comparable *j* (~10 mA cm^{-2}) for CO_2RR, the minimum potential change (Min. $\Delta\eta_{act}$) can be calculated by the equation below [S11]:

$$\text{Min. } \Delta\eta_{\text{act}} = \frac{5\text{R}T}{\alpha n\text{F}} \ln 10 \qquad \text{(S4.7)}$$

where n (2) is the number of electrons participating in reaction S4.6; α is the transfer coefficient and assumed to 0.5 in this case; F (96485 C mol^{-1}) is Faraday's constant. The Min. $\Delta\eta_{\text{act}}$ was calculated to be 0.30 V. Therefore, $\eta_{\text{act}} \gg 0.30$ V and hence, the potential required to produce a j of ~10 mA cm^{-2} for reaction S4.6 should be $\ll -1.00$ V ($E - \eta_{\text{act}}$). This value is remarkably more negative than the *iR*-corrected potential (–0.77 V) on the catalyst, suggesting that $CdCO_3$ would not be reduced during the stability test.

4.5.3 Supporting figures and tables

Table S4.1 Electronic energies and relevant thermodynamic data calculated by DFT.

Species_adsorbate	E_{DFT} (eV)	E_{ZPE} (eV)	–TS (eV)	$\int C_p dT$ (eV)	G (eV)
H_2O	–14.220	0.585	–0.673	0.104	–14.204
CO	–14.779	0.136	–0.596	0.090	–15.149
CO_2	–22.960	0.309	–0.663	0.098	–23.216
H_2	–6.767	0.290	–0.403	0.090	–6.790
$CdCO_3$(012)_	–547.752	0.000	0.000	0.000	–547.752
$CdCO_3$(012)_COOH	–574.562	0.615	–0.238	0.131	–574.055
$CdCO_3$(012)_CO	–563.039	0.186	–0.174	0.099	–562.927
$CdCO_3$(012)_H	–551.276	0.145	–0.063	0.049	–551.145
$CdCO_3$(104)_	–905.260	0.000	0.000	0.000	–905.260
$CdCO_3$(104)_COOH	–931.399	0.605	–0.262	0.135	–930.921
$CdCO_3$(104)_CO	–920.179	0.160	–0.289	0.129	–920.179
$CdCO_3$(104)_H	–910.116	0.304	–0.029	0.028	–909.812

Table S4.2 Binding energies of *COOH, *CO and *H intermediates on $CdCO_3$(012) and $CdCO_3$(104) facets.

Active sites	ΔE_{COOH} (eV)	ΔE_{CO} (eV)	ΔE_{H} (eV)
$CdCO_3$(012)	0.309	–0.025	0.002
$CdCO_3$(104)	0.950	0.230	–1.158

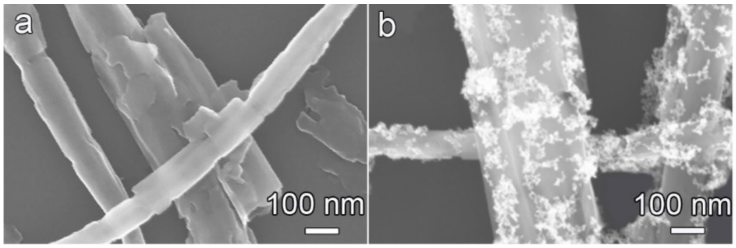

Figure S4.2 SEM images of (a) pretreated CNFs and (b) $CdCO_3$-CNFs

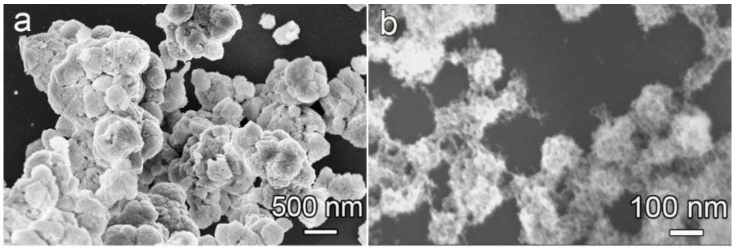

Figure S4.3 SEM images of (a) bulk $CdCO_3$ and (b) $CdCO_3$ NPs.

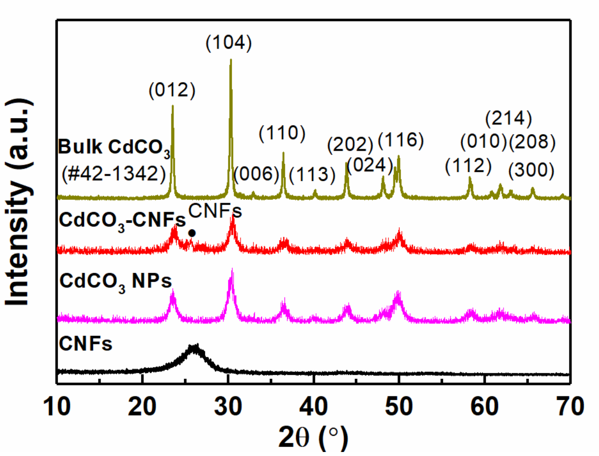

Figure S4.4 XRD patterns of bulk $CdCO_3$, CNFs, $CdCO_3$ NPs and $CdCO_3$-CNFs.

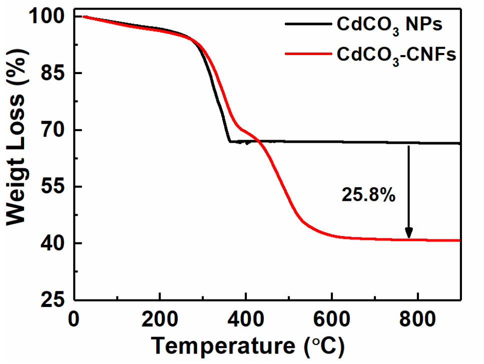

Figure S4.5 Weight loss of CdCO$_3$-CNFs measured by TGA in air.

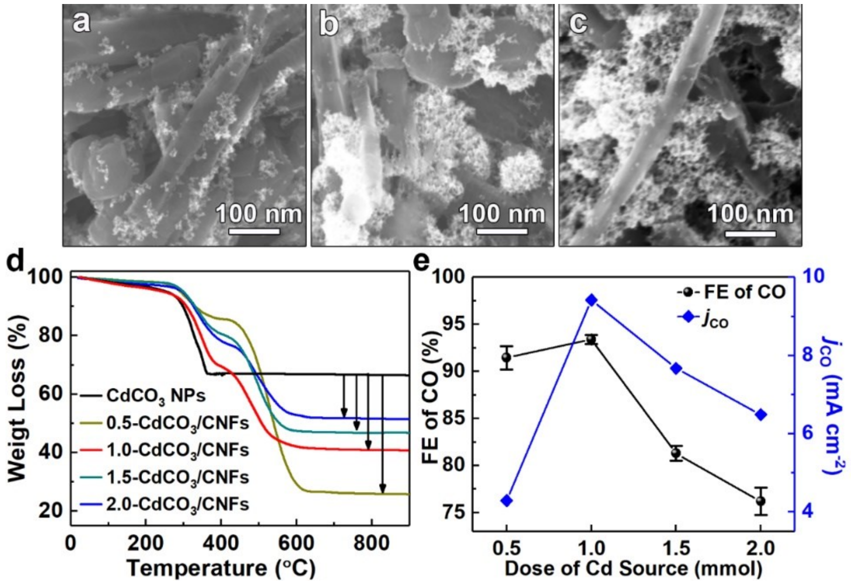

Figure S4.6 SEM images of (a) 0.5-CdCO$_3$/CNFs, (b) 1.5-CdCO$_3$/CNFs and (c) 2.0-CdCO$_3$/CNFs. (d) Weight loss of various CdCO$_3$/CNFs samples measured by TGA in air. (e) FEs of CO and j_{CO}s of various CdCO$_3$-CNFs measured at –0.83 V.

To study the influence of the dose of Cd source on the CO$_2$RR performance over CdCO$_3$/CNFs system, three additional samples were prepared by a same method except for the different amounts of Cd source, and examined their CO$_2$RR performance. The results are shown in Figure S4.6 and Table S4.3. For simplicity, the samples prepared by adding 0.5, 1.0, 1.5 and 2.0 mmol of cadmium acetate dihydrate are denoted as 0.5-$CdCO_3$/CNFs, 1.0-$CdCO_3$/CNFs, 1.5-$CdCO_3$/CNFs and 2.0-$CdCO_3$/CNFs, respectively. Among them, 1.0-$CdCO_3$/CNFs corresponds to $CdCO_3$-CNFs discussed in the text. When decreasing the amount of Cd source to 0.5 mmol, comparable FE of CO is obtained (Figure S4.6e) due to the relatively uniform distribution of $CdCO_3$ nanoparticles as shown in Figure S4.6a. However, the partial current density of CO (j_{CO}) is dramatically declined as compared to 1.0-$CdCO_3$/CNFs, due to the significantly increased content of CNFs (Figure S4.6d) and the corresponding decreased number of catalytically active sites on $CdCO_3$. In contrast, an obvious drop was observed on FE of CO when increasing the amount of Cd source to 1.5 and 2.0 mmol. The deterioration in selectivity is attributed to the agglomeration of $CdCO_3$ nanoparticles as shown in Figure S4.6b and S4.6c, which is unfavorable for CO_2RR. Therefore, it can be concluded that 1.0-$CdCO_3$/CNFs, i.e., $CdCO_3$-CNFs, possess the optimal content of CNFs to achieve efficient and selective CO_2RR by balancing the increased active sites and unfavorable agglomeration of $CdCO_3$ nanoparticles.

Table S4.3 FEs of CO and j_{CO}s of $CdCO_3$/CNFs samples with different contents of CNFs measured at –0.83 V.

Dose of Cd source		Content of CNFs	FE of CO (%)	j_{CO} (mA cm^{-2})
n (mmol)	m (g)			
0.5	0.133	40.5%	91.45	5.38
1.0	0.187	25.8%	93.4	9.42
1.5	0.266	19.3%	86.3	7.67
2.0	0.533	14.7%	84.2	4.29

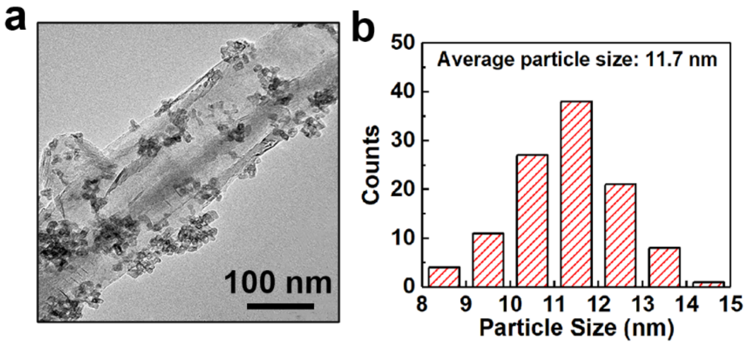

Figure S4.7 (a) TEM image of $CdCO_3$-CNFs and (b) the corresponding particle size distribution

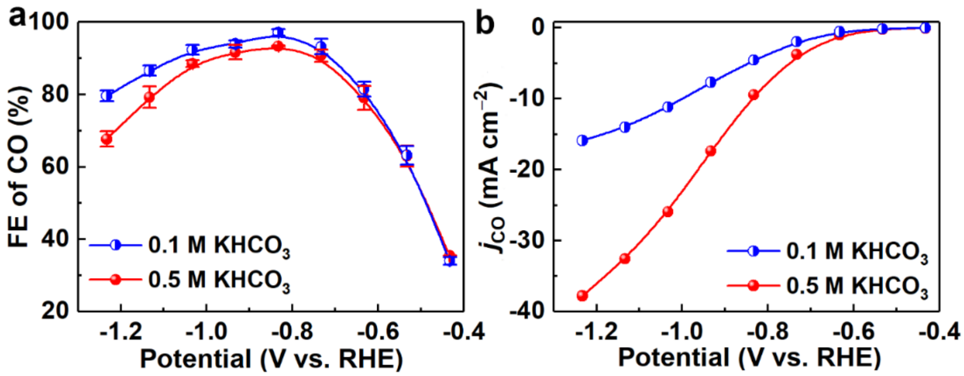

Figure S4.8 (a) FEs of CO and (b) j_{CO}s of $CdCO_3$-CNFs in 0.1 and 0.5 M $KHCO_3$ electrolytes.

The electrochemical CO_2RR performance over $CdCO_3$-CNFs was evaluated in 0.1 M and 0.5 M $KHCO_3$, respectively. As shown in Figure S4.8, a higher FE of CO is achieved in 0.1 M $KHCO_3$ than in 0.5 M $KHCO_3$, especially at highly negative potentials. This can be attributed to the increased local pH at the electrode/electrolyte interface caused by the lower buffer ability of 0.1 M $KHCO_3$ to neutralize the generated OH^- [S6]. The high local pH has been demonstrated to inhibit the competitive hydrogen evolution reaction (HER), thereby increasing the selectivity of CO [S2]. On the contrary, $CdCO_3$-CNFs deliver remarkably lower partial current densities of CO (j_{CO}s) in 0.1 M $KHCO_3$ than the values in 0.5 M $KHCO_3$. It has been proven that an increase in the concentration of electrolytes leads to an improved ionic conductivity [S13] and an increased concentration of dissolved CO_2 near the electrode [S14], thereby significantly promoting the reaction kinetics for CO_2RR. Briefly, an increase in the concentration of bicarbonate boosts the current density at the compromise of CO FE. Since high values of j_{CO} are more desirable for practical applications, the electrochemical CO_2RR performance over the catalysts was mainly evaluated in 0.5 M $KHCO_3$ in this work.

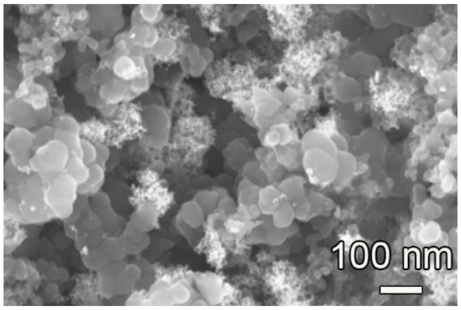

Figure S4.9 SEM image of $CdCO_3$-CB.

Table S4.4 Comparison of CO_2RR performance for CO production over $CdCO_3$-CNFs and other state-of-the-art catalysts in aqueous electrolytes.

Catalysts	**Electrolyte**	***E* (V)**	**j_{co} (mA cm^{-2})**	**FE of CO**
$CdCO_3$-CNFs (This work)	0.5 M $KHCO_3$	–1.13	–32.6	79.3%
		–1.03	–25.9	88.6%
		–0.93	–17.3	91.7%
		–0.83	–9.4	93.4%
		–0.73	–3.8	90.8%
		–0.63	–1.0	79.1%
$CdCO_3$[S15]	0.1 M $KHCO_3$	-0.35	$\sim -4.5\times10^{-5}$*	90%
CdS nanorods[S16]	0.1 M $KHCO_3$	–1.2	–21.9	81%
CdS-CNTs[S17]	0.1 M $KHCO_3$	–1.2	–10.5	92%
Zn dendrites[S18]	0.5 M $NaHCO_3$	–1.1	–13.0	79%
S-Zn-S nanosheets[S19]	0.1 M $KHCO_3$	–0.8	–4.3	94.2%
Cu-In[S20]	0.1 M $KHCO_3$	–0.5	–1.5	90%
Cu-Sn[S21]	0.1 M $KHCO_3$	–0.6	–1.0	~90%
N-CNTs[S22]	0.1 M $KHCO_3$	–0.78	–0.8	80%
Fe-N-C[S23]	0.5 M $NaHCO_3$	–0.6	–5.4	90%
3.7 nm Pd NPs[S24]	0.1 M $KHCO_3$	–0.89	–11.0	91.2%
Ag nanoplates[S25]	0.1 M $KHCO_3$	–0.86	–1.3	96.8%
Au nanowires[S26]	0.5 M $KHCO_3$	–0.35	–8.2	94%
Au-CeO_2/C[S27]	0.1 M $KHCO_3$	–0.89	–12.9	89.1%

*: The j_{CO} of $CdCO_3$ from reference S15 is estimated based on the reported Tafel plots.

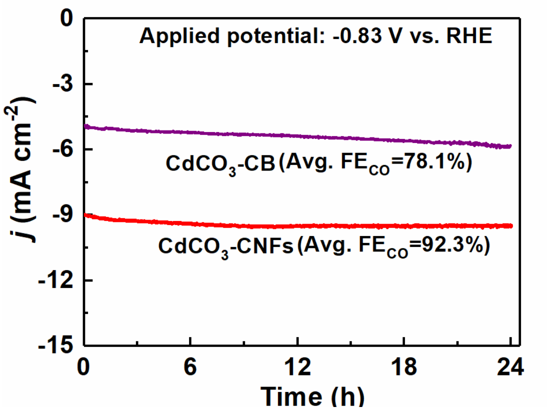

Figure S4.7 Stability tests of CdCO$_3$-CNFs and CdCO$_3$-CB at the potential of –0.83 V. The Avg. FE$_{CO}$ denotes average FE of CO.

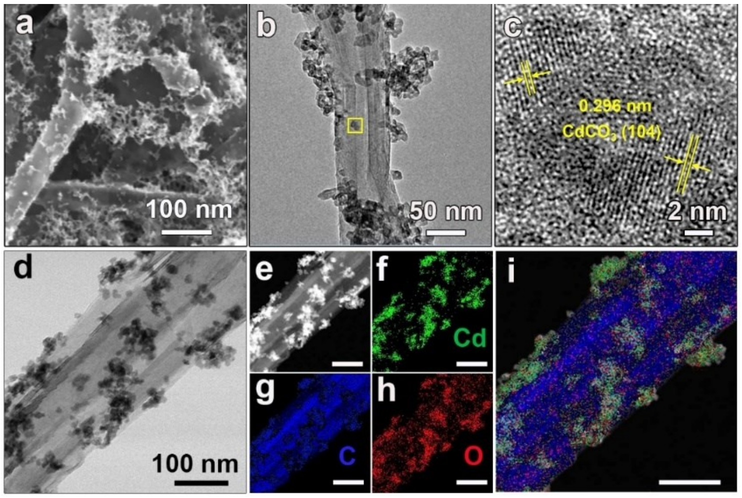

Figure S4.8 (a) SEM image, (b) low- and (c) high-resolution TEM images of CdCO$_3$-CNFs after the stability test. (d) Scanning TEM image and (e-i) corresponding EDS elemental mapping profiles of CdCO$_3$-CNFs after stability test.

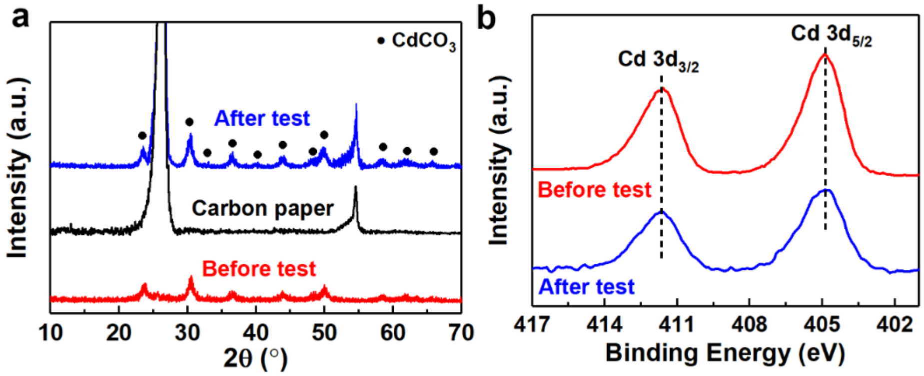

Figure S4.9 (a) XRD patterns of $CdCO_3$-CNFs before and after the stability test, as well as carbon paper. (b) XPS spectra of Cd 3d for $CdCO_3$-CNFs before and after the stability test.

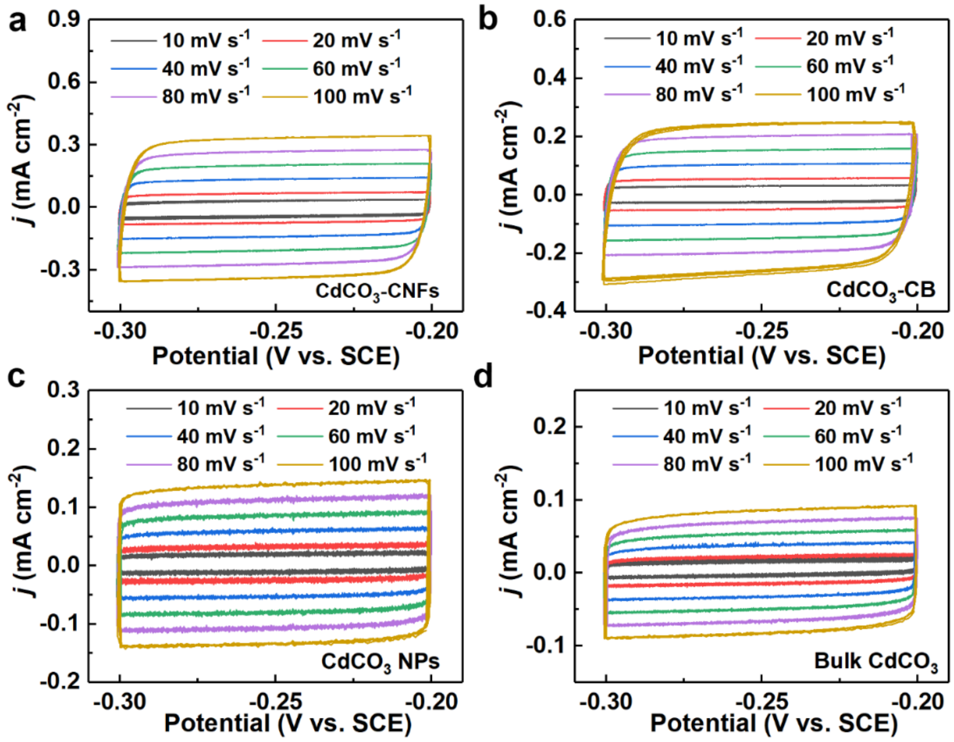

Figure S4.10 CVs of (a) $CdCO_3$-CNFs, (b) $CdCO_3$-CB, (c) $CdCO_3$ NPs and (b) bulk $CdCO_3$ with a potential range from –0.2 to –0.3 V vs. SCE in an CO_2-bubbled 0.5 M $KHCO_3$ solution.

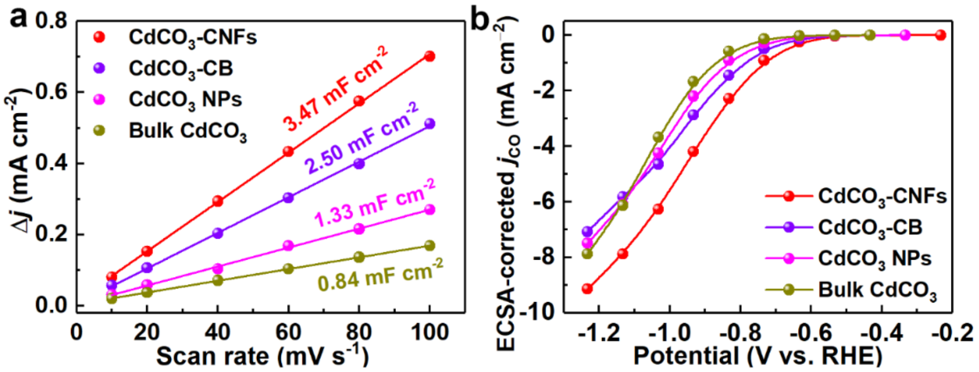

Figure S4.14 (a) Charging current density difference plotted against scan rates and (b) ECSA-corrected j_{CO} of CdCO$_3$-CNFs, CdCO$_3$-CB, CdCO$_3$ NPs and bulk CdCO$_3$.

Table S4.5 Fitting parameters of EIS results for the CdCO$_3$-based catalysts.

Catalysts	R_s (Ω cm^2)	CPE		C (F cm^{-2})	R_{ct} (Ω cm^2)
		Q (Ω^{-1} cm^{-2} s^n)	n		
CdCO$_3$-CNFs	6.61	9.81×10^{-4}	0.93	7.32×10^{-4}	20.83
CdCO$_3$-CB	6.58	9.23×10^{-4}	0.88	5.68×10^{-4}	30.72
CdCO$_3$ NPs	6.67	7.85×10^{-4}	0.91	5.81×10^{-4}	59.76

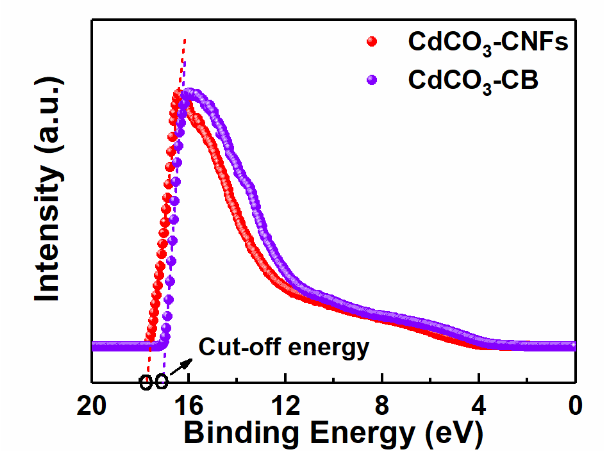

Figure S4.15 UPS plots of CdCO$_3$-CNFs and CdCO$_3$-CB

4.5.4 Supporting references

[S1] Y. Xu and W. A. Shelton, O_2 reduction by lithium on Au (111) and Pt (111), J. Chem. Phys 133 (2010) 024703.

[S2] V. Tripković, E. Skúlason, S. Siahrostami, J. K. Nørskov and J. Rossmeisl, The oxygen reduction reaction mechanism on Pt (111) from density functional theory calculations, Electrochim. Acta 55 (2010) 7975-7981.

[S3] K. Liu, J. Wang, M. Shi, J. Yan and Q. Jiang, Simultaneous achieving of high faradaic efficiency and CO partial current density for CO_2 reduction via robust, noble-metal-free Zn nanosheets with favorable adsorption energy. Adv. Energy Mater. 9 (2019) 1900276.

[S4] D.R. Lide, CRC handbook of chemistry and physics, CRC press, 2004.

[S5] H. Gamsjäger, W. Preis, E. Königsberger, M.C. Magalhães, P. Brandão, Solid-solute phase equilibria in aqueous solution. XI. Aqueous solubility and standard Gibbs energy of cadmium carbonate. J. solution chem. 28 (1999) 711-720.

[S6] N. Gupta, M. Gattrell, B. MacDougall, Calculation for the cathode surface concentrations in the electrochemical reduction of CO_2 in $KHCO_3$ solutions. J. appl. Electrochem. 36 (2006) 161-172.

[S7] C. Chen, B. Zhang, J. Zhong, Z. Cheng, Selective electrochemical CO_2 reduction over highly porous gold films. J. Mater. Chem. A 5 (2017) 21955-21964.

[S8] M. Ma, B.J. Trześniewski, J. Xie, W.A. Smith, Selective and efficient reduction of carbon dioxide to carbon monoxide on oxide - derived nanostructured silver electrocatalysts. Angew. Chem. 128 (2016) 9900-9904.

[S9] S. Liu, J. Xiao, X.F. Lu, J. Wang, X. Wang, X.W. Lou, Efficient electrochemical reduction of CO_2 to HCOOH over Sub-2 nm SnO_2 quantum wires with exposed grain boundaries. Angew. Chem., Int. Ed. 58 (2019) 8499-8503.

[S10] K.P. Kuhl, E.R. Cave, D.N. Abram, T.F. Jaramillo, New insights into the electrochemical reduction of carbon dioxide on metallic copper surfaces. Energy Environ. Sci. 5 (2012) 7050-7059.

[S11] R. O'hayre, S.W. Cha, W. Colella, F.B. Prinz, Fuel cell fundamentals. John Wiley & Sons, 2016.

[S12] W. Luo, J. Zhang, M. Li, A. Züttel, Boosting CO production in electrocatalytic CO_2 reduction on highly porous Zn catalysts. ACS Catal. (2019) 3783-3791.

[S13] S. Verma, X. Lu, S. Ma, R.I. Masel, P.J. Kenis, The effect of electrolyte composition on the electroreduction of CO_2 to CO on Ag based gas diffusion electrodes. Phys. Chem. Chem. Phys. 18 (2016) 7075-7084.

[S14] Y. Hori, Modern Aspects of Electrochemistry 42, Springer, 2008, pp. 89-189.

[S15] X. Jiang, X. Wang, Q. Wang, X. Xiao, J. Chen, M. Wang, Y. Shen, Efficient activation and electroreduction of carbon dioxide on an electrocatalyst cadmium carbonate. ACS Appl. Energy Mater. 4 (2021) 2073-2080.

[S16] R. He, A. Zhang, Y. Ding, T. Kong, Q. Xiao, H. Li, Y. Liu, J. Zeng, Achieving the widest range of syngas proportions at high current density over cadmium sulfoselenide nanorods in CO_2 electroreduction, Adv. Mater. 30 (2018) 1705872.

[S17] B. Qin, Y. Li, H. Wang, G. Yang, Y. Cao, H. Yu, Q. Zhang, H. Liang, F. Peng, Efficient electrochemical reduction of CO_2 into CO promoted by sulfur vacancies, Nano Energy 60 (2019) 43-51.

[S18] J. Rosen, G.S. Hutchings, Q. Lu, R.V. Forest, A. Moore, F. Jiao, Electrodeposited Zn dendrites with enhanced CO selectivity for electrocatalytic CO_2 reduction, ACS Catal. 5 (2015) 4586-4591.

[S19] C. Li, G. Shen, R. Zhang, D. Wu, C. Zou, T. Ling, H. Liu, C. Dong, X.-W. Du, Zn nanosheets coated with a ZnS subnanometer layer for effective and durable CO_2 reduction, J. Mater. Chem. A 7 (2019) 1418-1423.

[S20] S. Rasul, D.H. Anjum, A. Jedidi, Y. Minenkov, L. Cavallo, K. Takanabe, A highly selective copper–indium bimetallic electrocatalyst for the electrochemical reduction of aqueous CO_2 to CO, Angew. Chem. Int. Ed. 54 (2015) 2146-2150.

[S21] S. Sarfraz, A.T. Garcia-Esparza, A. Jedidi, L. Cavallo, K. Takanabe, Cu–Sn bimetallic catalyst for selective aqueous electroreduction of CO_2 to CO, ACS Catal. 6 (2016) 2842-2851.

[S22] J. Wu, R.M. Yadav, M. Liu, P.P. Sharma, C.S. Tiwary, L. Ma, X. Zou, X.-D. Zhou, B.I. Yakobson, J. Lou, Achieving highly efficient, selective, and stable CO_2 reduction on nitrogen-doped carbon nanotubes, ACS nano 9 (2015) 5364-5371.

[S23] T.N. Huan, N. Ranjbar, G. Rousse, M. Sougrati, A. Zitolo, V. Mougel, F. Jaouen, M. Fontecave, Electrochemical reduction of CO_2 catalyzed by Fe-N-C materials: A structure–selectivity study, ACS Catal. 7 (2017) 1520-1525.

[S24] D. Gao, H. Zhou, J. Wang, S. Miao, F. Yang, G. Wang, J. Wang, X. Bao, Size-dependent electrocatalytic reduction of CO_2 over Pd nanoparticles, J. Am. Chem. Soc. 137 (2015) 4288-4291.

[S25] S. Liu, H. Tao, L. Zeng, Q. Liu, Z. Xu, Q. Liu, J.L. Luo, Shape-dependent electrocatalytic reduction of CO_2 to CO on triangular silver nanoplates, J. Am. Chem. Soc. 139 (2017) 2160-2163.

[S26] W. Zhu, Y.-J. Zhang, H. Zhang, H. Lv, Q. Li, R. Michalsky, A.A. Peterson, S. Sun, Active and selective conversion of CO_2 to CO on ultrathin Au nanowires, J. Am. Chem. Soc. 136 (2014) 16132-16135.

[S27] D. Gao, Y. Zhang, Z. Zhou, F. Cai, X. Zhao, W. Huang, Y. Li, J. Zhu, P. Liu, F. Yang, G. Wang, X. Bao, Enhancing CO_2 electroreduction with the metal-oxide interface, J. Am. Chem. Soc. 139 (2017) 5652-5655.

Chapter 5. In-situ Generated Hydroxides Realize Near-unity CO Selectivity for Electrochemical CO_2 Reduction

Abstract: Electrochemical reduction of CO_2 to CO is an attractive approach for the sustainable carbon cycle. However, the activity and selectivity of the CO_2 reduction reaction (CO_2RR) are often limited by the competitive hydrogen evolution reaction (HER) in aqueous media. In this work, in-situ generated hydroxides were introduced by the synthesis of rhombohedral $CdCO_3$ crystals (i-$CdCO_3$) under electrochemical CO_2RR conditions. The generated hydroxides contribute to an increased local pH at the electrode/electrolyte interface, thereby effectively inhibiting HER. As a result, the obtained i-$CdCO_3$ exhibits remarkably higher CO Faradaic efficiency (over 90%) in a broad potential range, where a near 100% selectivity is achieved, as compared to a pre-synthesized $CdCO_3$ with similar morphology. Moreover, i-$CdCO_3$ delivers a large current density of −24.8 mA mg^{-1} at −1.26 V, together with a good stability of 36 h with negligible degradation, further demonstrating its superiority for efficient CO_2RR. This study proposes a promising design strategy to boost the selectivity of CO_2RR systems through in-situ producing hydroxides near the electrode to suppress the unfavorable HER.

5.1 Introduction

Electrochemical CO_2 reduction reaction (CO_2RR), powered by renewable electricity sources, is an attractive approach to closing the anthropogenic CO_2 cycle through the formation of value-added fuels [1-3]. Among the various CO_2RR products, CO is an important feedstock for many industrial processes such as the Fischer-Tropsch synthesis [4], it is also the most kinetically accessible product [5,6]. However, the concurrent hydrogen evolution reaction

(HER) often competes with CO_2RR in aqueous electrolytes, leading to the insufficient selectivity and energy efficiency of CO production [5]. Thus, it is of great importance to develop advanced catalysts with the capacity of efficiently promoting CO_2RR to CO while simultaneously suppressing the competitive HER.

Various materials, including metals [7-9], transition metal chalcogenides [10-11], carbon materials [12,13] and molecular catalysts [14,15], have been identified to be catalytically active for the CO_2RR to CO. Particularly, the well-designed nanostructured noble metals, such as ultrathin Au nanowires [16] and triangular Ag nanoplates [17], are among the most selective catalysts for CO production with the Faradaic efficiency (FE) of over 90%. However, their scarcity and the associated high costs inevitably hinder large-scale applications. Therefore, tremendous efforts have been devoted to seeking earth-abundant alternatives with the catalytic activity and CO selectivity comparable to the noble metals. To this end, several structural and morphological characteristics, including particle size [18,19], grain boundaries [20-22], exposed crystal facets [23,24] and surface defects [25,26], have been experimentally and computationally demonstrated to significantly influence the CO selectivity through tuning the binding energies of key reaction intermediates (*COOH, *CO and *H) for CO_2RR and HER. Besides the structure and morphology of catalysts, the CO_2RR selectivity also depends on the nature of electrolytes [27-29]. An important parameter for electrolytes is the local pH at the electrode/electrolyte interface, which is closely related to the formation of intermediates in certain reaction pathways. However, the effect of local pH on the CO_2RR selectivity has only been reported by limited studies.

The local pH effect was first reported by Hori et al., they found that the high pH near Cu electrode could facilitate the CO_2RR to C_2H_4 [30]. Likewise, a promoted C_2H_4 production was observed on dense Cu nanowire arrays which contribute to an increased local pH through impeding the neutralization of OH^- [31]. Apart from Cu-based catalysts, the local pH also has a crucial influence on the product distribution of Ag- and Au-based catalysts [32-34]. For instance, by substituting K_2HPO_4 (higher buffer capacity) for $KHCO_3$, the FE of CO on polycrystalline Ag is remarkably decreased with enhanced FE of H_2, as a result of the relatively low local pH that favors HER [32]. Although the specific role of local pH in the CO_2RR process has not been thoroughly explored to date, taking advantage of such local pH effect for enhancing CO selectivity is an attractive strategy for designing highly efficient and cost-effective CO_2RR systems.

This study is the first exploration for generating hydroxides (OH^-) near the electrode via the in-situ synthesis of $CdCO_3$ (i-$CdCO_3$) from CdO porous nanosheets (PNSs) under electrochemical CO_2RR conditions, thereby increasing the local pH. Compared with similarly sized $CdCO_3$ (s-$CdCO_3$) which has been pre-synthesized, the obtained i-$CdCO_3$ displays considerably increased FEs of CO in the entire measured potential range and reaches a maximum CO FE of 99.2% at a potential of −0.86 V. The enhancement in CO selectivity is demonstrated to benefit from the higher local pH near the catalyst surface which significantly promotes CO_2RR while inhibiting HER.

5.2 Results and discussion

The CdO PNSs were synthesized through annealing the precursors of $Cd(OH)_2$ nanosheets (NSs) obtained via a facile wet-chemical method. SEM and TEM were first employed to demonstrate the morphology evolution of $Cd(OH)_2$ NSs to CdO PNSs. As shown in Figure 5.1a-c, randomly oriented $Cd(OH)_2$ NSs were transformed to CdO PNSs with massive mesopores. The high-resolution TEM image (Figure 5.1d) displays an interplanar distance of 0.271 nm, which matches well with the (111) plane of the cubic CdO crystal phase [35], indicating the successful synthesis of CdO PNSs. The porous feature of CdO PNSs was further confirmed by N_2 adsorption–desorption isotherm (Figure 5.1e), which implies the presence of numerous pores with a size of 2-5 nm.

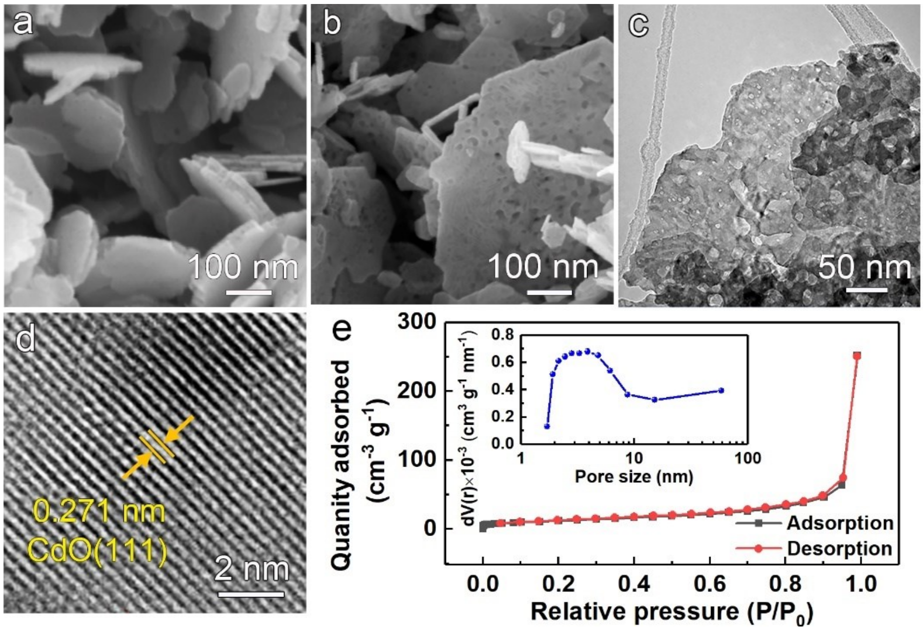

Figure 5.1 SEM images of (a) $Cd(OH)_2$ NSs and (b) CdO PNSs; (c) TEM image of CdO PNSs and (d) the corresponding high-resolution TEM image; (e) N_2 adsorption-desorption isotherm of CdO PNSs, where the inset shows the pore size distribution.

The as-synthesized CdO PNSs were then loaded on carbon paper to fabricate the working electrode. Before electrochemical CO_2RR measurements, the fabricated electrode was pretreated to obtain i-$CdCO_3$ by applying a constant potential of −1.26 V for 90 min in CO_2-bubbled 0.1 M $KHCO_3$ electrolyte till the steady current was obtained (Figure S5.1, see Section 5.5 for the supporting figures and tables). The structure and morphology evolution of CdO PNSs to i-$CdCO_3$ was determined by SEM, XRD and XPS analysis. Apparently, the sheet-like nanostructure of CdO PNSs (Figure 5.2a) collapsed under such in-situ CO_2RR conditions, and rhombohedral $CdCO_3$ crystals appeared and accumulated on the electrode surface (Figure 5.2b). These $CdCO_3$ crystals gradually grew to 200-300 nm (Figures 5.2c and S5.2) under the negative potential and meanwhile, a stable current was reached. EDS elemental mappings (Figure 5.2d-g) show the homogeneous distributions of Cd, C and O in the $CdCO_3$ crystal, which verifies the successful preparation of i-$CdCO_3$. Moreover, the XRD patterns (Figure 5.2h) demonstrate the transformation of cubic CdO (JCPDS 05-0640) to rhombohedral $CdCO_3$ (JCPDS 42-1342). This is further confirmed by XPS results, as the Cd 3d peaks of i-$CdCO_3$ moved to the identical position as pristine commercial $CdCO_3$ (p-$CdCO_3$, Figure S5.3) after the pre-treatment process (Figure 5.2i), and carbonate species was detected according to XPS spectra of C 1s (Figure S5.4). Notably, the rhombohedral shape of i-$CdCO_3$ is characteristic of calcite-group minerals (e.g., Ca, Mg, Fe, Cd and Zn carbonates) [36,37]. It implies that the synthesized i-$CdCO_3$ is composed of isotropic rhombohedral crystals delimited by a set of equivalent oblique $\{10\bar{1}4\}$ facets, and the cadmium and CO_3^{2-} are closely packed along the $\{10\bar{1}4\}$ facets for the maximum thermodynamic stability [38].

The growth of i-$CdCO_3$ can be well understood based on the chemical reaction below:

$$CdO + HCO_3^- \rightarrow CdCO_3 + OH^- \qquad (5.1)$$

Briefly, the CdO reacted with HCO_3^- in the electrolyte to form $CdCO_3$ while releasing OH^-. A similar phenomenon was also observed on the electrode in Ar-bubbled bicarbonate solution (Figure S5.5), further verifying the occurrence of the reaction. The released OH^- leads to a high local pH near the electrode, which is unfavorable for HER. Therefore, it is expected to achieve enhanced CO_2RR on the as-prepared i-$CdCO_3$.

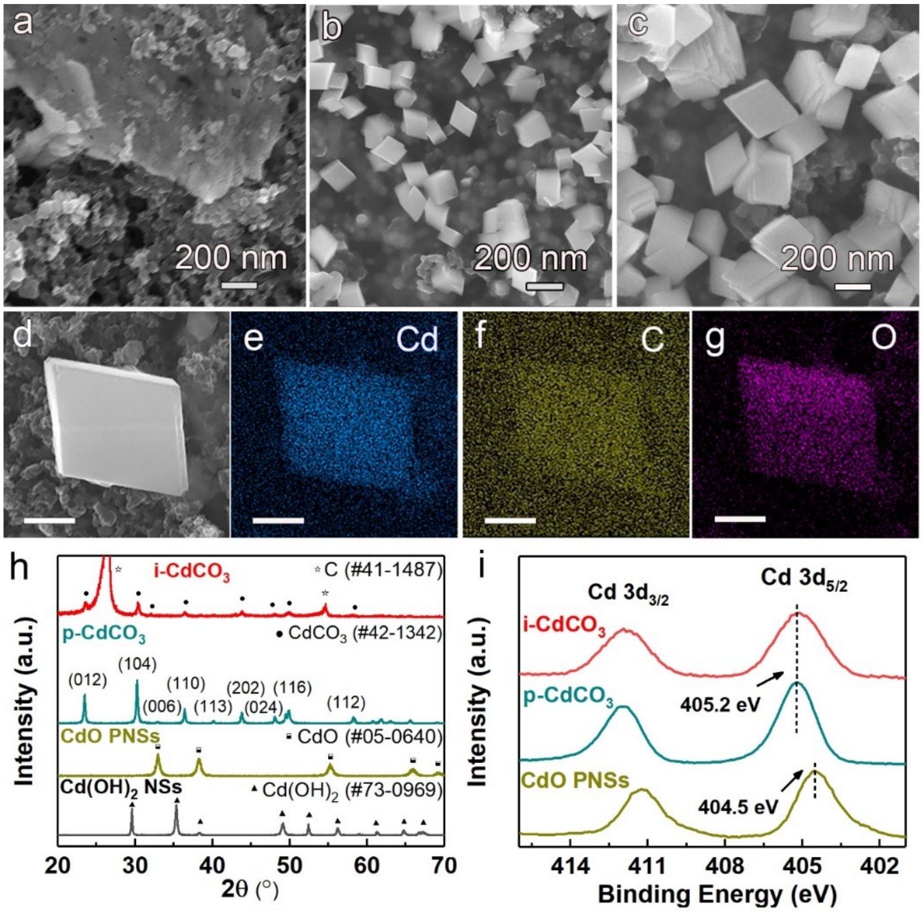

Figure 5.2 SEM images of i-$CdCO_3$ under different conditions: (a) prior to testing, and applied a potential of –1.26 V for (b) 1 min and (c) 90 min in CO_2-saturated 0.1 M $KHCO_3$; (d) SEM image of an i-$CdCO_3$ particle and (e-g) the corresponding EDS elemental mappings; (h) XRD patterns of $Cd(OH)_2$ NSs, CdO PNSs, p-$CdCO_3$ and i-$CdCO_3$ (The scale bar is 50 nm); (i) Cd 3d XPS spectra of CdO PNSs, p-$CdCO_3$ and i-$CdCO_3$.

To validate this assumption, the electrocatalytic activity of i-$CdCO_3$ was evaluated in a CO_2-saturated 0.1 M $KHCO_3$ electrolyte using p-$CdCO_3$ as the reference catalyst. To persuasively clarify the local pH effect on the CO_2RR performance, s-$CdCO_3$ (Figure S5.6) with similar morphology was prepared and also examined for CO_2RR. The cathodic polarization curves of all catalysts were recorded by linear sweep voltammetry (LSV) at a scan rate of 10 mV

s^{-1}. Clearly, i-$CdCO_3$ displays considerably higher current density (*j*, normalized by geometric area) than s-$CdCO_3$ and p-$CdCO_3$ over the measured potential range (Figure 5.3a), suggesting its enhanced catalytic activity. To get a better understanding of the CO_2RR activity as well as the product distribution, stepped potentiostatic CO_2 electrolysis was performed at potentials ranging from −0.26 to −1.26 V to periodically quantify the gaseous and liquid products by gas chromatography and ion chromatography, respectively. The results indicate that CO is the main CO_2RR product on i-$CdCO_3$, accompanied by a small amount of HCOOH detected at highly negative potentials (Figure S5.7). As a byproduct from HER, H_2 was also detected throughout the entire potential window. Figure 5.3b shows the potential-dependent FEs of CO on these $CdCO_3$ catalysts. As expected, i-$CdCO_3$ exhibits the highest FE of CO at all potentials as compared to s-$CdCO_3$ and p-$CdCO_3$. Specifically, i-$CdCO_3$ delivers a FE of over 90% for CO production in a broad potential range from −0.66 to −1.16 V, and reaches a maximum FE of 99.2% at −0.86 V, which is comparably higher than the FEs of many other state-of-the-art catalysts for CO formation (Table S5.1) [11, 16-18, 39-41], and also a recent work on $CdCO_3$ [42]. In contrast, s-$CdCO_3$ and p-$CdCO_3$ display lower CO selectivity, with the maximum FE of CO being 87.0% (at −0.86 V) and 75.9% (at −0.96 V), respectively. The difference in CO selectivity mainly corresponds to lower FEs for H_2 on i-$CdCO_3$ (Figure S5.8), which could be the result of inhibited HER caused by the local pH effect.

Figure 5.3c shows the potential-dependent CO partial current densities (j_{CO}s) of all the catalysts calculated based on steady-state *j* and corresponding FEs of CO. It clearly demonstrates the high catalytic activity of i-$CdCO_3$ towards CO formation with a j_{CO} of −24.8 mA cm^{-2} obtained at −1.26 V, which is nearly 2.1- and 3.3- fold higher than the values on s-$CdCO_3$ and p-$CdCO_3$, respectively. Currently, the reported mass activities on benchmarking materials for CO formation are typically less than 50 mA mg^{-1} at the potentials corresponding to the maximum FE (Table S5.1) [43-45], which severely hinders the widespread application of these materials. Surprisingly, i-$CdCO_3$ exhibits remarkably high mass activities (>50 mA mg^{-1}) in a wide potential window ranging from −0.86 to −1.26 V and achieves an ultrahigh value of 165.1 mA mg^{-1} at −1.26 V, exceeding s-$CdCO_3$ and p-$CdCO_3$ (Figure 5.3d). The superior mass activity is highly desirable for Cd-based catalysts considering their toxicity. The increase in mass activity on i-$CdCO_3$ can be attributed to the dense $CdCO_3$ crystals on the electrode surface, which ensures sufficient surface area in contact with the electrolyte, thereby boosting the number of effective active sites for CO_2RR. Therefore, i-$CdCO_3$ has sufficient potential as a promising catalyst for electrochemical CO_2RR with ultrahigh CO selectivity and mass activity, as well as good catalytic activity.

It is well-accepted that the improvement in the catalytic activity of catalysts may originate from the increased number of active sites and/or the enhanced intrinsic activity [8,46]. To differentiate these two factors, the electrochemically active surface areas (ECSAs) for all $CdCO_3$ catalysts were estimated by measuring double-layer capacitance (C_{dl}), and the results are shown in Figure 5.4a. Apparently, the i-$CdCO_3$ possesses the largest ECSA among these catalysts, with the C_{dl} value (5.7 mF cm^{-2}) being roughly 1.6 and 2.2 times higher than those of s-$CdCO_3$ and p-$CdCO_3$, respectively. The increased ECSA for i-$CdCO_3$ suggests a significant increase in the number of catalytically active sites, which endows i-$CdCO_3$ with increased CO_2 adsorption capacity, as demonstrated by the corresponding CO_2 adsorption isotherms in Figure 5.4b. A consensus has been reached that CO_2 adsorption is the prerequisite for CO_2RR in aqueous media [47] and hence, the increased CO_2 adsorption capacity of i-$CdCO_3$ ensures the continuous supply of reactants for subsequent CO_2RR. By comparing the ECSA-corrected j_{CO}s of the $CdCO_3$ catalysts (Figure S5.9), it is found that i-$CdCO_3$ exhibits higher intrinsic activity than the other two components. Therefore, the increased ECSA and the catalytically more active sites collectively contribute to the enhanced catalytic activity on i-$CdCO_3$.

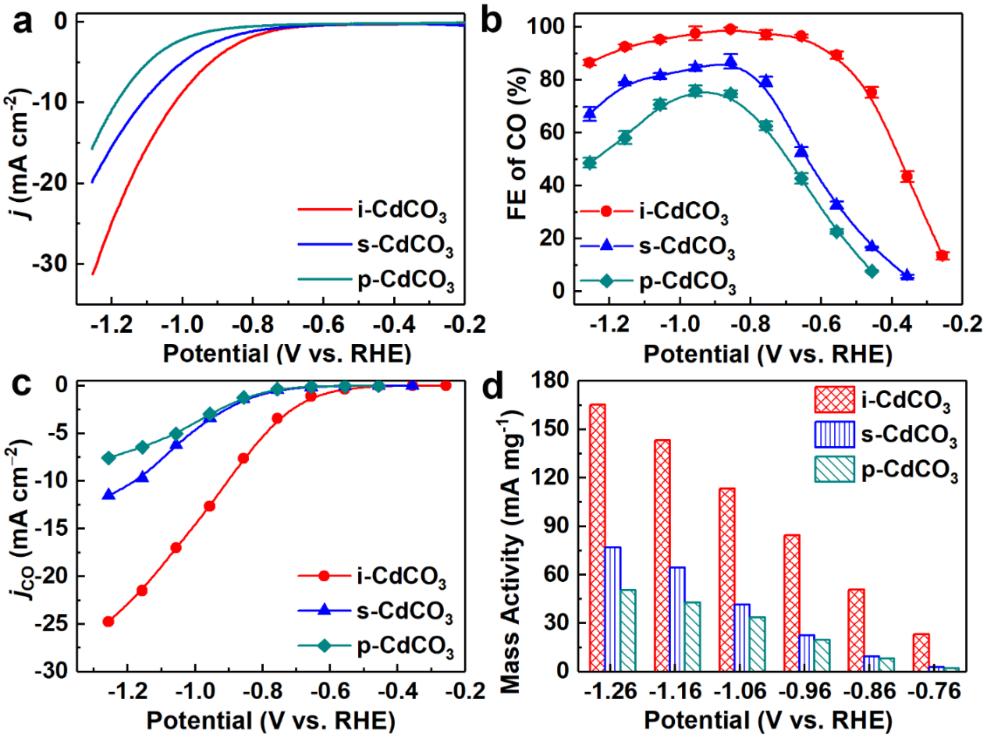

Figure 5.3 (a) LSV curves in CO_2-saturated 0.1 M $KHCO_3$ electrolyte; (b) potential-dependent FEs of CO, (d) *j*sCO and (e) mass activities of p-$CdCO_3$, s-$CdCO_3$ and i-$CdCO_3$.

To gain deep insights into the electrokinetic mechanism of CO_2RR on the $CdCO_3$ catalysts, Tafel analysis was performed and the results are shown in Figure 5.4c. It is commonly accepted that the process of CO_2RR to CO involves the transfer of two electrons and two protons [48]. Initially, one electron is transferred to an adsorbed CO_2 molecule to form $*CO_2^-$ intermediate, and then a *COOH intermediate is generated after receiving one proton [32,49].

Subsequently, the adsorbed *COOH experiences a proton-coupled electron transfer to form a *CO intermediate and a H_2O molecule. Finally, the *CO intermediate desorbs from the catalysts to produce CO. The rate-determining step can be uncovered by calculating the Tafel slope, an inherent property of catalysts. Compared with s-$CdCO_3$ (139 mV dec^{-1}) and p-$CdCO_3$ (150 mV dec^{-1}), i-$CdCO_3$ shows a relatively lower Tafel slope of 119 mV dec^{-1}, much close to the theoretical value of 118 mV dec^{-1} [20], indicating that the first one-electron transfer is the rate-determining step over i-$CdCO_3$. Indeed, the initial CO_2 activation generally requires a much more negative potential than the subsequent steps [20,50]. The lowed Tafel slope of i-$CdCO_3$ indicates a promoted kinetics for the formation of the $*CO_2^-$ intermediate. It can be inferred that the intrinsically more active sites on i-$CdCO_3$ offer improved stabilization for the $*CO_2^-$ intermediate, thereby lowering the energy barrier for CO_2 activation and eventually increasing the catalytic activity.

In addition to product selectivity and catalytic activity, stability is another crucial criterion to evaluate an advanced catalyst for CO_2RR. Hence, continuous CO_2RR was performed at a fixed potential of –0.86 V for 36 h to examine the stability of i-$CdCO_3$ (Figure 5.4d). The total j on i-$CdCO_3$ stabilizes at about 8.2 mA cm^{-2} with negligible variation, and the corresponding FE of CO remains at over 95%. Moreover, the morphology and composition of i-$CdCO_3$ are preserved after the stability test (Figure S5.10). In contrast, noticeable degradation of both j and FE of CO was observed on s-$CdCO_3$ after 36 h operation, which could be ascribed to the agglomeration of $CdCO_3$ crystals and thus the loss of active sites (Figure S5.11). The enhanced stability of i-$CdCO_3$ should be attributed to the stronger interaction between i-$CdCO_3$ and carbon support due to in-situ growth, which has been demonstrated to restrain the agglomeration of active sites effectively [51]. The good stability of i-$CdCO_3$ further confirms its superiority as a promising CO_2RR catalyst.

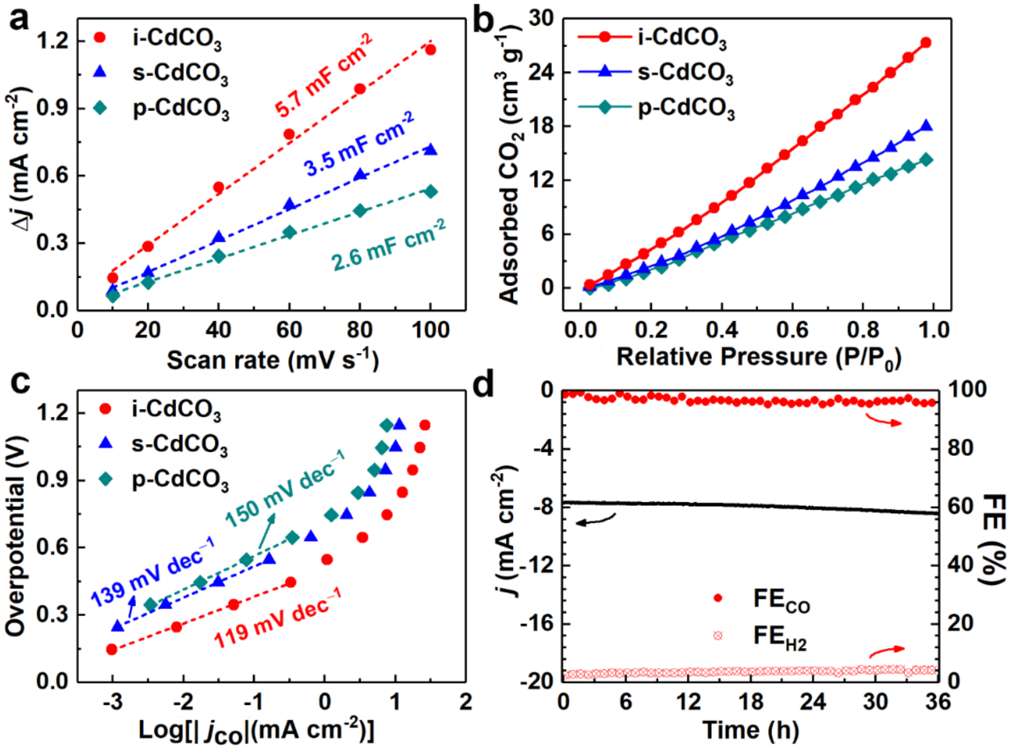

Figure 5.4 (a) Charging current density difference (Δ*j*) plotted against scan rates; (b) CO_2 adsorption isotherms and (c) Tafel plots of p- $CdCO_3$, s-$CdCO_3$ and i-$CdCO_3$; (d) stability test for i-$CdCO_3$ at a potential of –0.86 V.

Regarding the remarkably enhanced CO selectivity of i-$CdCO_3$ over s-$CdCO_3$ with similar morphology, the local pH effect is proposed to explain this phenomenon, as illustrated in Figure 5.5a. On one hand, the pH rises locally at the electrode/electrolyte interface as a consequence of releasing OH^- in the following cathode reactions [3,33]:

$$CO_2 + H_2O + 2e^- \rightarrow CO + 2OH^- \tag{5.2}$$

$$2H_2O + 2e^- \rightarrow H_2 + 2OH^- \tag{5.3}$$

On the other hand, the in-situ growth process of i-$CdCO_3$ also generates OH^- near the electrode surface according to the abovementioned Equation 5.1. Therefore, a higher local pH is developed near i-$CdCO_3$ than that near s-$CdCO_3$. It has been proven that an increase in pH will significantly lower the kinetics of HER [52] and hence, the higher local pH near i-$CdCO_3$ leads to the effective suppression of HER and subsequently the enhanced selectivity of CO_2RR to CO. Particularly, geometric j also affects the local pH by controlling the generation rate of OH^- [39,53]. To exclude the influence of j on the local pH, the FEs of CO for i-$CdCO_3$ and s-$CdCO_3$ were plotted against j instead of the applied potentials (Figure 5.5b). Clearly, i-$CdCO_3$ exhibits higher FEs of CO than s-$CdCO_3$ in the whole j range, suggesting that the variation in j is not sufficient to account for the different local pH environments and CO selectivities. This evidence indicates that the OH^- produced by the in-situ synthesis process plays an important role in the CO_2RR selectivity for $CdCO_3$ catalysts.

To better understand the local pH effect, the product selectivities of i-$CdCO_3$ and s-$CdCO_3$ were evaluated in CO_2-saturated 0.05 M K_2HPO_4, 0.1 M $KHCO_3$ and 0.1 M $KClO_4$ solutions, respectively. Figure 5.5c shows the FEs of CO on i-$CdCO_3$ in various electrolytes. As can be seen, the FEs of CO are dramatically decreased in 0.05 M K_2HPO_4 than the values in 0.1 M $KHCO_3$, which is consistent with the work on oxide-derived Ag [32]. This result is attributed to the better buffer ability of K_2HPO_4 ($pK_a = 7.2$) than $KHCO_3$ ($pK_a = 10.3$) [54], which makes it easier to neutralize generated OH^- near the electrode and keep a relatively low value of local pH. The lower local pH promotes HER (Figure S5.12), leading to the decreased CO selectivity. Similar results are obtained on s-$CdCO_3$ in 0.05 M K_2HPO_4 electrolyte (Figure S5.13). A relatively high local pH can be achieved in $KClO_4$ electrolyte, which does not have buffer ability. [54] As expected, the CO selectivity is improved on s-$CdCO_3$ by replacing 0.1

M $KHCO_3$ with 0.1 M $KClO_4$, where a maximum FE of 96.8% is obtained at –0.96 V (Figure S5.13). This evidence clearly reveals that the local pH effect has a significant impact on the CO_2RR selectivity.

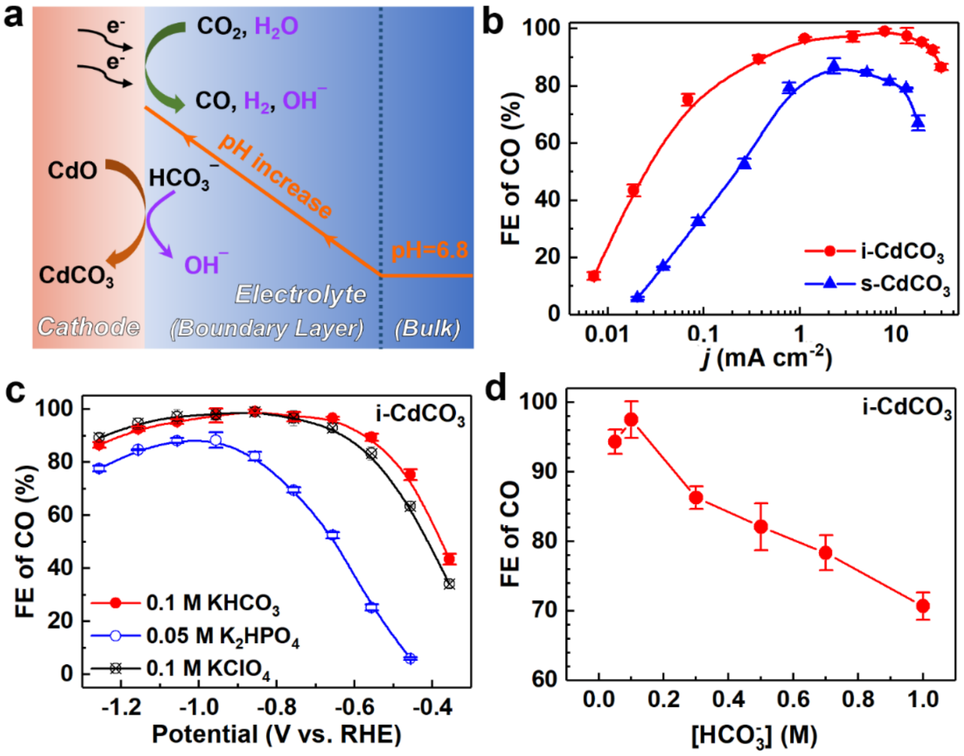

Figure 5.5 (a) Schematic illustration of local pH effect on i-$CdCO_3$; (b) FEs of CO as a function of *j* observed over s-$CdCO_3$ and i-$CdCO_3$; (c) potential-dependent FEs of CO on i-$CdCO_3$ in CO_2-saturated 0.05 M K_2HPO_4, 0.1 M $KHCO_3$ and 0.1 M $KClO_4$ electrolytes; (d) FEs of CO on i-$CdCO_3$ measured in various concentrations of $KHCO_3$.

To further examine the pH effect on the CO_2RR, CO_2 electrolysis was performed on i-$CdCO_3$ in various concentrations of $KHCO_3$ electrolytes at a potential of –0.96 V. The local pH drops with the increasing concentration of bicarbonate electrolytes owing to the enhanced buffer strength [53,54]. Therefore, the FE of CO on i-$CdCO_3$ declines monotonically with the increase of $KHCO_3$ concentration in the range of 0.1 M to 1 M (Figure 5.5d). This result further validates the fact that high local pH favors CO_2RR rather than HER to some extent. However, rising the local pH by conducting CO_2RR in more dilute (e.g., 0.05 M) bicarbonate electrolyte cannot further improve the CO selectivity on i-$CdCO_3$. Such a disparity may be related to the lowered CO_2 concentration, which can be explained by the equations below [29,53]:

$$CO_2 + OH^- \leftrightarrow HCO_3^- \tag{5.4}$$

$$HCO_3^- + OH^- \leftrightarrow CO_3^{2-} + H_2O \tag{5.5}$$

An extraordinarily high local pH will shift the equilibria of above acid-base reactions towards (bi)carbonates, which can reduce the CO_2 concentration near the electrode surface and decrease the reaction kinetics for CO_2RR. This also explains the comparable FEs of CO on i-$CdCO_3$ in 0.1 M $KHCO_3$ and 0.1 M $KClO_4$ electrolytes (Figure 5.5c). Based on these results, it seems likely that there is an optimum local pH that balances the benefits of increased pH and the unfavorable decline in CO_2 concentration. However, the measurement of local pH under the CO_2RR conditions remains as a big challenge, and it is unclear how local pH itself affects the adsorption energies of reaction intermediates. Considering the huge impact of local pH on the product selectivity, more experimental and theoretical work is highly encouraged to clarify the CO_2RR mechanisms related to local pH, so as to provide a scientific basis for optimizing the electrochemical CO_2RR performance through tuning the local pH.

5.3 Conclusions

In summary, we successfully introduced hydroxides by the revolution of porous CdO nanosheets to dense rhombohedral $CdCO_3$ crystals under in-situ electrochemical CO_2RR conditions. The obtained catalyst, denoted as i-$CdCO_3$, shows significantly higher current density and mass activity for CO formation, as compared to pre-synthesized $CdCO_3$ catalyst with similar morphology. Moreover, i-$CdCO_3$ displays remarkably increased CO FEs of over 90% in a wide potential window ranging from −0.66 to −1.16 V and achieves a maximum value of 99.2% at −0.86 V, outperforming most benchmarking catalysts for CO formation. The improved selectivity of CO is primarily attributed to an appropriate increase in local pH near the electrode surface, which effectively inhibits the competitive HER. These findings can significantly advance the current understanding on the local pH effect and provide new insights for designing inexpensive and selective catalyst systems for electrochemical CO_2RR.

5.4 References

[1] P. De Luna, C. Hahn, D. Higgins, et al., What would it take for renewably powered electrosynthesis to displace petrochemical processes?, Science 364 (2019) 3506.

[2] Y. Wu, S. Cao, J. Hou, et al., Rational design of nanocatalysts with nonmetal species modification for electrochemical CO_2 reduction, Adv. Energy Mater. 10 (2020) 2000588.

[3] J. Qiao, Y. Liu, F. Hong, et al., A review of catalysts for the electroreduction of carbon dioxide to produce low-carbon fuels, Chem. Soc. Rev. 43 (2014) 631-675.

[4] Z.-P. Liu, P. Hu, A new insight into Fischer−Tropsch synthesis, J. Am. Chem. Soc. 124 (2002) 11568-11569.

[5] F.-Y. Gao, R.-C. Bao, M.-R. Gao, et al., Electrochemical CO_2-to-CO conversion: electrocatalysts, electrolytes, and electrolyzers, J. Mater. Chem. A 8 (2020) 15458-15478.

[6] W. Zheng, J. Yang, H. Chen, et al., Atomically defined undercoordinated active sites for highly efficient CO_2 electroreduction, Adv. Funct. Mater. 30 (2020) 1907658.

[7] P. Prabhu, V. Jose, J.M. Lee, Heterostructured catalysts for electrocatalytic and photocatalytic carbon dioxide reduction, Adv. Funct. Mater. 30 (2020) 1910768.

[8] M. Li, S. Garg, X. Chang, et al., Toward excellence of transition metal-based catalysts for CO_2 electrochemical reduction: an overview of strategies and rationales., Small Methods 4 (2020) 2000033.

[9] W. Zhu, R. Michalsky, O. Metin, et al., Monodisperse Au nanoparticles for selective electrocatalytic reduction of CO_2 to CO, J. Am. Chem. Soc. 135 (2013) 16833-16836.

[10] M. Asadi, K. Kim, C. Liu, et al., Nanostructured transition metal dichalcogenide electrocatalysts for CO_2 reduction in ionic liquid, Science 353 (2016) 467-470.

[11] R. He, A. Zhang, Y. Ding, et al., Achieving the widest range of syngas proportions at high current density over cadmium sulfoselenide nanorods in CO_2 electroreduction, Adv. Mater. 30 (2018) 1705872.

[12] J. Wu, R.M. Yadav, M. Liu, et al., Achieving highly efficient, selective, and stable CO_2 reduction on nitrogen-doped carbon nanotubes, ACS nano 9 (2015) 5364-5371.

[13] X. Duan, J. Xu, Z. Wei, et al., Metal-free carbon materials for CO_2 electrochemical reduction, Adv. Mater. 29 (2017) 1701784.

[14] S. Ren, D. Joulié, D. Salvatore, et al., Molecular electrocatalysts can mediate fast, selective CO_2 reduction in a flow cell, Science 365 (2019) 367-369.

[15] S. Lin, C.S. Diercks, Y.-B. Zhang, et al., Covalent organic frameworks comprising cobalt porphyrins for catalytic CO_2 reduction in water, Science 349 (2015) 1208-1213.

[16] W. Zhu, Y.-J. Zhang, H. Zhang, et al., Active and selective conversion of CO_2 to CO on ultrathin Au nanowires., J. Am. Chem. Soc. 136 (2014) 16132-16135.

[17] S. Liu, H. Tao, L. Zeng, et al., Shape-dependent electrocatalytic reduction of CO_2 to CO on triangular silver nanoplates, J. Am. Chem. Soc. 139 (2017) 2160-2163.

[18] D. Gao, H. Zhou, J. Wang, et al., Size-dependent electrocatalytic reduction of CO_2 over Pd nanoparticles, J. Am. Chem. Soc. 137 (2015) 4288-4291.

[19] R. Reske, H. Mistry, F. Behafarid, et al., Particle size effects in the catalytic electroreduction of CO_2 on Cu nanoparticles, J. Am. Chem. Soc. 136 (2014) 6978-6986.

[20] Y. Chen, C.W. Li, M.W. Kanan, Aqueous CO_2 reduction at very low overpotential on oxide-derived Au nanoparticles, J. Am. Chem. Soc. 134 (2012) 19969-19972.

[21] R.G. Mariano, K. McKelvey, H.S. White, et al., Selective increase in CO_2 electroreduction activity at grain-boundary surface terminations, Science 358 (2017) 1187-1192.

[22] S. Liu, J. Xiao, X.F. Lu, et al., Efficient electrochemical reduction of CO_2 to HCOOH over Sub-2 nm SnO_2 quantum wires with exposed grain boundaries, Angew. Chem. Int. Ed. 58 (2019) 8499-8503.

[23] W.D. Hye, S. Hyeyoung, K. Jaekang, et al., Highly efficient, selective, and stable CO_2 electroreduction on a hexagonal Zn catalyst, Angew. Chem. Int. Ed. 55 (2016) 9297-9300.

[24] A. Klinkova, P. De Luna, C.-T. Dinh, et al., Rational design of efficient palladium catalysts for electroreduction of carbon dioxide to formate, ACS Catal.6 (2016) 8115-8120.

[25] Z. Sun, T. Ma, H. Tao, et al., Fundamentals and challenges of electrochemical CO_2 reduction using two-dimensional materials, Chem 3 (2017) 560-587.

[26] B. Qin, Y. Li, H. Wang, et al., Efficient electrochemical reduction of CO_2 into CO promoted by sulfur vacancies, Nano Energy 60 (2019) 43-51.

[27] A.S. Varela, M. Kroschel, T. Reier, et al., Controlling the selectivity of CO_2 electroreduction on copper: The effect of the electrolyte concentration and the importance of the local pH, Catal. Today 260 (2016) 8-13.

[28] S. Ringe, E.L. Clark, J. Resasco, et al., Understanding cation effects in electrochemical CO_2 reduction, Energy Environ. Sci. 12 (2019) 3001-3014.

[29] S. Nitopi, E. Bertheussen, S.B. Scott, et al., Progress and perspectives of electrochemical CO_2 reduction on copper in aqueous electrolyte, Chem. Rev. 119 (2019) 7610-7672.

[30] Y. Hori, A. Murata, R. Takahashi, Formation of hydrocarbons in the electrochemical reduction of carbon dioxide at a copper electrode in aqueous solution, J. Chem. Soc., Faraday Trans. 1 85 (1989) 2309-2326.

[31] M. Ma, K. Djanashvili, W.A. Smith, Controllable hydrocarbon formation from the electrochemical reduction of CO_2 over Cu nanowire arrays, Angew. Chem. Int. Ed. 55 (2016) 6680-6684.

[32] M. Ma, B.J. Trześniewski, J. Xie, et al., Selective and efficient reduction of carbon dioxide to carbon monoxide on oxide-derived nanostructured silver electrocatalysts, Angew. Chem. 128 (2016) 9900-9904.

[33] C. Chen, B. Zhang, J. Zhong, et al., Selective electrochemical CO_2 reduction over highly porous gold films, J. Mater. Chem. A 5 (2017) 21955-21964.

[34] A. Goyal, G. Marcandalli, V.A. Mints, et al., Competition between CO_2 reduction and hydrogen evolution on a gold electrode under well-defined mass transport conditions, J. Am. Chem. Soc. 142 (2020) 4154-4161.

[35] W. Li, M. Li, S. Xie, et al., Improving the photoelectrochemical and photocatalytic performance of CdO nanorods with CdS decoration, CrystEngComm 15 (2013) 4212-4216.

[36] W.J. Dufresne, C.J. Rufledt, C.P. Marshall, Raman spectroscopy of the eight natural carbonate minerals of calcite structure, J. Raman Spectrosc., 49 (2018) 1999-2007.

[37] H. Li, H.L. Xin, D.A. Muller, et al., Visualizing the 3D internal structure of calcite single crystals grown in agarose hydrogels, Science 326 (2009) 1244-1247.

[38] S. Weiner, L. Addadi, Design strategies in mineralized biological materials, J. Mater. Chem. 7 (1997) 689-702.

[39] W. Luo, J. Zhang, M. Li, et al., Boosting CO production in electrocatalytic CO_2 reduction on highly porous Zn catalysts, ACS Catal. (2019) 3783-3791.

[40] K. Liu, J. Wang, M. Shi, et al., Simultaneous achieving of high Faradaic efficiency and CO partial current density for CO_2 reduction via robust, noble-metal-free Zn nanosheets with favorable adsorption energy, Adv. Energy Mater. 9 (2019) 1900276.

[41] S. Rasul, D.H. Anjum, A. Jedidi, et al., A highly selective copper–indium bimetallic electrocatalyst for the electrochemical reduction of aqueous CO_2 to CO, Angew. Chem. Int. Ed. 54 (2015) 2146-2150.

[42] X. Jiang, X. Wang, Q. Wang, et al., Efficient activation and electroreduction of carbon dioxide on an electrocatalyst cadmium carbonate, ACS Appl Energy Mater. 4 (2021) 2073-2080.

[43] D. Gao, H. Zhou, F. Cai, et al., Pd-containing nanostructures for electrochemical CO_2 reduction reaction, ACS Catal. 8 (2018) 1510-1519.

[44] S. Liu, H. Tao, Q. Liu, et al., Rational design of silver sulfide nanowires for efficient CO_2 electroreduction in ionic liquid, ACS Catal. 8 (2018) 1469-1475.

[45] W. Ju, A. Bagger, G.-P. Hao, et al., Understanding activity and selectivity of metal-nitrogen-doped carbon catalysts for electrochemical reduction of CO_2, Nat. Commun. 8 (2017) 944.

[46] E.L. Clark, J. Resasco, A. Landers, et al., Standards and protocols for data acquisition and reporting for studies of the electrochemical reduction of carbon dioxide, ACS Catal. 8 (2018) 6560-6570.

[47] R. Kortlever, J. Shen, K.J.P. Schouten, et al., Catalysts and reaction pathways for the electrochemical reduction of carbon dioxide, J. Phys. Chem. Lett. 6 (2015) 4073-4082.

[48] Y. Hori, H. Wakebe, T. Tsukamoto, et al., Electrocatalytic process of CO selectivity in electrochemical reduction of CO_2 at metal electrodes in aqueous media, Electrochim. Acta 39 (1994) 1833-1839.

[49] J. Rosen, G.S. Hutchings, Q. Lu, et al., Mechanistic insights into the electrochemical reduction of CO_2 to CO on nanostructured Ag surfaces, ACS Catal. 5 (2015) 4293-4299.

[50] Q. Lu, J. Rosen, Y. Zhou, et al., A selective and efficient electrocatalyst for carbon dioxide reduction, Nat. Commun. 5 (2014) 3242.

[51] F. Li, L. Chen, G.P. Knowles, et al., Hierarchical mesoporous SnO_2 nanosheets on carbon cloth: a robust and flexible electrocatalyst for CO_2 reduction with high efficiency and selectivity, Angew. Chem. 129 (2017) 520-524.

[52] D. Strmcnik, P.P. Lopes, B. Genorio, et al., Design principles for hydrogen evolution reaction catalyst materials, Nano Energy 29 (2016) 29-36.

[53] N. Gupta, M. Gattrell, B. MacDougall, Calculation for the cathode surface concentrations in the electrochemical reduction of CO_2 in $KHCO_3$ solutions, J. Appl. Electrochem. 36 (2006) 161-172.

[54] Y. Hori, Modern Aspects of Electrochemistry 42, Springer New York, 2008, pp. 89-189.

5.5 Supporting information

5.5.1 Supporting figures and tables

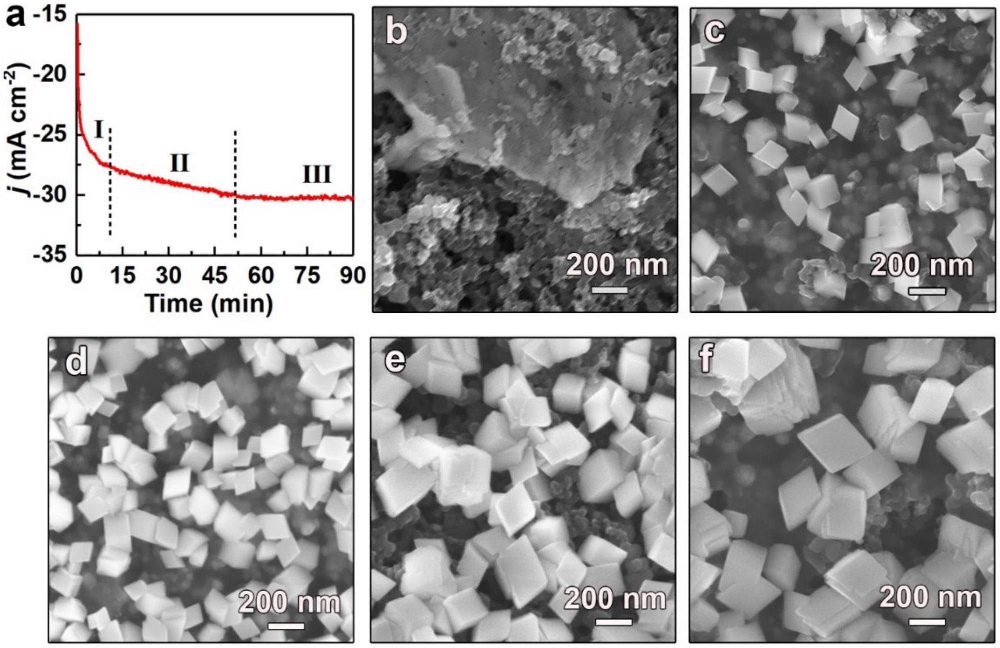

Figure S5.1 (a) Records of current density (*j*) with time during the preparation of i-$CdCO_3$ at –1.26 V in CO_2-bubbled 0.1 M $KHCO_3$ electrolyte. SEM images of i-$CdCO_3$ under different conditions: (b) prior to testing, and applied potential for (c) 1 min, (d) 10 min, (e) 30 min, and (f) 90 min.

The *j-t* curves of the as-prepared i-$CdCO_3$ can be divided into three stages (Figure S5.1a), i.e., stage I (0-10 min) with *j* sharply increasing, stage II (10-50 min) with *j* mildly growing, and stage III (>50 min) with almost constant *j*. The morphology evolution in each stage was investigated by SEM. As shown in Figure S5.1, rhombohedral $CdCO_3$ crystals with a size of about 100 nm formed and accumulated at the electrode surface at stage I (Figs. S5.1c and S5.1d), and then gradually grown at stage II (Figure S5.1e), finally reached a certain size of 200-300 nm at stage III (Figure S5.1f).

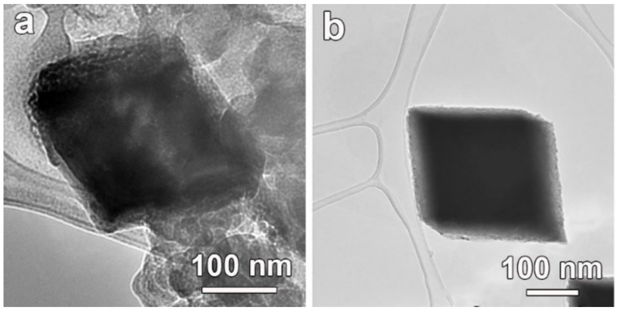

Figure S5.2 TEM images of i-$CdCO_3$.

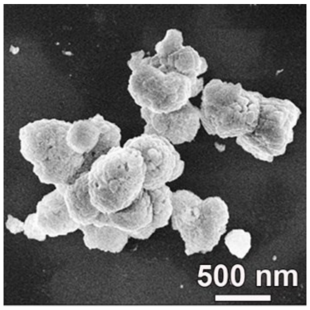

Figure S5.3 SEM image of p-$CdCO_3$.

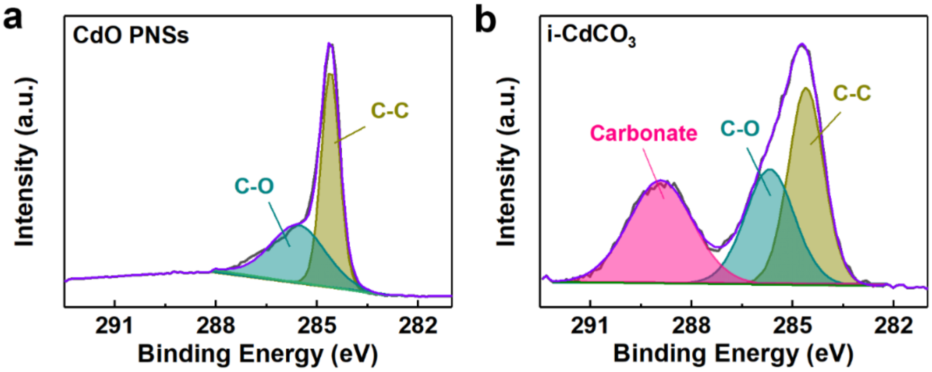

Figure S5.4 XPS spectra of C 1s for (a) CdO PNSs and (b) i-$CdCO_3$.

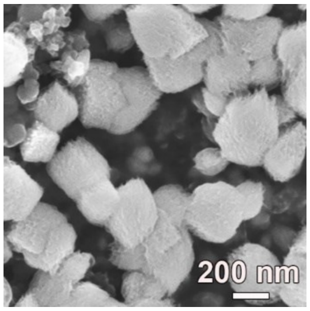

Figure S5.5 SEM image of $CdCO_3$ particles prepared by applying a potential of –1.26 V on CdO PNSs for 90 min in Ar-bubbled 0.1 M $KHCO_3$ electrolyte.

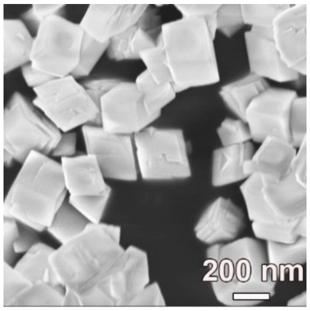

Figure S5.6 SEM image of s-$CdCO_3$.

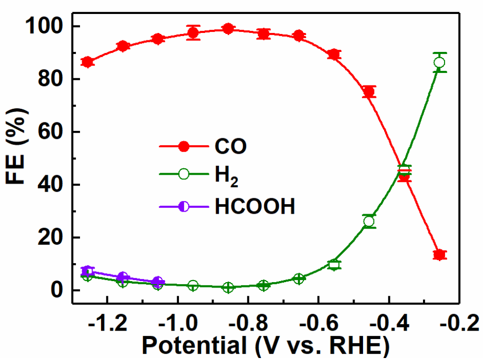

Figure S5.7 Potential-dependent FEs of all reduction products over i-$CdCO_3$.

Table S5.1 Comparison of CO$_2$RR performance for CO production over i-CdCO$_3$ and other state-of-the-art catalysts in bicarbonate electrolytes.

Catalysts	**Electrolyte**	***E* (V)**	**$j_{\rm co}$ (mA cm^{-2})**	**FE of CO**	**Mass activity[a] (mA mg^{-1})**
i-CdCO$_3$ (This work)	0.1 M KHCO$_3$	–1.26	–24.8	86.6%	165.1
		–1.16	–21.5	92.5%	143.3
		–1.06	–17.0	95.3%	113.4
		–0.96	–12.7	97.5%	84.4
		–0.86	–7.6	99.2%	50.9
		–0.76	–3.5	97.2%	23.0
		–0.66	–1.1	96.5%	7.2
Au nanowires [S1]	0.5 M KHCO$_3$	–0.35	–8.2	94%	1.8
Ag nanoplates [S2]	0.1 M KHCO$_3$	–0.86	–1.3	96.8%	2.0
Ag NPs [S3]	0.5 M KHCO$_3$	–0.75	–3.5	84.4%	~40
Pd NPs [S4]	0.1 M KHCO$_3$	–0.89	–8.9	91.2%	23.9
PdCu NPs [S5]	0.1 M KHCO$_3$	–0.89	–6.9	86%	24.5
Ag$_2$S NWs [S6]	0.1 M KHCO$_3$	–0.756	–0.8	41.7%	~1.3
Porous Zn [S7]	0.1 M KHCO$_3$	–0.95	–27.0	94.4%	4.2
Zn nanosheets [S8]	0.1 M KHCO$_3$	–1.0	~–7.2	90%	~3.6
CdS nanorods [S9]	0.1 M KHCO$_3$	–1.2	–21.9	81%	67.8
Cu-In [S10]	0.1 M KHCO$_3$	–0.6	~–0.6	85%	N.R.[b]
Cu-Sn [S11]	0.1 M KHCO$_3$	–0.6	–1.0	~90%	N.R.
N-CNTs [S12]	0.1 M KHCO$_3$	–0.78	–0.8	80%	1.6
Ni-N-C [S13]	0.1 M NaHCO$_3$	–0.75	–4.8	~85%	~9
CoPc/CNT [S14]	0.1 M NaHCO$_3$	–0.63	–15.0	98%	37.5

[a] Mass activities were calculated based on the reported $j_{\rm CO}$ and catalyst loadings.

[b] N.R.: not reported.

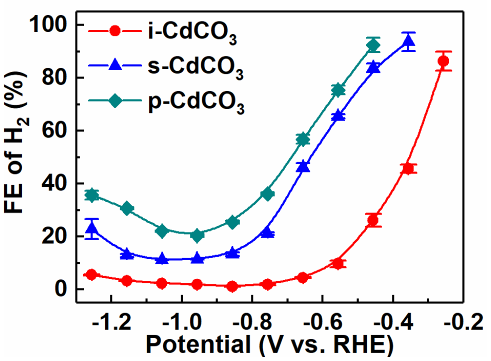

Figure S5.8 Potential-dependent FEs of H_2 on i-$CdCO_3$, s-$CdCO_3$ and p-$CdCO_3$.

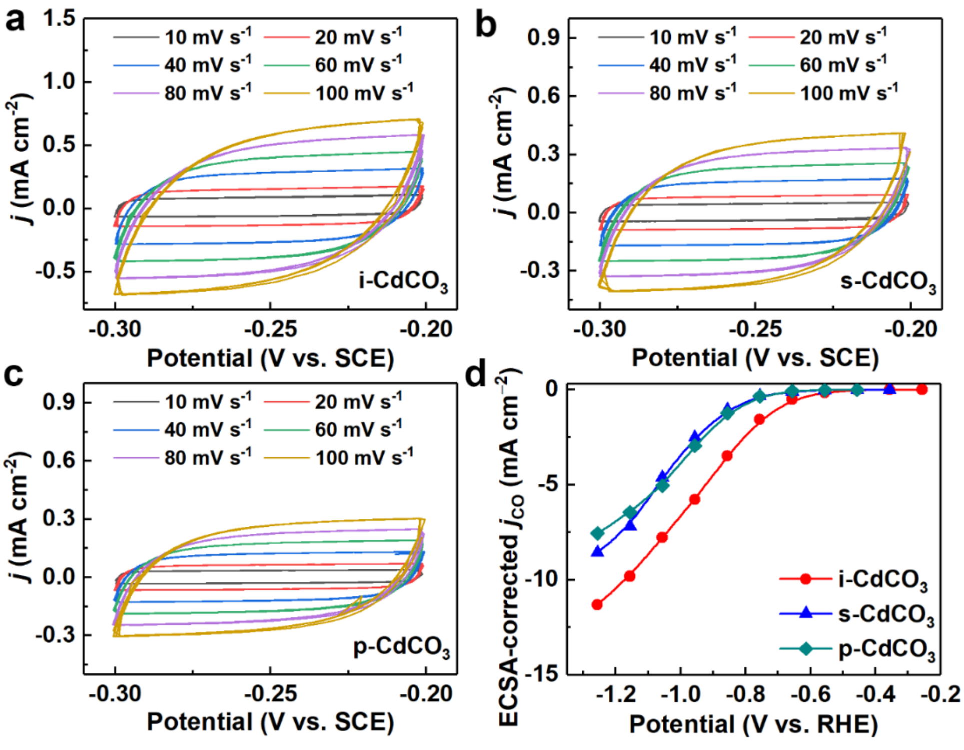

Figure S5.9 CVs of (a) i-$CdCO_3$, (b) s-$CdCO_3$, and (c) p-$CdCO_3$ with a potential range from –0.2 to –0.3 V vs. SCE in an CO_2-saturated 0.1 M $KHCO_3$ solution; (d) ECSA-corrected j_{SCO} of i-$CdCO_3$, s-$CdCO_3$-CB and p-$CdCO_3$.

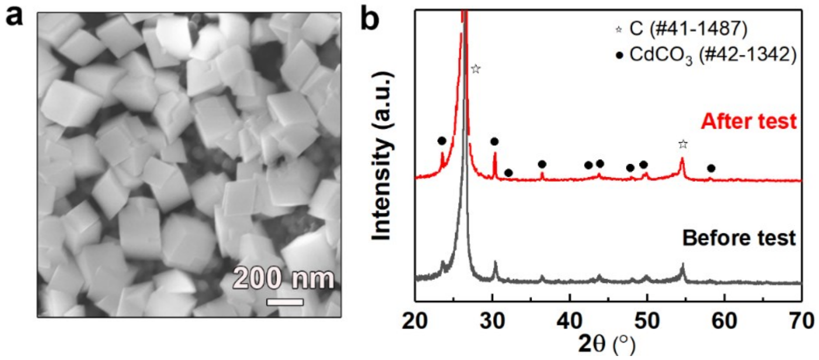

Figure S5.6 (a) SEM image of i-CdCO$_3$ after stability test and (b) XRD patterns of i-CdCO$_3$ before and after stability test. The C peaks are originated from carbon paper.

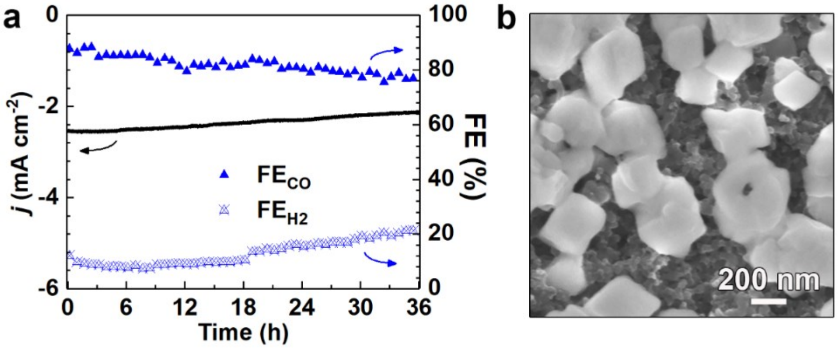

Figure S5.7 (a) Stability test for s-CdCO$_3$ and (b) SEM image for s-CdCO$_3$ after stability test.

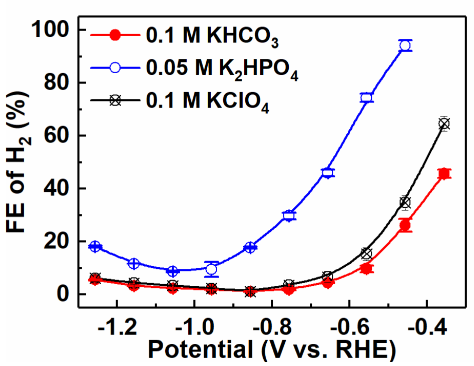

Figure S5.8 Potential-dependent FEs of H$_2$ on i-CdCO$_3$ in CO$_2$-saturated 0.05 M K$_2$HPO$_4$, 0.1 M KHCO$_3$ and 0.1 M KClO$_4$ electrolytes.

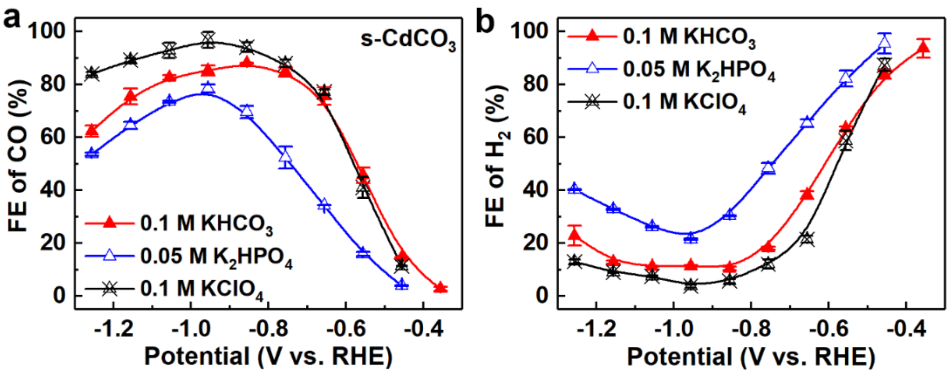

Figure S5.9 (a) Potential-dependent FEs of CO and (b) FEs of H_2 on s-$CdCO_3$ in CO_2-saturated 0.05 M K_2HPO_4, 0.1 M $KHCO_3$ and 0.1 M $KClO_4$ electrolytes.

5.5.2 Supporting references

[S1] W. Zhu, Y.-J. Zhang, H. Zhang, et al., Active and selective conversion of CO_2 to CO on ultrathin Au nanowires., J. Am. Chem. Soc. 136 (2014) 16132-16135.

[S2] S. Liu, H. Tao, L. Zeng, et al., Shape-dependent electrocatalytic reduction of CO_2 to CO on triangular silver nanoplates, J. Am. Chem. Soc. 139 (2017) 2160-2163.

[S3] C. Kim, H. S. Jeon, T. Eom, et al., Achieving selective and efficient electrocatalytic activity for CO_2 reduction using immobilized silver nanoparticles, J. Am. Chem. Soc. 137 (2015) 13844-13850.

[S4] D. Gao, H. Zhou, J. Wang, et al., Size-dependent electrocatalytic reduction of CO_2 over Pd nanoparticles, J. Am. Chem. Soc. 137 (2015) 4288-4291.

[S5] Z. Yin, D. Gao, S. Yao, et al., Highly selective palladium-copper bimetallic electrocatalysts for the electrochemical reduction of CO_2 to CO, Nano Energy 27 (2016) 35-43.

[S6] S. Liu, H. Tao, Q. Liu, et al., Rational design of silver sulfide nanowires for efficient CO_2 electroreduction in ionic liquid, ACS Catal. 8 (2018) 1469-1475.

[S7] W. Luo, J. Zhang, M. Li, et al., Boosting CO production in electrocatalytic CO_2 reduction on highly porous Zn catalysts, ACS Catal. (2019) 3783-3791.

[S8] K. Liu, J. Wang, M. Shi, et al., Simultaneous achieving of high Faradaic efficiency and CO partial current density for CO_2 reduction via robust, noble-metal-free Zn nanosheets with favorable adsorption energy, Adv. Energy Mater. 9 (2019) 1900276.

[S9] R. He, A. Zhang, Y. Ding, et al., Achieving the widest range of syngas proportions at high current density over cadmium sulfoselenide nanorods in CO_2 electroreduction, Adv. Mater. 30 (2018) 1705872.

[S10] S. Rasul, D.H. Anjum, A. Jedidi, et al., A highly selective copper–indium bimetallic electrocatalyst for the electrochemical reduction of aqueous CO_2 to CO, Angew. Chem. Int. Ed. 54 (2015) 2146-2150.

[S11] S. Sarfraz, A.T. Garcia-Esparza, A. Jedidi, et al., Cu–Sn bimetallic catalyst for selective aqueous electroreduction of CO_2 to CO, ACS Catal. 6 (2016) 2842-2851.

[S12] J. Wu, R.M. Yadav, M. Liu, et al., Achieving highly efficient, selective, and stable CO_2 reduction on nitrogen-doped carbon nanotubes, ACS nano 9 (2015) 5364-5371.

[S13] W. Ju, A. Bagger, G.-P. Hao, et al., Understanding activity and selectivity of metal-nitrogen-doped carbon catalysts for electrochemical reduction of CO_2, Nat. Commun. 8 (2017) 944.

[S14] X. Zhang, Z. Wu, X. Zhang, et al., Highly selective and active CO_2 reduction electrocatalysts based on cobalt phthalocyanine/carbon nanotube hybrid structures, Nat. commun. 8 (2017) 14675.

Chapter 6. Summary and Future Prospects

6.1 Summary

This dissertation focused on designing highly selective and efficient Zn- and Cd-based catalysts for the CO_2RR towards CO production, and investigating the factors governing their CO_2RR performance. Firstly, hexagonal Zn nanoplates (H-Zn-NPs) enclosed by Zn(100) and Zn(002) facets were successfully synthesized and explored their shape-dependent CO_2RR performance. Compared with spherical-like Zn nanoparticles and Zn foil, H-Zn-NPs exhibit enhanced catalytic activity and CO selectivity in a wide potential window. Particularly, H-Zn-NPs achieve a maximum FE of 94.2% is at −0.96 V, outperforming most of the reported Zn-based catalysts. DFT calculation results indicate that the enhanced CO_2RR performance is ascribed to an increased number of Zn(100) and edge atoms, which lower the energy barrier of the initial electron-transfer process and thereby facilitating the CO_2RR to CO. This study identifies the active sites on Zn catalysts for CO_2RR, and provides a straightforward approach to improve the CO_2RR performance over Zn catalysts through tuning the catalysts' shape and subsequently maximizing the percentage of these active sites.

Secondly, $CdCO_3$ nanoparticles decorated carbon nanofibers ($CdCO_3$-CNFs) were synthesized and investigated the effect of catalyst-support interactions on the CO_2RR performance. $CdCO_3$ has shown good CO selectivity at less negative potentials. Moreover, according to the theoretical results in this study, $CdCO_3$ processes appropriate binding energies of the key intermediates for CO production, together with a good electrochemical stability under the CO_2RR conditions. However, the current density of $CdCO_3$ is still unsatisfactory. Therefore, the well-designed $CdCO_3$-CNFs were constructed to boost the catalytic activity via a strong interaction between the $CdCO_3$ catalyst and the carbon support. The presence of such interaction, which is evidenced by XPS and UPS results, enables the fast electron transfer and the stabilization of active sites on $CdCO_3$-CNFs during the CO_2RR. As a result, $CdCO_3$-CNFs are able to achieve high partial current density (~10 mA cm^{-2}) and selectivity of CO (93.4%)) simultaneously at a moderately negative potential (–0.83 V). The superior catalytic activity, along with good stability of over 24 h, endows the $CdCO_3$-CNFs as a promising CO_2RR electrocatalyst to replace noble metals towards CO production. This study exemplifies a rational design for fabricating highly efficient and robust Cd-based catalysts for the electrochemical CO_2RR via developing a strong catalyst-support interaction.

Finally, to further improve the CO selectivity, in-situ generated hydroxides were introduced by the synthesis of rhombohedral $CdCO_3$ crystals (i-$CdCO_3$) under electrochemical CO_2RR conditions. The generated hydroxides contribute to an increased local pH at the electrode/electrolyte interface, thereby effectively inhibiting HER. As a result, the obtained i-$CdCO_3$ exhibits remarkably high FE of CO (over 90%) in a broad potential range, where a near 100% selectivity is achieved, exceeding a pre-synthesized $CdCO_3$ and most benchmarking catalysts for CO formation. Additionally, the local pH effect on the product selectivity of i-$CdCO_3$ was investigated by employing various aqueous electrolytes with different buffer abilities. The results suggest that there is an optimum local pH that balances the benefits of increased pH and the unfavorable decline in CO_2 concentration. These findings can significantly advance the current understanding on the local pH effect and provide new insights for designing inexpensive and selective catalyst systems for electrochemical CO_2RR.

6.2 Future prospects

The suggestions of future work are briefly listed below, and hopefully, they can serve as guidelines and inspirations for researchers who are dedicated to developing Zn- and Cd-based catalysts for efficient, robust and inexpensive CO_2RR.

(1) *Further enhancement in the catalytic activity and stability of Zn- and Cd-based catalysts*

Although appreciable CO selectivity has been achieved on Zn- and Cd-based catalysts in this work, the current density and the overpotential still fall short of the practical requirement for electrochemical CO_2RR. To this end, new strategies are essential for developing Zn- and Cd-based catalysts with higher current density and lower overpotential while maintaining high CO selectivity. Moreover, the stability of catalysts should be improved to suppress degradation and poisoning, so as to make the CO_2RR economically feasible for long-term (> 1000 h) operation.

(2) *Deeper understanding of the factors governing the CO_2RR performance*

The mechanistic understanding associated with the factors governing the CO_2RR performance is still lacking. In situ characterization technologies are highly desirable to record the CO_2RR process systematically and precisely under various experimental conditions. More importantly, the integrated information from these in situ characterization techniques together with theoretical calculations may bring deeper insights into the relationship of catalysts' structure, local environment and the CO_2RR performance.

(3) *Development of efficient full cell reactor*

Traditional H-type electrolyzers can only work for tens of hours and exhibit a limited current density of less than 100 mA cm^{-2}, which does not meet the requirements for industrial production. Thus, liquid electrolyte flow cell, membrane electrode assembly (MEA) cell [containing gas diffusion electrode (GDE) and ion-exchange membrane], are highly recommended to solve these problems.

Bibliography

[1] J. Rogelj, D. Huppmann, V. Krey, et al., A new scenario logic for the Paris Agreement long-term temperature goal, Nature 573 (2019) 357-363.

[2] S. Fawzy, A.I. Osman, J. Doran, et al., Strategies for mitigation of climate change: a review, Environ. Chem. Lett. 18 (2020) 2069-2094.

[3] P. De Luna, C. Hahn, D. Higgins, et al., What would it take for renewably powered electrosynthesis to displace petrochemical processes?, Science 364 (2019) 3506.

[4] E.S. Rubin, J.E. Davison, H.J. Herzog, The cost of CO_2 capture and storage, Int. J. Greenh. Gas Control 40 (2015) 378-400.

[5] A. Saravanan, D.-V.N. Vo, S. Jeevanantham, et al., A comprehensive review on different approaches for CO_2 utilization and conversion pathways, Chem. Eng. Sci. 236 (2021) 116515.

[6] R. Zhao, P. Ding, P. Wei, et al., Recent progress in electrocatalytic methanation of CO_2 at ambient conditions, Adv. Funct. Mater. 31 (2021) 2009449.

[7] Y. Zheng, W. Zhang, Y. Li, et al., Energy related CO_2 conversion and utilization: Advanced materials/nanomaterials, reaction mechanisms and technologies, Nano Energy 40 (2017) 512-539.

[8] K.P. Kuhl, T. Hatsukade, E.R. Cave, et al., Electrocatalytic conversion of carbon dioxide to methane and methanol on transition metal surfaces, J. Am. Chem. Soc. 136 (2014) 14107-14113.

[9] S. Nitopi, E. Bertheussen, S.B. Scott, et al., Progress and perspectives of electrochemical CO_2 reduction on copper in aqueous electrolyte, Chem. Rev. 119 (2019) 7610-7672.

[10] A.J. Martín, G.O. Larrazábal, J. Pérez-Ramírez, Towards sustainable fuels and chemicals through the electrochemical reduction of CO_2: lessons from water electrolysis, Green Chem. 17 (2015) 5114-5130.

[11] M. Valenti, N.P. Prasad, R. Kas, et al., Suppressing H_2 evolution and promoting selective CO_2 electroreduction to CO at low overpotentials by alloying Au with Pd, ACS Catal. 9 (2019) 3527-3536.

[12] W. Zhu, R. Michalsky, O. Metin, et al., Monodisperse Au nanoparticles for selective electrocatalytic reduction of CO_2 to CO, J. Am. Chem. Soc. 135 (2013) 16833-16836.

[13] R. Kortlever, I. Peters, S. Koper, et al., Electrochemical CO_2 reduction to formic acid at low overpotential and with high faradaic efficiency on carbon-supported bimetallic Pd–Pt nanoparticles, ACS Catal. 5 (2015) 3916-3923.

[14] P. Ding, H. Zhao, T. Li, et al., Metal-based electrocatalytic conversion of CO_2 to formic acid/formate, J. Mater. Chem. A 8 (2020) 21947-21960.

[15] K. Nakata, T. Ozaki, C. Terashima, et al., High-yield electrochemical production of formaldehyde from CO_2 and seawater, Angew. Chem. Int. Ed. 53 (2014) 871-874.

[16] J.-M. Saveant, C. Tard, Attempts to catalyze the electrochemical CO_2-to-methanol conversion by biomimetic $2e^- + 2H^+$ transferring molecules, J. Am. Chem. Soc. 138 (2016) 1017-1021.

[17] W.-J. Ong, L.-L. Tan, S.-P. Chai, et al., Self-assembly of nitrogen-doped TiO_2 with exposed {001} facets on a graphene scaffold as photo-active hybrid nanostructures for reduction of carbon dioxide to methane, Nano Res. 7 (2014) 1528-1547.

[18] Y. Li, F. Cui, M.B. Ross, et al., Structure-Sensitive CO_2 electroreduction to hydrocarbons on ultrathin 5-fold twinned copper nanowires, Nano Lett. 17 (2017) 1312-1317.

[19] T.-C. Chou, C.-C. Chang, H.-L. Yu, et al., Controlling the oxidation state of the Cu electrode and reaction intermediates for electrochemical CO_2 reduction to ethylene, J. Am. Chem. Soc. 142 (2020) 2857-2867.

[20] S. Lee, G. Park, J. Lee, Importance of Ag–Cu biphasic boundaries for selective electrochemical reduction of CO_2 to ethanol, ACS Catal. 7 (2017) 8594-8604.

[21] J. Qiao, Y. Liu, F. Hong, et al., A review of catalysts for the electroreduction of carbon dioxide to produce low-carbon fuels, Chem. Soc. Rev. 43 (2014) 631-675.

[22] K.P. Kuhl, E.R. Cave, D.N. Abram, et al., New insights into the electrochemical reduction of carbon dioxide on metallic copper surfaces, Energy Environ. Sci. 5 (2012) 7050-7059.

[23] F.-Y. Gao, R.-C. Bao, M.-R. Gao, et al., Electrochemical CO_2-to-CO conversion: electrocatalysts, electrolytes, and electrolyzers, J. Mater. Chem. A 8 (2020) 15458-15478.

[24] A.Y. Khodakov, W. Chu, P. Fongarland, Advances in the development of novel cobalt Fischer− Tropsch catalysts for synthesis of long-chain hydrocarbons and clean fuels, Chem. Rev. 107 (2007) 1692-1744.

[25] R. Kortlever, J. Shen, K.J.P. Schouten, et al., Catalysts and reaction pathways for the electrochemical reduction of carbon dioxide, J. Phys. Chem. Lett. 6 (2015) 4073-4082.

[26] J. Rosen, G.S. Hutchings, Q. Lu, et al., Mechanistic insights into the electrochemical reduction of CO_2 to CO on nanostructured Ag surfaces, ACS Catal. 5 (2015) 4293-4299.

[27] S. Back, M.S. Yeom, Y. Jung, Active sites of Au and Ag nanoparticle catalysts for CO_2 electroreduction to CO, ACS Catal. 5 (2015) 5089-5096.

[28] Y. Hori, H. Wakebe, T. Tsukamoto, et al., Electrocatalytic process of CO selectivity in electrochemical reduction of CO_2 at metal electrodes in aqueous media, Electrochim. Acta 39 (1994) 1833-1839.

[29] Y. Chen, C.W. Li, M.W. Kanan, Aqueous CO_2 reduction at very low overpotential on oxide-derived Au nanoparticles, J. Am. Chem. Soc. 134 (2012) 19969-19972.

[30] C. Kim, H.S. Jeon, T. Eom, et al., Achieving selective and efficient electrocatalytic activity for CO_2 reduction using immobilized silver nanoparticles, J. Am. Chem. Soc. 137 (2015) 13844-13850.

[31] W. Luo, J. Zhang, M. Li, et al., Boosting CO production in electrocatalytic CO_2 reduction on highly porous Zn catalysts, ACS Catal. 9 (2019) 3783-3791.

[32] A. Wuttig, Y. Yoon, J. Ryu, et al., Bicarbonate is not a general acid in Au-catalyzed CO_2 electroreduction, J. Am. Chem. Soc. 139 (2017) 17109-17113.

[33] M. Ma, B.J. Trześniewski, J. Xie, et al., Selective and efficient reduction of carbon dioxide to carbon monoxide on oxide-derived nanostructured silver electrocatalysts, Angew. Chem. 128 (2016) 9900-9904.

[34] R. Chaplin, A. Wragg, Effects of process conditions and electrode material on reaction pathways for carbon dioxide electroreduction with particular reference to formate formation, J. Appl. Electrochem. 33 (2003) 1107-1123.

[35] J. Qiao, Y. Liu, J. Zhang, Electrochemical reduction of carbon dioxide: fundamentals and technologies, CRC Press, 2016.

[36] Q. Lu, J. Rosen, Y. Zhou, et al., A selective and efficient electrocatalyst for carbon dioxide reduction, Nat. Commun. 5 (2014) 3242.

[37] C. Delacourt, P.L. Ridgway, J.B. Kerr, et al., Design of an electrochemical cell making syngas (CO+ H_2) from CO_2 and H_2O reduction at room temperature, J. Electrochem. Soc. 155 (2008) B42-B49.

[38] S. Liu, H. Tao, L. Zeng, et al., Shape-dependent electrocatalytic reduction of CO_2 to CO on triangular silver nanoplates, J. Am. Chem. Soc. 139 (2017) 2160-2163.

[39] C. Shi, H.A. Hansen, A.C. Lausche, et al., Trends in electrochemical CO_2 reduction activity for open and close-packed metal surfaces, Phys. Chem. Chem. Phys. 16 (2014) 4720-4727.

[40] Y. Li, Q. Sun, Recent advances in breaking scaling relations for effective electrochemical conversion of CO_2, Adv. Energy Mater. 6 (2016) 1600463.

[41] W. Zhu, Y.-J. Zhang, H. Zhang, et al., Active and selective conversion of CO_2 to CO on ultrathin Au nanowires, J. Am. Chem. Soc. 136 (2014) 16132-16135.

[42] C. Chen, B. Zhang, J. Zhong, et al., Selective electrochemical CO_2 reduction over highly porous gold films, J. Mater. Chem. A 5 (2017) 21955-21964.

[43] S. Liu, X.-Z. Wang, H. Tao, et al., Ultrathin 5-fold twinned sub-25 nm silver nanowires enable highly selective electroreduction of CO_2 to CO, Nano Energy 45 (2018) 456-462.

[44] D. Gao, H. Zhou, J. Wang, et al., Size-dependent electrocatalytic reduction of CO_2 over Pd nanoparticles, J. Am. Chem. Soc. 137 (2015) 4288-4291.

[45] D. Gao, H. Zhou, F. Cai, et al., Pd-containing nanostructures for electrochemical CO_2 reduction reaction, ACS Catal. 8 (2018) 1510-1519.

[46] A. Salehi-Khojin, H.-R.M. Jhong, B.A. Rosen, et al., Nanoparticle silver catalysts that show enhanced activity for carbon dioxide electrolysis, J. Phys. Chem. C 117 (2013) 1627-1632.

[47] N. Hoshi, M. Kato, Y. Hori, Electrochemical reduction of CO_2 on single crystal electrodes of silver Ag (111), Ag (100) and Ag (110), J. Electroanal. Chem. 440 (1997) 283-286.

[48] A. Klinkova, P. De Luna, C.-T. Dinh, et al., Rational design of efficient palladium catalysts for electroreduction of carbon dioxide to formate, ACS Catal. 6 (2016) 8115-8120.

[49] N. Hoshi, M. Noma, T. Suzuki, et al., Structural effect on the rate of CO_2 reduction on single crystal electrodes of palladium, J. Electroanal. Chem. 421 (1997) 15-18.

[50] H.-E. Lee, K.D. Yang, S.M. Yoon, et al., Concave rhombic dodecahedral Au nanocatalyst with multiple high-index facets for CO_2 reduction, ACS Nano 9 (2015) 8384-8393.

[51] Q. Zhang, H. Wang, Facet-dependent catalytic activities of Au nanoparticles enclosed by high-index facets, ACS Catal. 4 (2014) 4027-4033.

[52] K.D. Yang, C.W. Lee, J.H. Jang, et al., Rise of nano effects in electrode during electrocatalytic CO_2 conversion, Nanotechnology 28 (2017) 352001.

[53] R.G. Mariano, K. McKelvey, H.S. White, et al., Selective increase in CO_2 electroreduction activity at grain-boundary surface terminations, Science 358 (2017) 1187-1192.

[54] K.-S. Kim, W.J. Kim, H.-K. Lim, et al., Tuned chemical bonding ability of Au at grain boundaries for enhanced electrochemical CO_2 reduction, ACS Catal. 6 (2016) 4443-4448.

[55] C. Rogers, W.S. Perkins, G. Veber, et al., Synergistic enhancement of electrocatalytic CO_2 reduction with gold nanoparticles embedded in functional graphene nanoribbon composite electrodes, J. Am. Chem. Soc. 139 (2017) 4052-4061.

[56] L. Zhang, F. Mao, L.R. Zheng, et al., Tuning metal catalyst with metal–C_3N_4 interaction for efficient CO_2 electroreduction, ACS Catal. 8 (2018) 11035-11041.

[57] V.R. Stamenkovic, B. Fowler, B.S. Mun, et al., Improved oxygen reduction activity on Pt_3Ni (111) via increased surface site availability, Science 315 (2007) 493-497.

[58] J.-H. Kim, H. Woo, J. Choi, et al., CO_2 electroreduction on Au/TiC: enhanced activity due to metal–support interaction, ACS Catal. 7 (2017) 2101-2106.

[59] J.-H. Kim, H. Woo, S.-W. Yun, et al., Highly active and selective Au thin layer on Cu polycrystalline surface prepared by galvanic displacement for the electrochemical reduction of CO_2 to CO, Appl. Catal. B 213 (2017) 211-215.

[60] D. Gao, Y. Zhang, Z. Zhou, et al., Enhancing CO_2 electroreduction with the metal-oxide interface, J. Am. Chem. Soc. 139 (2017) 5652-5655.

[61] X. Yuan, Y. Wu, B. Jiang, et al., Interface engineering of silver-based heterostructures for CO_2 reduction reaction, ACS Appl. Mater. Interfaces 12 (2020) 56642-56649.

[62] X. Feng, K. Jiang, S. Fan, et al., A direct grain-boundary-activity correlation for CO electroreduction on Cu nanoparticles, ACS Cent. Sci. 2 (2016) 169-174.

[63] M. Li, J. Wang, P. Li, et al., Mesoporous palladium–copper bimetallic electrodes for selective electrocatalytic reduction of aqueous CO_2 to CO, J. Mater. Chem. A 4 (2016) 4776-4782.

[64] Z. Yin, D. Gao, S. Yao, et al., Highly selective palladium-copper bimetallic electrocatalysts for the electrochemical reduction of CO_2 to CO, Nano Energy 27 (2016) 35-43.

[65] D. Kim, J. Resasco, Y. Yu, et al., Synergistic geometric and electronic effects for electrochemical reduction of carbon dioxide using gold–copper bimetallic nanoparticles, Nat. Commun. 5 (2014) 4948.

[66] J. Choi, M.J. Kim, S.H. Ahn, et al., Electrochemical CO_2 reduction to CO on dendritic Ag–Cu electrocatalysts prepared by electrodeposition, Chem. Eng. J. 299 (2016) 37-44.

[67] C. Roy, J. Galipaud, L. Fréchette-Viens, et al., CO_2 electroreduction at Au_xCu_{1-x} obtained by pulsed laser deposition in O_2 atmosphere, Electrochim. Acta 246 (2017) 115-122.

[68] S. Rasul, D.H. Anjum, A. Jedidi, et al., A highly selective copper–indium bimetallic electrocatalyst for the electrochemical reduction of aqueous CO_2 to CO, Angew. Chem. Int. Ed. 54 (2015) 2146-2150.

[69] S. Sarfraz, A.T. Garcia-Esparza, A. Jedidi, et al., Cu–Sn bimetallic catalyst for selective aqueous electroreduction of CO_2 to CO, ACS Catal. 6 (2016) 2842-2851.

[70] Q. Li, J. Fu, W. Zhu, et al., Tuning Sn-catalysis for electrochemical reduction of CO_2 to CO via the core/shell Cu/SnO_2 structure, J. Am. Chem. Soc. 139 (2017) 4290-4293.

[71] Y. Zhao, C. Wang, G.G. Wallace, Tin nanoparticles decorated copper oxide nanowires for selective electrochemical reduction of aqueous CO_2 to CO, J. Mater. Chem. A 4 (2016) 10710-10718.

[72] A. Jedidi, S. Rasul, D. Masih, et al., Generation of Cu–In alloy surfaces from $CuInO_2$ as selective catalytic sites for CO_2 electroreduction, J. Mater. Chem. A 3 (2015) 19085-19092.

[73] G.O. Larrazábal, T. Shinagawa, A.J. Martín, et al., Microfabricated electrodes unravel the role of interfaces in multicomponent copper-based CO_2 reduction catalysts, Nat. Commun. 9(1) (2018) 1477.

[74] W. Luo, W. Xie, R. Mutschler, et al., Selective and stable electroreduction of CO_2 to CO at the copper/indium interface, ACS Catal. 8 (2018) 6571-6581.

[75] Y. Hori, K. Kikuchi, S. Suzuki, Production of CO and CH_4 in electrochemical reduction of CO_2 at metal electrodes in aqueous hydrogencarbonate solution, Chem. Lett. 14 (1985) 1695-1698.

[76] W.D. Hye, S. Hyeyoung, K. Jaekang, et al., Highly efficient, selective, and stable CO_2 electroreduction on a hexagonal Zn catalyst, Angew. Chem. Int. Ed. 55 (2016) 9297-9300.

[77] B. Qin, Y. Li, H. Fu, et al., Electrochemical reduction of CO_2 into tunable syngas production by regulating the crystal facets of earth-abundant Zn catalyst, ACS Appl. Mater. Interfaces 10 (2018) 20530-20539.

[78] P. Moreno-García, N. Schlegel, A. Zanetti, et al., Selective electrochemical reduction of CO_2 to CO on Zn-based foams produced by Cu^{2+} and template-assisted electrodeposition, ACS Appl. Mater. Interfaces 10 (2018) 31355-31365.

[79] D.L.T. Nguyen, M.S. Jee, D.H. Won, et al., Selective CO_2 reduction on zinc electrocatalyst: the effect of zinc oxidation state induced by pretreatment environment, ACS Sustain. Chem. Eng. 5 (2017) 11377-11386.

[80] T. Zhang, X. Li, Y. Qiu, et al., Multilayered Zn nanosheets as an electrocatalyst for efficient electrochemical reduction of CO_2, J. Catal. 357 (2018) 154-162.

[81] M. Morimoto, Y. Takatsuji, K. Hirata, et al., Visualization of catalytic edge reactivity in electrochemical CO_2 reduction on porous Zn electrode, Electrochim. Acta 290 (2018) 255-261.

[82] K. Liu, J. Wang, M. Shi, et al., Simultaneous achieving of high Faradaic efficiency and CO partial current density for CO_2 reduction via robust, noble-metal-free Zn nanosheets with favorable adsorption energy, Adv. Energy Mater. 9 (2019) 1900276.

[83] J. Greeley, T.F. Jaramillo, J. Bonde, et al., Computational high-throughput screening of electrocatalytic materials for hydrogen evolution, Nat. Mater. 5 (2006) 909-913.

[84] R. He, A. Zhang, Y. Ding, et al., Achieving the widest range of syngas proportions at high current density over cadmium sulfoselenide nanorods in CO_2 electroreduction, Adv. Mater. 30 (2018) 1705872.

[85] B. Qin, Y. Li, H. Wang, et al., Efficient electrochemical reduction of CO_2 into CO promoted by sulfur vacancies, Nano Energy 60 (2019) 43-51.

[86] Y.H. Li, L. Cheng, P.F. Liu, et al., Simple cadmium sulfide compound with stable 95 % selectivity for carbon dioxide electroreduction in aqueous medium, ChemSusChem 11 (2018) 1421-1425.

[87] L. Cheng, Y. Li, A. Chen, et al., Impacts on carbon dioxide electroreduction of cadmium sulfides via continuous surface sulfur vacancy engineering, Chem. Commun. 56 (2020) 563-566.

[88] S.-H. Yu, F.-Y. Gao, S.-J. Hu, et al., High-curvature transition metal chalcogenide nanostructures with profound proximity effect enable fast and selective CO_2 electroreduction, Angew. Chem. 132 (2020) 8784-8790.

[89] N. Meng, C. Liu, Y. Liu, et al., Efficient electrosynthesis of syngas with tunable CO/H_2 ratios over $Zn_xCd_{1-x}S$-amine inorganic-organic hybrids, Angew. Chem. Int. Ed. 58 (2019) 18908-18912.

[90] X. Jiang, X. Wang, Q. Wang, et al., Efficient activation and electroreduction of carbon dioxide on an electrocatalyst cadmium carbonate, ACS Applied Energy Materials 4 (2021) 2073-2080.

[91] M. Asadi, B. Kumar, A. Behranginia, et al., Robust carbon dioxide reduction on molybdenum disulphide edges, Nat. Commun. 5 (2014) 4470.

[92] B.A. Rosen, A. Salehi-Khojin, M.R. Thorson, et al., Ionic liquid–mediated selective conversion of CO_2 to CO at low overpotentials, Science 334 (2011) 643-644.

[93] M. Asadi, K. Kim, C. Liu, et al., Nanostructured transition metal dichalcogenide electrocatalysts for CO_2 reduction in ionic liquid, Science 353 (2016) 467-470.

[94] B.A. Rosen, J.L. Haan, P. Mukherjee, et al., In situ spectroscopic examination of a low overpotential pathway for carbon dioxide conversion to carbon monoxide, J. Phys. Chem. C 116 (2012) 15307-15312.

[95] J.L. DiMeglio, J. Rosenthal, Selective conversion of CO_2 to CO with high efficiency using an inexpensive bismuth-based electrocatalyst, J. Am. Chem. Soc. 135 (2013) 8798-8801.

[96] Z. Zhang, M. Chi, G.M. Veith, et al., Rational design of Bi nanoparticles for efficient electrochemical CO_2 reduction: the elucidation of size and surface condition effects, ACS Catal. 6 (2016) 6255-6264.

[97] C. Ding, A. Li, S.-M. Lu, et al., In situ electrodeposited indium nanocrystals for efficient CO_2 reduction to CO with low overpotential, ACS Catal. 6 (2016) 6438-6443.

[98] L. Sun, G.K. Ramesha, P.V. Kamat, et al., Switching the reaction course of electrochemical CO_2 reduction with ionic liquids, Langmuir 30 (2014) 6302-6308.

[99] J. Xu, X. Li, W. Liu, et al., Carbon dioxide electroreduction into syngas boosted by a partially delocalized charge in molybdenum sulfide selenide alloy monolayers, Angew. Chem. Int. Ed. 56 (2017) 9121-9125.

[100] T. Liu, S. Ali, Z. Lian, et al., CO_2 electoreduction reaction on heteroatom-doped carbon cathode materials, J. Mater. Chem. A 5 (2017) 21596-21603.

[101] D. Voiry, H.S. Shin, K.P. Loh, et al., Low-dimensional catalysts for hydrogen evolution and CO_2 reduction, Nat. Rev. Chem. 2(1) (2018) 0105.

[102] T. Zheng, K. Jiang, H. Wang, Recent Advances in electrochemical CO_2-to-CO conversion on heterogeneous catalysts, Adv. Mater. 30 (2018) 1802066.

[103] J. Wu, R.M. Yadav, M. Liu, et al., Achieving highly efficient, selective, and stable CO_2 reduction on nitrogen-doped carbon nanotubes, ACS nano 9 (2015) 5364-5371.

[104] P.P. Sharma, J. Wu, R.M. Yadav, et al., Nitrogen-doped carbon nanotube arrays for high-efficiency electrochemical reduction of CO_2: on the understanding of defects, defect density, and selectivity, Angew. Chem. 127 (2015) 13905-13909.

[105] J. Wu, M. Liu, P.P. Sharma, et al., Incorporation of nitrogen defects for efficient reduction of CO_2 via two-electron pathway on three-dimensional graphene foam, Nano Lett. 16 (2016) 466-470.

[106] J. Xu, Y. Kan, R. Huang, et al., Revealing the origin of activity in nitrogen-doped nanocarbons towards electrocatalytic reduction of carbon dioxide, ChemSusChem 9 (2016) 1085-1089.

[107] S. Liu, H. Yang, X. Huang, et al., Identifying active sites of nitrogen-doped carbon materials for the CO_2 reduction reaction, Adv. Funct. Mater. 28 (2018) 1800499.

[108] F. Pan, B. Li, X. Xiang, et al., Efficient CO_2 electroreduction by highly dense and active pyridinic nitrogen on holey carbon layers with fluorine engineering, ACS Catal. 9 (2019) 2124-2133.

[108] M. Gangeri, S. Perathoner, S. Caudo, et al., Fe and Pt carbon nanotubes for the electrocatalytic conversion of carbon dioxide to oxygenates, Catal. Today 143 (2009) 57-63.

[109] J. Rogelj, D. Huppmann, V. Krey, et al., A new scenario logic for the Paris Agreement long-term temperature goal, Nature 573 (2019) 357-363.

[110] J.M. Spurgeon, B. Kumar, A comparative technoeconomic analysis of pathways for commercial electrochemical CO_2 reduction to liquid products, Energy Environ. Sci. 11 (2018) 1536-1551.

[111] Z.-L. Wang, C. Li, Y. Yamauchi, Nanostructured nonprecious metal catalysts for electrochemical reduction of carbon dioxide, Nano Today 11 (2016) 373-391.

[112] J. Rosen, G.S. Hutchings, Q. Lu, et al., Electrodeposited Zn dendrites with enhanced CO selectivity for electrocatalytic CO_2 reduction, ACS Catal. 5 (2015) 4586-4591.

[113] F. Quan, D. Zhong, H. Song, et al., A highly efficient zinc catalyst for selective electroreduction of carbon dioxide in aqueous NaCl solution, J. Mater. Chem. A 3 (2015) 16409-16413.

[114] Z. Wang, G. Yang, Z. Zhang, et al., Selectivity on etching: creation of high-energy facets on copper nanocrystals for CO_2 electrochemical reduction, ACS Nano 10 (2016) 4559-4564.

[115] H.S. Jeon, I. Sinev, F. Scholten, et al., Operando evolution of the structure and oxidation state of size-controlled Zn nanoparticles during CO_2 electroreduction, J. Am. Chem. Soc. 140 (2018) 9383-9386.

[116] S. Ikeda, A. Hattori, K. Ito, et al., Zinc ion effect on the electrochemical reduction of carbon dioxide at zinc electrode in aqueous solutions, Electrochem. 67 (1999) 27-33.

[117] Y. Hori, Modern aspects of electrochemistry 42, Springer New York, 2008, pp. 89-189.

[118] G. Zhigang, K. Xiangdong, C. Weiwei, et al., Oxygen vacancies in ZnO nanosheets enhance CO_2 electrochemical reduction to CO, Angew. Chem. Int. Ed. 57 (2018) 6054-6059.

[119] H.-K. Lim, H. Shin, W.A. Goddard, et al., Embedding covalency into metal catalysts for efficient electrochemical conversion of CO_2, J. Am. Chem. Soc. 136 (2014) 11355-11361.

[120] W.J. Durand, A.A. Peterson, F. Studt, et al., Structure effects on the energetics of the electrochemical reduction of CO_2 by copper surfaces, Surf. Sci. 605 (2011) 1354-1359.

[121] J.K. Nørskov, F. Abild-Pedersen, F. Studt, et al., Density functional theory in surface chemistry and catalysis, Proc. Natl. Acad. Sci. 108 (2011) 937-943.

[122] D.U. Nielsen, X.-M. Hu, K. Daasbjerg, et al., Chemically and electrochemically catalysed conversion of CO_2 to CO with follow-up utilization to value-added chemicals, Nat. Catal. 1 (2018) 244-254.

[123] A. Modak, P. Bhanja, S. Dutta, et al., Catalytic reduction of CO_2 into fuels and fine chemicals. Green Chem. 22 (2020) 4002-4033.

[124] J.B. Branco, P.E. Brito, A.C. Ferreira, Methanation of CO_2 over nickel-lanthanide bimetallic oxides supported on silica. Chem. Eng. J. 380 (2020) 122465.

[125] A. Modak, A. Ghosh, A. Bhaumik, et al., CO_2 hydrogenation over functional nanoporous polymers and metal-organic frameworks. Adv. Colloid Interface Sci. 290 (2021) 102349.

[126] D.D. Zhu, J.L. Liu, S.Z. Qiao, Recent advances in inorganic heterogeneous electrocatalysts for reduction of carbon dioxide, Adv. Mater. 28 (2016) 3423-3452.

[127] R. Reske, H. Mistry, F. Behafarid, et al., Particle size effects in the catalytic electroreduction of CO_2 on Cu nanoparticles, J. Am. Chem. Soc. 136 (2014) 6978-6986.

[128] S. Mou, Y. Li, L. Yue, et al., Cu_2Sb decorated Cu nanowire arrays for selective electrocatalytic CO_2 to CO conversion. Nano Res. 14 (2021) 2831-2836.

[129] S. Zhang, P. Kang, T.J. Meyer, Nanostructured tin catalysts for selective electrochemical reduction of carbon dioxide to formate, J. Am. Chem. Soc. 136 (2014) 1734-1737.

[130] F. Lei, W. Liu, Y. Sun, et al., Metallic tin quantum sheets confined in graphene toward high-efficiency carbon dioxide electroreduction, Nat. Commun. 7 (2016) 12697.

[131] C. Li, G. Shen, R. Zhang, et al., Zn nanosheets coated with a ZnS subnanometer layer for effective and durable CO_2 reduction, J. Mater. Chem. A 7 (2019) 1418-1423.

[132] J. Xiao, M.-R. Gao, S. Liu, et al., Hexagonal Zn nanoplates enclosed by Zn (100) and Zn (002) facets for highly selective CO_2 electroreduction to CO, ACS Appl. Mater. Interfaces12 (2020) 31431-31438.

[133] H. Jung, S.Y. Lee, C.W. Lee, et al., Electrochemical fragmentation of Cu_2O nanoparticles enhancing selective C–C coupling from CO_2 reduction reaction, J. Am. Chem. Soc. 141 (2019) 4624-4633.

[134] X. Sun, L. Lu, Q. Zhu, et al., MoP nanoparticles supported on indium-doped porous carbon: outstanding catalysts for highly efficient CO_2 electroreduction, Angew. Chem. Int. Ed. 57 (2018) 2427-2431.

[135] A. Dutta, A. Kuzume, V. Kaliginedi, et al., Probing the chemical state of tin oxide NP catalysts during CO_2 electroreduction: A complementary operando approach, Nano Energy 53 (2018) 828-840.

[136] D. Raciti, K.J. Livi, C. Wang, Highly dense Cu nanowires for low-overpotential CO_2 reduction, Nano Lett.. 15 (2015) 6829-6835.

[137] Y. Liang, W. Zhou, Y. Shi, et al., Unveiling in situ evolved In/In_2O_{3-x} heterostructure as the active phase of In_2O_3 toward efficient electroreduction of CO_2 to formate, Sci. Bull. 65 (2020) 1547-1554.

[138] Y. Shi, Y. Ji, J. Long, et al., Unveiling hydrocerussite as an electrochemically stable active phase for efficient carbon dioxide electroreduction to formate, Nat. commun. 11 (2020) 3415.

[139] Y. Wang, W. Ding, S. Chen, et al., Cobalt carbonate hydroxide/C: an efficient dual electrocatalyst for oxygen reduction/evolution reactions. Chem. Commun. 50 (2014) 15529-15532.

[140] D. Vidyasagar, S.G. Ghugal, A. Kulkarni, et al., Microwave assisted in situ decoration of a g-C_3N_4 surface with $CdCO_3$ nanoparticles for visible light driven photocatalysis, New J. Chem. 42 (2018) 6322-6331.

[141] C. Xin, M. Hu, K. Wang, et al., Significant enhancement of photocatalytic reduction of CO_2 with H_2O over ZnO by the formation of basic zinc carbonate, Langmuir 33 (2017) 6667-6676.

[142] T. Tang, W.-J. Jiang, S. Niu, et al., Electronic and morphological dual modulation of cobalt carbonate hydroxides by Mn doping toward highly efficient and stable bifunctional electrocatalysts for overall water splitting, J. Am. Chem. Soc. 139 (2017) 8320-8328.

[143] L.-P. Yuan, W.-J. Jiang, X.-L. Liu, et al., Molecularly engineered strong metal oxide–support interaction enables highly efficient and stable CO_2 electroreduction, ACS Catal. 10 (2020) 13227-13235.

[144] H. Li, C. Chen, D. Yan, et al., Interfacial effects in supported catalysts for electrocatalysis, J. Mater. Chem. A 7 (2019) 23432-23450.

[145] X. He, Z. Han, F. Kong, et al., Facile synthesis of $CdCO_3$ cubic particles/graphene composite with enhanced electrochemical performance for lithium-ion batteries, Mater. Lett. 236 (2019) 672-675.

[146] G. Kresse, J. Furthmüller, Efficiency of ab-initio total energy calculations for metals and semiconductors using a plane-wave basis set, Comput. Mater. Sci. 6 (1996) 15-50.

[147] G. Kresse, J. Hafner, Ab initio molecular-dynamics simulation of the liquid-metal–amorphous-semiconductor transition in germanium. Phys. Rev. B 49 (1994) 14251.

[148] H.A. Hansen, J.B. Varley, A.A. Peterson, et al., Understanding trends in the electrocatalytic activity of metals and enzymes for CO_2 reduction to CO, J. Phys. Chem. Lett. 4 (2013) 388-392.

[149] H. Gamsjäger, W. Preis, E. Königsberger, et al., Solid-solute phase equilibria in aqueous solution. XI. Aqueous solubility and standard Gibbs energy of cadmium carbonate. J. solution chem. 28 (1999) 711-720.

[150] D.R. Lide, CRC handbook of chemistry and physics, CRC press, 2004.

[151] S. Verma, X. Lu, S. Ma, et al., The effect of electrolyte composition on the electroreduction of CO_2 to CO on Ag based gas diffusion electrodes. Phys. Chem. Chem. Phys. 18 (2016) 7075-7084.

[152] T.N. Huan, N. Ranjbar, G. Rousse, et al., Electrochemical reduction of CO_2 catalyzed by Fe-N-C materials: A structure–selectivity study, ACS Catal. 7 (2017) 1520-1525.

[153] A.R. Bredar, A.L. Chown, A.R. Burton, et al., Electrochemical impedance spectroscopy of metal oxide electrodes for energy applications. ACS Appl. Energy Mater., 3 (2020) 66-98.

[154] F. Zhang, X. Wang, D. Yin, et al., Efficiency and mechanisms of Cd removal from aqueous solution by biochar derived from water hyacinth (Eichornia crassipes), J. Environ. Manage., 153 (2015) 68-73.

[155] J. Wang, J. Kim, S. Choi, et al., A review of carbon-supported nonprecious metals as energy-related electrocatalysts, Small Methods, 4 (2020) 2000621.

[156] Y. Wu, S. Cao, J. Hou, et al., Rational design of nanocatalysts with nonmetal species modification for electrochemical CO_2 reduction, Adv. Energy Mater. 10 (2020) 2000588.

[157] Z.-P. Liu, P. Hu, A new insight into Fischer−Tropsch synthesis, J. Am. Chem. Soc. 124 (2002) 11568-11569.

[158] W. Zheng, J. Yang, H. Chen, et al., Atomically defined undercoordinated active sites for highly efficient CO_2 electroreduction, Adv. Funct. Mater. 30 (2020) 1907658.

[159] P. Prabhu, V. Jose, J.M. Lee, Heterostructured catalysts for electrocatalytic and photocatalytic carbon dioxide reduction, Adv. Funct. Mater. 30 (2020) 1910768.

[160] M. Li, S. Garg, X. Chang, et al., Toward excellence of transition metal‐based catalysts for CO_2 electrochemical reduction: an overview of strategies and rationales., Small Methods 4 (2020) 2000033.

[161] X. Duan, J. Xu, Z. Wei, et al., Metal‐free carbon materials for CO_2 electrochemical reduction, Adv. Mater. 29 (2017) 1701784.

[162] S. Ren, D. Joulié, D. Salvatore, et al., Molecular electrocatalysts can mediate fast, selective CO_2 reduction in a flow cell, Science 365 (2019) 367-369.

[163] S. Lin, C.S. Diercks, Y.-B. Zhang, et al., Covalent organic frameworks comprising cobalt porphyrins for catalytic CO_2 reduction in water, Science 349 (2015) 1208-1213.

[164] S. Liu, J. Xiao, X.F. Lu, et al., Efficient electrochemical reduction of CO_2 to HCOOH over Sub-2 nm SnO_2 quantum wires with exposed grain boundaries, Angew. Chem. Int. Ed. 58 (2019) 8499-8503.

[165] Z. Sun, T. Ma, H. Tao, et al., Fundamentals and challenges of electrochemical CO_2 reduction using two-dimensional materials, Chem 3 (2017) 560-587.

[166] A.S. Varela, M. Kroschel, T. Reier, et al., Controlling the selectivity of CO_2 electroreduction on copper: The effect of the electrolyte concentration and the importance of the local pH, Catal. Today 260 (2016) 8-13.

[167] S. Ringe, E.L. Clark, J. Resasco, et al., Understanding cation effects in electrochemical CO_2 reduction, Energy Environ. Sci. 12 (2019) 3001-3014.

[168] Y. Hori, A. Murata, R. Takahashi, Formation of hydrocarbons in the electrochemical reduction of carbon dioxide at a copper electrode in aqueous solution, J. Chem. Soc., Faraday Trans. 1 85 (1989) 2309-2326.

[169] M. Ma, K. Djanashvili, W.A. Smith, Controllable hydrocarbon formation from the electrochemical reduction of CO_2 over Cu nanowire arrays, Angew. Chem. Int. Ed. 55 (2016) 6680-6684.

[170] A. Goyal, G. Marcandalli, V.A. Mints, et al., Competition between CO_2 reduction and hydrogen evolution on a gold electrode under well-defined mass transport conditions, J. Am. Chem. Soc. 142 (2020) 4154-4161.

[171] W. Li, M. Li, S. Xie, et al., Improving the photoelectrochemical and photocatalytic performance of CdO nanorods with CdS decoration, CrystEngComm 15 (2013) 4212-4216.

[172] W.J. Dufresne, C.J. Rufledt, C.P. Marshall, Raman spectroscopy of the eight natural carbonate minerals of calcite structure, J. Raman Spectrosc., 49 (2018) 1999-2007.

[173] H. Li, H.L. Xin, D.A. Muller, et al., Visualizing the 3D internal structure of calcite single crystals grown in agarose hydrogels, Science 326 (2009) 1244-1247.

[174] S. Weiner, L. Addadi, Design strategies in mineralized biological materials, J. Mater. Chem. 7 (1997) 689-702.

[175] S. Liu, H. Tao, Q. Liu, et al., Rational design of silver sulfide nanowires for efficient CO_2 electroreduction in ionic liquid, ACS Catal. 8 (2018) 1469-1475.

[176] W. Ju, A. Bagger, G.-P. Hao, et al., Understanding activity and selectivity of metal-nitrogen-doped carbon catalysts for electrochemical reduction of CO_2, Nat. Commun. 8 (2017) 944.

[177] E.L. Clark, J. Resasco, A. Landers, et al., Standards and protocols for data acquisition and reporting for studies of the electrochemical reduction of carbon dioxide, ACS Catal. 8 (2018) 6560-6570.

[178] F. Li, L. Chen, G.P. Knowles, et al., Hierarchical mesoporous SnO_2 nanosheets on carbon cloth: a robust and flexible electrocatalyst for CO_2 reduction with high efficiency and selectivity, Angew. Chem. 129 (2017) 520-524.

[179] D. Strmcnik, P.P. Lopes, B. Genorio, et al., Design principles for hydrogen evolution reaction catalyst materials, Nano Energy 29 (2016) 29-36.

[180] N. Gupta, M. Gattrell, B. MacDougall, Calculation for the cathode surface concentrations in the electrochemical reduction of CO_2 in $KHCO_3$ solutions, J. Appl. Electrochem. 36 (2006) 161-172.